MASS TRANSFER AND DEVOLATILIZATION PHENOMENA IN VERY LARGE COAL DOMAINS AT VERY SLOW HEATING RATES

by

Keith William Gneshin

A dissertation submitted to the faculty of
The University of Utah
in partial fulfillment of the requirements for the degree of

Doctor of Philosophy

Department of Chemical Engineering

The University of Utah

December 2013

The University of Utah Graduate School

STATEMENT OF DISSERTATION APPROVAL

The dissertation of **Keith William Gneshin**

has been approved by the following supervisory committee members:

Eric Eddings	, Chair	**5/30/13** Date Approved
Milind Deo	, Member	**5/30/13** Date Approved
John McLennan	, Member	**6/11/13** Date Approved
Philip Smith	, Member	**5/30/13** Date Approved
Hong-Yong Sohn	, Member	**5/30/13** Date Approved

and by **Milind Deo** , Chair/Dean of

the Department/College/School of **Chemical Engineering**

and by David B. Kieda, Dean of The Graduate School.

ABSTRACT

The proliferation of nonconventional subsurface hydrocarbon production methods has turned some attention toward production from deep coal seams. There exists little research into coal pyrolysis under conditions relevant to subsurface processing (large coal domains, very slow heating rates, high hydrostatic pressure, volumetric confinement). Basic studies into the phenomena of mass transfer and devolatilization in a high-volatile Utah bituminous coal are described for very large particles (>1 cm) at very slow heating rates (< 10K/min) at atmospheric pressure. Studied systems included large coal blocks heated via immersion heaters and 2 cm-diameter coal cores heated in a tube furnace apparatus. Changes in char porosity during pyrolysis as a function of heating rate are described in large coal blocks. Coal core data show char porosity evolution as a function of temperature and heating rate and demonstrate a distinct threshold for plastic deformation. Volumetric confinement of core swelling was shown to dramatically affect char morphology. Devolatilization data from coal cores are presented, showing little impact of heating rate upon total volatile yield, but a substantial impact upon the yield of tars. A Knudsen flow analysis is also presented to argue that the driving force for mass transfer at very slow heating rates is pressure-driven flow. Several novel pyrolysis phenomena are described, including a pore plugging effect at very slow heating rates. The presented experimental work suggests that many common assumptions for conventional coal pyrolysis would not apply in a subsurface processing environment.

To Ms. Busse – you taught me that mathematics and engineering were a worthwhile pursuit. Another 11 years of schooling taught me that that's a half-truth.

TABLE OF CONTENTS

LIST OF TABLES

NOMENCLATURE

A – area, m^2

B – preexponential factor, K

C – Sutherland constant, K

C_p – heat capacity, J kg^{-1} K^{-1}

D – heater length, m

F – slip flow friction factor, dimensionless

g – gravitational constant, 9.81 m s^{-2}

h – heat transfer coefficient, W m^{-2} K^{-1}

J – mass flux rate, kg m^{-2} s^{-1}

k – thermal conductivity, W m^{-1} K^{-1}

L – block length, m

M – molecular weight, kg $kmol^{-1}$

P – pressure, Pa

Pr – Prandtl number

q – heat flux, W m^{-2}

r – radial distance, m

R – maximum radial distance, m

R_g – Universal gas constant, 8.314 J mol^{-1} K^{-1}

t – time, s

T – temperature, K

x – distance, m

α – thermal diffusivity, $m^2\ s^{-1}$

β – expansion coefficient, K^{-1}

γ – exponential factor, unitless

Δt – time step, s

Δx – node length, m

ε – emissivity

η – dynamic viscosity, $m^2\ s^{-1}$

κ – wall roughness, dimensionless

λ – exponential coefficient, m^{-2}

μ – viscosity, Pa s

ρ – density, $kg\ m^{-3}$

σ – Stefan-Boltzmann coefficient, $5.678 \times 10^{-8}\ W\ m^{-4}\ K^{-1}$

ACKNOWLEDGMENTS

First, I would like to thank the U.S. Department of Energy Office of Science for providing me with a very generous graduate fellowship. The focus of my work would probably have been far different if not for the freedom afforded me by the fellowship. I would also like to thank my advisor, Prof. Eric Eddings for his tireless academic and bureaucratic support. There is also a litany of people to whom I owe my gratitude for their assistance, including (but not inclusive) Sean Patterson, Chris Clayton and my thesis committee. However, there is no one to whom I am more deeply indebted than Rob Krumm. All the interesting stuff in this dissertation happened because you wouldn't let a criminally underwritten instruction manual break your spirit. And lastly, I should acknowledge the patience, compassion and support of my wife, Mary Jo, but it looks like I'm out of space so it will have to wait until my next dissertation. Sorry, dear!

CHAPTER I

INTRODUCTION

The purpose of this dissertation is to describe an investigation into the dynamics of pyrolysis-driven mass transfer in extended domains of coal at very slow heating rates. The work is relevant to a proposed technology termed underground coal thermal treatment (UCTT), a conceptual method for converting deeply buried coal into gaseous or liquid hydrocarbon fuels meant for surface consumption. The description of mass transfer given in this dissertation is an important step toward predicting the potential gas and liquid yields and their rates of evolution from a UCTT operation, two necessary objectives for demonstrating the feasibility of this technology.

The specific focus of this thesis is an analysis of the driving mechanism for mass transfer during coal pyrolysis. The research ties together porosity development data and product evolution data to assess the relative magnitude of mass transfer driving forces. The work also illuminates some unique phenomena that appear to be characteristic of coal pyrolysis at very slow heating rates in large coal domains. Although the research does not examine pressure effects or confinement effects created by mechanical loading of coal, this research should provide a foundation for examining those parameters.

This research fits within a broader effort at the University of Utah to explore fundamental and applied questions about the UCTT process. This effort aims to unite experiment, numerical modeling and theoretical kinetics development into a large-scale

description of the physics of coal pyrolysis under conditions relevant to subsurface processing. The research described here will aid the modeling and theoretical development efforts by providing insight into the assumptions that can be made to simplify the governing equations for the UCTT process. Although this work by no means represents a true experimental simulation of coal pyrolysis under UCTT *in situ* conditions, it does represent an evolutionary step toward that goal and should help to steer the phenomenology that is explored under more realistic conditions.

Description of Underground Coal Thermal Treatment

Underground coal thermal treatment is an as yet untested method for producing hydrocarbon fuels from buried coal formations. As conceptualized, this technology would be ideal for deep coal seams that cannot be exploited commercially by mining. UCTT would be similar to other nonconventional hydrocarbon production techniques, including underground coal gasification, coal-bed methane production and *in situ* oil shale retorting. Likely, the technological developments that have permitted the aforementioned production methods make UCTT a technologically and economically viable concept.

The UCTT process is envisioned to be oxygen-excluded or oxygen-limited, so the primary mode of thermal decomposition in the targeted coal seam will be pyrolysis. Although this inherently requires the investment of energy to drive the endothermic pyrolysis reactions, the tradeoff is believed to come in the form of several environmental advantages that will be discussed later. Based upon *in situ* oil share retorting methods, it is expected that the subsurface heating rate for a UCTT operation would be on the order of 10K/day (~0.01K/min) and subsurface temperatures would be on the lower end of the pyrolysis zone, perhaps 300 – 450^{o}C. Prior to this dissertation, little work has been done

to understand the dynamics of pyrolysis at such low heating rates, particulary in particles larger than those typically found in pulverized coals. One of the primary fundamental challenges to developing UCTT technology is describing coal pyrolysis at very slow heating rates and low temperatures.

It is proposed that the ideal target for UCTT is a deep coal seam, perhaps exceeding a half-mile in depth. It would also be preferable to perform the heating in a seam that is sufficiently thick to minimize heat dissipation to surrounding rock layers. An ideal candidate seam may be an exhausted coal-bed methane site because such an operation will have invested in substantial piping and pumping infrastructure and will have dried the seam, eliminating a massive energy cost to the UCTT process. Due to the operating depth of the targeted coal seams, coal pyrolysis is expected to occur under elevated hydrostatic pressure and high axial and radial loading caused by overburden and surrounding rock. The effect these parameters will have on coal pyrolysis is not understood, although the presented research does briefly explore the pyrolysis under confined conditions (but not elevated hydrostatic pressure).

UCTT operation would require the insertion of heating infrastructure into the coal seam via boreholes. In one conception of UCTT, horizontal bores will be made off of the vertical wells, allowing the insertion of heaters at the base of the coal seam. This might allow natural convection to help speed the heating process by transporting heat through natural or artificial fractures. The precise nature of the heating system is undetermined at this time, but possible candidates could include recirculated combustion gases from downhole burners or dissipation of RF or microwave radiation.

In summary, a UCTT process is expected to be a low-temperature, slow heating method for producing hydrocarbon fuels from deep coal seams. The very unique conditions created by *in situ* operation lead to a mode of coal pyrolysis that has not received much fundamental analysis. This dissertation will present one of the first descriptions of mass transfer during coal pyrolysis at temperatures and heating rates for larger coal particle sizes that accurately reflects the expected working conditions for UCTT.

Comparison to UCG, CBM and *In Situ* Oil Shale Retorting

Underground coal thermal treatment is closely related to several other *in situ* nonconventional hydrocarbon production methods, including underground coal gasification (UCG), coal-bed methane production (CBM) and *in situ* oil shale retorting. Many of the technical challenges that would face a UCTT operation have already been encountered in the aforementioned production methods. Although these methods have been explored and developed for much longer than UCTT, it could be argued that none of them have fully matured. Thus, the development of UCTT may drive technical improvements for related production methods just as the development of UCTT will draw on available methods to facilitate its implementation.

Underground coal gasification is the most similar *in situ* coal utilization technology. It has been in development since the 1930s in Russia, although the most active period of U.S. research was in the late 1970s and early 1980s [Shafirovich, 2009]. Both UCTT and UCG require the generation of heat to drive forward the chemical reactions that convert coal into fuels. UCG involves the injection of an oxidizing fluid (oxygen, water, carbon dioxide) into a heated coal seam to create a controlled combustion

front. The thermal front drives pyrolysis, combustion and gasification reactions, creating a product primarily composed of syngas (hydrogen and carbon monoxide). The syngas can either be combusted directly to produce energy, or it can be added to a Fischer-Tropsch reactor to generate longer-chain hydrocarbons. The current state-of-the-art for this technology is direct gas-to-liquid conversion (GTL), such as the GTL facility operated at the Chinchilla coal field in Queensland, Australia [Linc Energy website]. This operation feeds cleaned UCG gas from extraction wells directly into a reactor to produce liquid hydrocarbons. By contrast, a UCTT operation will be oxidant-excluded so energy will need to be provided to drive forward the pyrolysis reactions. The UCTT product distribution will primarily produce oxygenated-species from the natural oxygen content of coal, so methane and other light hydrocarbons will be a more important source of valuable fuel.

In contrast to UCTT, UCG has the advantage of being self-sustaining and efficient due to the highly exothermic nature of coal combustion. The presence of an oxidant allows most of the reactive carbon to be scoured from the coal seam, leaving behind only slagged ash in an open cavity. These cavities are prone to collapse, creating surface subsidence and damaging or destroying well infrastructure. UCTT is not anticipated to have a subsidence issue because pyrolysis inherently generates a solid-phase matrix composed mainly of fixed carbon and ash. It is expected that the solid-phase will occupy enough of the seam space to limit or prevent surface subsidence, thereby reducing infrastructure repair or replacement costs.

UCTT also bears some relationship to coal-bed methane production. CBM operations produce natural gas from buried coal seams via a series of wells that pump the

evolved fuel to the surface [Pashin, 2011]. The anticipated fuel composition from UCTT is expected to more closely resemble that of the product from CBM than that from UCG. CBM and UCTT are also related by the need to dry the coal seam before hydrocarbon production can commence. CBM sites are proposed as a logical location for attempting UCTT because well infrastructure has been built, the permeability of the seam will have been increased, by hydraulic fracturing, and the water will have been removed, likely eliminating the single largest energy-consuming process of the pyrolysis. The requirement for embedded heaters in the coal seam during UCTT would necessitate further drilling and well modification to a CBM production field, but such an effort is feasible given current drilling technology.

UCTT also resembles several *in situ* oil shale retorting processes. Like UCTT, oil shale retorting involves low-temperature, low-heating rate pyrolysis of the oil shale kerogen to evolve hydrocarbons. The retort processes require heating sources to provide energy for the kerogen decomposition. As such, these operations provide a good estimate for the types of energy requirements and heating rates that will be achievable in UCTT processing.

Two oil shale retorting methods may be of interest for guiding UCTT development. One is the so-called "Shell" method, which is being pioneered by Shell Oil Company [Crawford, 2010]. It involves downhole heaters in wellbores that provide conductive heating to the shale formation. The heater technology being developed for this process may resemble the heaters that can be implemented for UCTT. Due to heat transfer limitations, months are required to bring the oil shale seam to sufficient temperature to get oil evolution. A second oil shale retorting method of interest is the

modified *in situ* retort being developed by Red Leaf Resources [Crawford, 2010]. This method requires the construction of rubblized beds of surface-mined shale atop recirculating pipe heaters. The void fraction between rubble pieces provides space for convective circulation of hot gases, speeding the rate of heating. UCTT will be constrained because the targeted coal seams will be too deep for mining, but the importance of convective heating may encourage an increase in fracturing to generate more free space for circulating gases.

The proliferation of nonconventional hydrocarbon production in the last decade provides a favorable suite of technologies for the development of UCTT. Although none of the aforementioned production methods are directly analogous to UCTT, various aspects of each process resemble some portion of the UCTT process. For this reason, the major technical advance needed to develop a UCTT process is likely an understanding of coal pyrolysis dynamics under *in situ* conditions. This will allow existing technologies to be redesigned to the specific chemical and mechanical properties of coal.

Supporting Technologies

Two important technologies that have become important to modern hydrocarbon production may prove important to underground coal thermal treatment. These technologies, slant drilling and hydraulic fracturing, have proliferated in recent years due to the need to access and produce from increasingly difficult hydrocarbon reservoirs [Bourgoyne, 1986]. Although both techniques were developed for conventional petroleum and natural gas production, they are applicable to the scenario presented by UCTT production.

Directional drilling is a technique that allows the borehole to be deviated from the initial perpendicular angle to the surface [Bourgoyne, 1986]. Although the borehole cannot be shaped into a sharp right angle, the drill can be curved into a horizontal plane in a short distance. The technology has advanced enough that drillers have a high degree of control over the inclination and azimuthal angle of the drill bit. Consequently, it is possible to drill wells that naturally match the strike and dip of a coal seam. This is important if downwell heaters are to be placed in a UCTT operation beneath a nonhorizontal coal seam.

Hydraulic fracturing (or "fracking") is another production technique that could encourage UCTT development. Fracturing involves the targeted pressurization of a hydraulic fluid to induce fracture of a chosen rock stratum [Bourgoyne, 1986]. Subsequent to fracturing, a propant material is injected into the fracture to mechanically support the overburden while maintaining a higher permeability in the fracture space. The purpose of fracturing is to increase the overall permeability of a producing reservoir. This technology is responsible for the sudden upswing in natural gas production in the past decade. Fracking will probably be important for UCTT because increased permeability for fuel evolution and more void space for convective heat flow will benefit the overall production efficiency.

Expected Advantages of UCTT Adoption

The wide-scale adoption of UCTT may be driven by several environmental advantages that arise from performing the pyrolysis in an *in situ* setting. The suggested environmental benefits highlight some of the key differences between coal pyrolysis and

more traditional combustion or gasification. Some of these anticipated benefits are described below.

High H:C Ratio Fuels

Pyrolytic decomposition of organic materials such as coal tends to naturally favor hydrogen removal over carbon removal [Solomon, 1992]. The result is an enrichment in H:C ratio in the evolved gaseous and liquid fuels and a corresponding decrease in the H:C ratio of the residual solid phase. In effect, pyrolysis serves to selectively remove the "high value" carbon that carries the hydrogen while retaining the lower value carbon underground. When compared to UCG, which removes virtually all carbon from underground, UCTT would lead to a far smaller amount of the processed coal's carbon content ultimately being evolved to the atmosphere by use of the produced fuels.

Reduced Sulfur Emissions

Low-temperature pyrolysis will not tend to mobilize large amounts of sulfur from the coal structure. There will be some organic sulfur that is susceptible for release; however, the inorganic sulfur content is unlikely to be released unless temperatures exceed 900^{o}C. Minimization of sulfur release prevents several problems, including reduced steel corrosion and reduced atmospheric pollution.

Reduced Groundwater Contamination

Due to the residual fixed carbon matrix and small amounts of ash transformation, low-temperature pyrolysis is unlikely to create much in the way of mobilized heavy metal species. The fixed carbon may be able to act like a molecular sieve that prevents the movement of metals and organic species into the surrounding aquifers. In comparison,

UCG leaves little residual carbon in oxidized zones and has been shown to emit some aromatic species to surrounding aquifers [Shafirovich 2009]. UCTT should pose less of a concern for contaminating surrounding groundwater supplies.

Minimized Surface Subsidence

The residual carbon matrix from a UCTT process should fill most of the subsurface volume occupied by the original coal seam, preventing the collapse of overburden into any cavity space. Surface subsidence has been a major challenge to UCG due to the near-complete removal of coal from the seam, but this should not be the case during UCTT.

Potential CO_2 Sequestration Reservoirs

UCTT should alter the physical properties of the treated coal seam enough to enhance the potential for CO_2 sequestration. Pyrolysis will likely increase the internal surface area and total pore volume of the coal, creating a larger capacity for CO_2 adsorption on the coal surface. There will also likely be seam permeability increases via a variety of mechanisms, including pore enlargement, thermal fracturing and hydraulic fracturing. This will facilitate the transfer of CO_2 into the coal formation after the completion of UCTT processing. As conceived, UCTT is intended to have a low carbon footprint by producing low-carbon fuels and offering sequestration space for the carbon that is ultimately emitted.

Technical Challenges in UCTT Development

Several technical challenges face the development of UCTT before it could be implemented in the field. Although these challenges are likely analogous to those that

have been solved in other parts of the oil and gas industry, the fundamental chemical and physical differences between coal and other kerogen-containing formations will need to be better understood before methods can be adapted for UCTT. Some of the anticipated challenges are discussed below.

Heat Transfer and Heater Design

Perhaps the most critical technical challenge to UCTT development is the efficient movement of heat into the coal seam. Sufficient heat will need to be provided to achieve pyrolysis temperatures (>300^{o}C) and losses to surrounding rock layers will need to be minimized. The creation of some void space to allow for convective heating would be ideal, but the method for doing so is not clear. A major factor in the development of seam heating techniques will be the heater design. For example, an RF source may allow for targeted, localized heating without the need for additional void space, but the heater would need to be optimized for the unique electromagnetic absorption characteristics of each coal treated. Likely, drilling strategies and heater designs will need to be codesigned to achieve sufficient heating to get sufficient product output.

Seam Permeability

Sufficient permeability will need to exist to extract fuels in meaningful amounts because this property governs the rate of bulk mass transfer from the coal seam. Hydraulic fracturing will most likely need to be employed to create artificial connections between natural cleats. Increased fracturing will decrease the distance products must travel from regions of low permeability to high. This dissertation seeks to bolster the

understanding of how permeability will develop in the large coal domains that will exist between fractures.

Product Evolution and Contamination

A better understanding of coal pyrolysis products under *in situ* conditions will be necessary to develop surface extraction techniques. Liquid products derived from coal will differ substantially from conventional crude oil, so traditional extraction methods may not work. Further, it is unclear in what quantity these liquids will be produced and if they are of value commercially. If they are not extracted, groundwater remediation will be an increased concern as the coal liquids will contain aromatic species that will have contamination issues.

Reservoir Modeling

The most efficient process design and implementation will require high-precision modeling as has been used throughout the oil and gas industry. As yet, insufficient pyrolysis data exist under relevant conditions to develop a model for the UCTT process. Coal pyrolysis will need to be examined under high-pressure and high-loading conditions to determine what kinetic data will be sufficient for describing *in situ* decomposition. Additionally, mass transfer and heat transfer will need to be described rigorously in large blocks. The very high organic content of coal will likely couple together kinetics, heat transfer and mass transfer more tightly than in other hydrocarbon production methods. Fundamental studies will need to be performed to detail the nature of this coupling and quantify it for modeling purposes.

Comparison of UCTT to Conventional Coal Pyrolysis

Coal pyrolysis is a very well-studied subject; however, it is unclear how applicable much of the preceding data are to UCTT processing due to the unique constraints imposed by working underground. Traditionally, coal pyrolysis has been studied to understand the devolatilization process that was crucial to the description of particle combustion in coal flames. As such, coal pyrolysis studies typically focused on coal particles at sizes typical of the crushed or pulverized coals that were fed into furnaces, typically in the range of microns to millimeters. In these studies, mass transfer studies often focused on determining the particle size beyond which mass transfer resistances could not be ignored [Solomon, 1992]. Kinetic studies were then performed on particles below this threshold size so that the data could be interpreted as the primary pyrolysis kinetics (free from secondary effects during mass transfer). The purpose was, in essence, to determine the rate-limiting step in volatile evolution to the coal flame as a function of particle size and thermal history.

In contrast, the relevant length scale for study in UCTT-type pyrolysis will be in the range of centimeters to meters. On this scale, it is a given that mass transfer effects cannot be ignored. Further, *in situ* operation will add other constraints to the pyrolysis conditions, such as an elevated hydrostatic pressure, and horizontal and vertical loading created by the volumetrically-confined conditions of the deep coal seam. Fundamental studies will be necessary to determine whether these constraints have major or minimal impacts on the devolatilization and mass transfer behavior during pyrolysis. The research presented in this dissertation stands as a bridge between conventional coal pyrolysis and the processing regime anticipated in UCTT. It should provide some guidance as to the

importance of certain effects on mass transfer in large coal particles at the types of heating rates that will be typical of a UCTT process.

Summary

The subject of mass transfer in large coal domains has been introduced as important to the description of underground coal thermal treatment, a proposed method for producing hydrocarbon fuels from deep coal seams. A conceptual description of UCTT has been given and the process has been compared and contrasted to other *in situ* processing technologies, including underground coal gasification and coal-bed methane production. The anticipated benefits of adopting this technology have been described, as well as some remaining technical challenges that will need to be solved before implementation. The differences between underground coal pyrolysis and conventional pyrolysis have been highlighted to provide context for the importance of the work presented in this dissertation.

CHAPTER II

LITERATURE SURVEY AND ANALYSIS

The purpose of this chapter is to provide an overview of the relevant technical literature to underground coal thermal treatment and identify the key fundamental issues that need to be addressed. The current status of several *in situ* processing methods are discussed, followed by an overview of coal pyrolysis. Finally, lingering questions will be identified and the novelty of the research presented in this dissertation will be described.

Current Status of *In Situ* Production Processes

Underground Coal Gasification

UCG is perhaps the most actively researched method for obtaining fuel gases from deep coal seams. Shafirovich and Varma [2009] give a substantial overview of the historical development of UCG dating back to Soviet efforts in the 1930s. U.S. efforts peaked in the early 1980s although an active modeling group remains at Lawrence Livermore National Laboratory. The modern focus for UCG field research has largely shifted to Asia and Australia in particular, where a pilot plant at the Chinchilla coal field in Queensland has demonstrated direct gas-to-liquid hydrocarbon production from a gasification test site.

Although UCG is a proven technology for producing syngas from deep coal seams, there is still substantial effort being put into developing improved methodologies

for constructing gasification sites and managing the active gasification process. One such development is the so-called CRIP method (controlled retracting injection point), which utilizes an injection well and a production well linked by a lateral well immediately beneath the coal seam [Hill, 1986]. Retractable tubing is fed into the well, allowing an injector to be precisely located beneath the coal seam. This gives the operator control over the location and extent of gasification. The injector can subsequently be repositioned to resume gasification at a new site. In 2012, a newer process was proposed, called SWIFT (single-well integrated flow tubing) [Porter, 2012]. This process utilizes a single large well for injection and extraction via networks of coiled tubing. In principle, its implementation would greatly reduce the amount of drilling required to achieve a UCG operation.

UCG is still being actively researched on a number of fronts that primarily pertain to the selection of candidate seams for optimal operation. Because UCG research is now primarily conducted in the field via complicated drilling operations, it is quite expensive and time-consuming to test new ideas. Areas of active research include optimal seam depth, optimal seam dip and groundwater containment strategies.

Estimates of optimal seam depth have ranged from 12m to 1200m, depending upon the selection criteria. Burton *et al*. [2006] suggested 200m as a minimum working depth based upon the availability of potable groundwater below that depth. 300m has also been suggested due to decreased amounts of surface subsidence. At working depths beyond 800m, CO_2 sequestration becomes more favorable in the gasification cavity and the increased hydrostatic pressure has been shown to increase the yield of methane,

leading to a higher heating value gas [Green, 1999]. However, deeper operating depths increase drilling costs, creating a tradeoff.

Seam angle is not seen to be an important design parameter when selecting a UCG candidate seam. There have been studies suggesting that shallow dipping seams promote drainage and hydrostatic balancing in the gasification zone [Sury, 2004]. Shallow dip also ensures that falling debris caused by subsidence of other forms of cavity collapse will not damage well infrastructure. However, other tests in steeply dipping seams did not show any negative effect resulting from the high angle [Kreinin, 2004].

Groundwater contamination is also a major design concern since environmental regulations in most regions limit the process waste that can enter potable aquifers. Sury *et al*. [2004] have suggested a 25m buffer between a candidate coal seam and the nearest overlying aquifer to ensure no process contamination. This rule of thumb is general and does not account for the unique stratigraphic scenarios presented by each coal seam, for example the presence of surrounding impermeable shale layers. UCG operations have been conducted in seams with smaller buffers between the seam and the nearest aquifer.

Recent years have also seen an increase in the efforts to create large-scale reservoir simulations of UCG processes. Perkins and Sahajwalla [2005; 2006; 2007] developed and refined a two-dimensional model that sought to demonstrate more accurately the physical phenomena in the growing gasification cavity during operation. This model demonstrated the importance of buoyancy effects in relation to product yield based upon the point of oxidant injection. Injection low in the cavity gave greater yields of syngas because the cooler oxidant was less likely to interact with the rising combustion gases. More recently, Seifi *et al*. [2011] published a three-dimensional model of UCG

using the CRIP method. Again, this model attempted to refine the transport phenomena to demonstrate how long-distance effects alter or enhance results from what is observed in laboratory gasification experiments.

Coal-Bed Methane Production

CBM is seen as a very close analogue to UCTT and many of the technologies developed for it will likely enable *in situ* coal pyrolysis. The U.S. is currently the leading producer of CBM-derived natural gas with annual production of nearly 2TCF [Pashin, 2011]. Although U.S. production in the 80s and 90s primarily involved high-rank reservoirs such as the San Juan Basin, the expansion into low-rank sources such as the Powder River Basin have swollen proven U.S. reserves. CBM involves the extraction of naturally occurring light gases that become trapped within buried coal seams. The gases can arise from thermogenic or biogenic pathways depending upon the reservoir characteristics. Trapped gases largely exist as adsorbed species on the coal surface within the massive internal pore network of coal [Moore, 2012]. Consequently, permeability is important to understanding the transport processes of CBM just as it will be in UCTT. Enhanced coal-bed methane (ECBM) is an emerging technique for boosting CBM recovery that may also be relevant for UCTT in the context of carbon sequestration. This section will discuss some technological developments in CBM/ECBM that may impact UCTT development.

CBM has spurred substantial development of subsurface coal seam drilling and production methods. CBM sites utilize both vertical and horizontal wellbores with the horizontal ones acting as drainage channels to the vertical ones. A large effort has been put into understanding the mechanical stability of both bore types in coal beds [Gentzis,

2009a; Gentzis, 2009b; Gentzis, 2009c; Han, 2009; Nie, 2012]. These studies enhance the necessary knowledge for laying out UCTT production sites and bolster the notion that CBM sites are well-equipped to be adapted to UCTT after CBM production is complete. CBM has also utilized hydraulic fracturing for permeability development in coal seams, to mixed effect. Close [1993] has suggested that the natural permeability of coal cannot be enhanced; however, fracking has still been employed to improve connectivity between cleats. The difficulty with enhancing permeability in coal is to derive from the ductility of coal, which naturally tends to reseal induced fractures. Proppants can be deployed although these increase the expense of fracking operations.

Due to its importance in CBM operations, the development of *in situ* permeability models has been vital to reservoir modeling efforts [Pan, 2012]. Models have been developed on the basis of porosity and stress/strain relationships. An important effect on seam permeability is the impact of swelling caused by the adsorption of gas species on the coal surface. When desorbed, the coal matrix shrinks, ultimately increasing the permeability. The models of Cui and Bustin [2005], and Connell *et al*. [2010] have attempted to empirically describe the effect of pore shrinking on permeability via different assumptions about the *in situ* stress/strain relationships. The growth in understanding of coal permeability is important to UCTT because it will help to guide development of permeability models for coal domains during pyrolysis.

ECBM is also a developing technology that can impact the development of UCTT. It involves the use of injected carbon dioxide to enhance methane yields from a coal seam. Because CO_2 preferentially adsorbs to coal over methane, its injection into the coal's pore system promotes gas exchange [Mazzotti, 2009]. The concept is favorable

because it not only promotes enhanced yields of methane, but it also results in the sequestration of carbon. A similar idea has been proposed with UCTT after pyrolysis increases the size of the coal's pore system. An unfortunate consequence of CO_2 injection is swelling, an effect that is known to decrease the seam permeability [Larsen, 2005]. This effect appears to occur early in the injection process due to the high pressure of injected gas. An improved understanding of swelling effects on the permeability of pyrolyzed coal will be necessary to understand whether UCTT is a potential option for facilitating CO_2 sequestration into coal seams.

Coal and Oil Shale *In Situ* Pyrolysis

Few studies have been performed to examine the pyrolysis behavior of coal under simulated *in situ* conditions. Some results can be gleaned from coal pyrolysis studies aimed at other applications. A greater body of work has been performed on oil shale under simulated *in situ* conditions, but the substantial chemical differences between coal and oil shale make the extrapolation of results difficult. The known *in situ* oil shale research does offer some insight into possible heater technology for UCTT applications.

The most directly relevant *in situ* coal pyrolysis studies were those performed by Westmoreland and Dickerson at Oak Ridge National Laboratory in the late 1970s [Westmoreland, 1980]. Pyrolysis was studied in large blocks of bituminous coal and lignite with the intent of understanding the gaseous product distribution. It was observed that the quantity of oxidized species (e.g. CO, CO_2) could not be produced purely from the native oxygen content of the coal, leading to the conclusion that self-gasification from the natural coal moisture was an important factor in influencing the final product distribution. This conclusion is supported by more recent modeling work by Yip *et al*.,

who showed that self-gasification by coal moisture as well as pyrolytic water was an important component of coal pyrolysis in certain coals [Yip, 2009]. Of additional relevance to *in situ* pyrolysis of coal is a claim made by Wellington *et al*. in a patent filing for Shell Oil that the thermal conductivity of confined coals is higher than published values for powdered coals [Wellington, 2003]. This claim has never been quantitatively proven in a peer-reviewed source.

Oil shale has also received an extensive amount of public and private research investment due to the massive resources located in the U.S. The United States are estimated to have 6 trillion barrels of recoverable oil shale reserves, with 75% of that residing in the Green River formation of Utah and Colorado alone [Knaus, 2010]. It is also currently estimated that 2 trillion barrels worth of the proven reserves will be produced as high-value crude oil with a similar composition to that of conventional petroleum. Like UCTT, the biggest challenge in oil shale production has been developing methods to convert nonextractable formations into recoverable fuels via *in situ* processing. Although the chemistries of coal and oil shale are different and quite complex, the engineering methodology likely provides insight for how to achieve UCTT conditions. Of interest are the *in situ* and modified *in situ* methods currently being developed for oil shale retorting.

In situ methods for oil shale retorting involve any technique that does not substantially alter the kerogen-containing formation. The most well-known example is the Shell *In Situ* Conversion Process (ICP), which is currently being piloted in western Colorado [U.S DOE, 2008]. ICP utilizes vertically-oriented electrical heaters to achieve pyrolysis temperatures over several years. The slow heating is said to produce a lighter

product oil that requires less upgrading than more rapid retort methods. Shell has also deployed a so-called Freezewall technology in conjunction with ICP to prevent the contamination of surrounding aquifers. The Freezewall surrounds the heated zone with a barrier of frozen rock to prevent the movement of metal and organic species. After oil production, a thorough steam flushing treatment will be used to remove these environmentally sensitive species before the freezing zone is brought back to ambient temperature.

Other researched *in situ* oil shale production methods utilize hydraulic fracturing to achieve improved heat transfer. The Chevron CRUSH process uses fracking to achieve a larger and more uniform permeability through which hot circulating gases are used to promote convective heating of the sediments [Chevron, 2006]. ExxonMobil has proposed a second method called ElectroFrac [Crawford, 2010]. This method involves filling induced fractures with an electrically-conductive material that becomes a resistive heating element when current is applied. This method is potentially low-impact at the surface but will require substantial amounts of electrical power to produce process heat.

It should also be noted that oil shale research has prompted substantial research into radio frequency (RF) heating. This is an electromagnetic dissipation method that utilizes specially tuned RF emission systems to create a more uniform heating throughout the heated volume. The idea was originated at Lawrence Livermore National Laboratory in the 70s and eventually transferred to Raytheon for commercial development [Burnham, 2003; Crawford, 2010]. The IP is now held by Schlumberger for commercial deployment. RF heating is estimated to heat shale at nearly 50 times the rate of

conduction heating; however, it requires approximately the equivalent of 1 barrel of oil for every 5 barrels it produces.

Modified *in situ* oil shale processes are also in development. These processes are characterized by more substantial alterations to the seam to improve heat transfer. In one method developed by Occidental Petroleum, horizontal wells were created beneath the shale deposit via mining [Lee, 2008]. The shale formation was then explosively blasted to collapse it into the void space, creating a rubblized bed of shale. A downward burning combustion was then achieved to push retorted oil toward drainage channels beneath the rubblized bed. Red Leaf Resources has also created a modified *in situ* process that requires surface mining shale deposits [Crawford, 2010]. After mining to create an open pit, the pit is lined with an impermeable barrier and filled back in with rubblized shale and piping. After capping the shale bed, the piping is used to circulate hot gases that achieve conductive heating. The void space created by rubblization is known to speed heating via natural convection.

Fundamentals of Coal Pyrolysis

Coal pyrolysis is a very well-studied subject due to its central role in describing the burnout of coal particles during combustion. Many extensive reviews have been written on the subject of coal particle pyrolysis comprising hundreds of studies on various aspects of the chemistry. These reviews including the works of Howard (overview of pyrolysis and hydropyrolysis) [Howard, 1981], Solomon (pyrolysis mechanism) [Solomon, 1993] and Yu (particle porosity and morphology changes) [Yu, 2007]. Collectively, these reviews provide a very thorough background on coal pyrolysis although their applicability to UCTT is uncertain due to the complications presented by

in situ processing. The purpose of the following section is to provide an overview of conventional coal pyrolysis. The subsequent section of the literature review will attempt to address what can and cannot be concluded from previous studies.

Devolatilization of Coal Particles

Pyrolysis-induced devolatilization has been a central challenge to describing the burnout of coal particles during combustion. Until devolatilization is complete, the pyrolysis reactions create a pressure gradient through the particle, driving volatile species out into the combustion zone surrounding the particle. As such, oxygen cannot begin oxidizing fixed carbon in the coal particle in substantial amounts until devolatilization is complete. Thus, a thorough description of devolatilization and the pyrolysis reactions that drive it are crucial to describing the combustion of coal particles. Consequently, a large effort has been invested in understanding the many parameters that affect coal pyrolysis as well as the composition and morphology of coal particles after devolatilization is complete. This section summarizes some key observations on coal pyrolysis in small particles.

Mechanism of coal pyrolysis. Due to the heterogeneous structure and composition of coal, as well as thousands of possible reaction pathways, an elementary description of the reaction mechanism of coal pyrolysis is virtually impossible. Rather, a more global description of the pyrolysis mechanism can be given and the specific reactions can be classified into nine broad categories. To create a standard nomenclature, the community has generally accepted that coal pyrolysis can be thought to occur in two distinct steps: primary and secondary pyrolysis. Primary pyrolysis is considered to be the low-temperature reactions that fragment the solid structure and give rise to most of the

tars as well as some light gases. Secondary pyrolysis consists of higher-temperature reactions that primarily produce light gases. During primary pyrolysis, the coal structure fragments into a more fluid structure known as the metaplast. During secondary pyrolysis, this structure will anneal into a char containing fixed carbon and mineral matter. It should also be noted that tar coking reactions are not classified as secondary pryolysis; rather, these reactions are, in effect, pyrolysis reactions of primary pyrolysis products and are consequently governed by their own complex mechanisms.

It has been proposed that coal pyrolysis reactions can be broadly categorized into nine categories. These categories include all the reactions leading to the three types of pyrolysis products (gas, liquid and char). The nine categories of pyrolysis reactions can be summarized as [Solomon, 1993]:

Step 1: Disruption of the hydrogen bonding network.

Step 2: Vaporization of noncovalently bonded molecules. This would include the desorption of species such as methane and carbon dioxide that preferentially adsorb to coal.

Step 3: Low-temperature cross-linking of the coal's solid phase, primarily in low-ranking coals.

Step 4: Fragmentation reactions that disrupt the structure of the coal.

Step 5: Hydrogen extraction from the coal structure to stabilize fragmented free radicals.

Step 6: Vaporization and gas-phase transport of the small molecules. Steps 4 through 6 include the reactions that will give rise to tar species.

Step 7: Moderate-temperature crosslinking to resolidify the coal structure. This step closes primary pyrolysis, giving rise to coal char.

Step 8: Decomposition of small functional groups to produce light gases. These reactions give the secondary pyrolysis products.

Step 9: High-temperature elimination of hydrogen to condense the coal char network.

At atmospheric pressure, the temperature region for primary pyrolysis can generally be considered to occur between 300 and 600^{o}C. Above 600^{o}C, secondary pyrolysis reactions begin to dominate, leading to greater gas yields. Tar coking reactions are generally not considered important until temperatures above 500^{o}C, although an acceleration in the rate of tar coking does not really occur until nearly 700^{o}C [Serio, 1987]. Mass transfer and pressure effects do complicate these basic trends, as discussed in a later portions of this review. Part of the difficulty in extrapolating these basic particle results is assessing how multiple effects will interact simultaneously. A UCTT-type pyrolysis can be expected to have mass transfer, heat transfer, pressure and confinement effects at relatively low temperature and heating rate. No known studies have looked at all of these effects simultaneously.

Effect of temperature on pyrolysis. The overall volatile yield is known to increase during pyrolysis as the maximum ultimate temperature increases [Dryden, 1957]. This effect is strong up to approximately 1000^{o}C, beyond which smaller volatile yields are realized for subsequent increases in temperature [Howard, 1981]. There is some heating rate correspondence to this effect because at lower heating rates, there is competition between devolatilization/transport processes and char condensation, limiting the amount of free volatiles at higher temperatures.

Compositional data for gas and liquid pyrolysis products based upon temperature tend to vary based upon the coal type and heating rate used. For example, Tyler reported

peak tar yields before 600^{o}C at an 10K/s heating rate [Tyler, 1980] while Suuberg reported a tar peak close to 1000^{o}C at a heating rate of 1000K/s [Suuberg, 1977]. The later case is attributed to mass transport limitations in the coal particle. In general, it should be noted that tar and light hydrocarbon yields appear to be most sensitive to the ultimate temperature. Other products, for example hydrogen sulfide and pyrolytic water, are weaker functions of temperature with only minor increases at elevated temperatures [Howard, 1981].

Effect of heating rate on pyrolysis. Heating rate does affect the overall volatile yield although the effect is fairly minor when held to within two orders of magnitude in rate. Datasets by Berkowitz and Eddinger *et al*. show a 15% increase in the total volatile yield when the heating rate increased from 10^{-1} to 10^{5}F/s [Berkowitz, 1985; Eddinger, 1966]. It is notable that the total volatile yield at very high heating rates can exceed the value given by proximate analysis. Howard defined a Q value that is the ratio of the maximum yield to the proximate analysis yield. He found the Q value to correspond to the coal swelling behavior, with nonswelling coals having a value of 1.3-1.5 and strongly swelling coals to have a Q value of up to 1.8 [Howard, 1981]. This effect may be attributed to the extensive cleavage and transport of organic fragments that occurs before char condensation reactions can occur. This idea is bolstered by increased tar yields, which suggests that transport rates exceed reaction rates at the fastest rates of heating.

Effect of pressure on pyrolysis. Pressure is known to suppress the overall volatile yield from the pyrolysis of coal particles. Suuberg demonstrated the impact of pressure on the specific yields of various pyrolysis products [Suuberg, 1977]. The overall volatile yield in the pyrolysis of a Pittsburgh No. 8 bituminous coal was seen to drop 15 percent

when the pressure rose from 1 atm to 100 atm during pyrolysis at 1000^{o}C. The most dramatic decrease in yield was found to originate from tars, while hydrocarbon gases actually increased. This effect was attributed to mass transfer effects. The increased external pressure suppressed pressure driven flow from the particle, increasing the residence time of tars. This, in turn, increased the likelihood of tar coking reactions, leading to a decrease in tar and a concomitant increase in light gases. The general trend of decreasing volatile yields with increasing pressure is contradicted by the work of Lewellen on a nonswelling Montana lignite [Lewellen, 1975]. He observed no correlation between pressure and yield. This result perhaps further underscores the importance of the mechanism of mass transfer in determining the final products of coal pyrolysis at elevated pressures

Coal Porosity Changes During Pyrolysis

The internal structure of coal is known to change during pyrolysis, affecting the permeability. The description and classification of void structures within the solid matrix of the coal is quite complex, as is the classification of different deformations that occur in pyrolysis. The purpose of this section is to describe some general principles of coal structure and characterize the relevant morphological changes that are induced by pyrolysis.

Native porosity of coal. Coal is a naturally porous medium although the nature and extent of available void space is tied to the composition, rank and geological history of the coal throughout the coalification process. In general, porous structures become smaller and more condensed as the coal matures and compression from overburden increases. The native porosity can be classified in three different categories: fracture

porosity, phytereal porosity and matrix porosity [Gamson, 1993]. Each type arises from different aspects of the coal composition and depositional history.

Fracture porosity is the void space within the coal structure created by stress-induced fractures. Depending upon size, these fractures can be resolved into macrofractures and microfractures. The macrofractures, referred to as cleats, are typically visible without magnification and can be up to millimeters in width. They orient perpendicular to the bedding planes of the coal (layering due to the original deposition of organic material in ancient bodies of water) and are usually infilled with mineral matter, reducing the permeability of these structures. Microfractures are smaller structures that are mostly on the micron scale. They tend to have more complex orientations as they can align with or oppose the larger cleats. The microfractures often connect cleats and can be a major source of permeability in the coal structure.

Phytereal porosity is the portion of coal porosity that is attributed to the ancient capillary structure of deposited plant materials. Because plant vessels were often bundled in extended clusters, phytereal pores are often found in close proximity to each other. These pores are notable for undergoing a sequenced process of breakdown and collapse as the coal ages, leading to a steadily evolving morphology. Initially, the plant vessels are able to withstand the compressive forces caused by overburden, leading to an elastic flattening of the vessels. Once a threshold compressive stress is achieved, the vessels will buckle then collapse. Further compression will further flatten what pore space remains. In effect, the phytereal pores are seen to transition from rounded structures to irregular elliptical structures, and eventually narrow slits as coalification continues. Consequently,

the amount of porosity contributed to coal by phytereal structures lessens as the coal ages. These pores are typically on the size of microns to tens of microns in width.

Matrix porosity is any porosity associated with discontinuities between individual particles in the coal structure. Common examples of matrix porosity include pores formed by the interface of granular maceral components and pores formed by the interface of clay particles. These pore structures tend to be smaller with sizes up to the micron scale. Their frequency is heavily dependent upon the quantity of granular macerals and mineral inclusions in the coal.

Although the aforementioned three categories of porosity compose the readily observable forms of macroporosity by SEM imaging, coal also contains even smaller structures that comprise the micro- and mesoporosity of the structure. Basic observation of permeability suggests that these structures are quite irregular in shape, size and length and occasionally sealed off from the connected pore system, creating dead ends for mass transport. Consequently, creating a precise description of coal permeability is difficult and will need to arise from direct measurements over length scales long enough to capture the characteristic heterogeneity of a particular coal's structure.

Porosity changes during pyrolysis. As with the native porosity of coal, the changes that occur to the porous system largely depend upon the coal being studied. Pyrolysis can induce changes to the coal structure through the removal of mass, reorganization and condensation of the char structure, coking of tars and plastic deformation. Low rank coals tend to have more extensive pore systems, increasing the ability to transfer mass during pyrolysis. As the rank increases, the pore system is less able to accommodate mass flow during devolatilization, leading to pressure increase and

swelling in the pore structure [Yu, 2007]. This is the root of plastic deformation. Once a coal has become an anthracite coal, the volatile content has dropped to an extent that the available pore system is again sufficient to transfer mass during pyrolysis. Consequently, plastic behavior is seen to peak in bituminous coals.

Plastic deformation is theorized to occur via a bubble mechanism. As pyrolysis products are devolatilized into the pore space, they accumulate and the pore pressure builds. Simultaneously, the fragmentation of the coal structure softens the coal solid, creating the more deformable metaplast phase [Solomon, 1992]. Eventually, the pressure exerted by the vapor bubble exceeds the strength of the coal structure, leading to bubble rupture through the coal. As individual bubbles travel through the deforming coal, they likely coalesce. Plastically-deformed coals are distinctly characterized by their large open pores, giving them a sieve-like appearance. In a bituminous coal, whose initial porosity is quite limited, the morphological change is dramatic and distinct with open pores of tens to hundreds of microns in width.

There are many other classifications of morphology changes caused by pyrolysis with distinctions being quite complex. Yu *et al*. provide an overview of the characteristics and nomenclature of these structures [Yu, 2007]. It is important to note that these results are typically taken from particle studies where individual particles are often composed of a single maceral species and resultant changes may be specific to that one group. Single particles are also prone to fragmentation, especially at high heating rates. Consequently, the single particle effects that govern porosity changes during pyrolysis may not apply to large coal particles where the overall structural strength and size may affect the physics that give rise to the changes.

Mass Transfer Effects in Coal Pyrolysis

Mass transfer within a coal particle is a complex subject that is difficult to decouple from the actual pyrolysis chemistry itself. The ability to evolve pyrolysis products from the coal structure depends on various properties, including the existing pore network and the swelling behavior of the coal, but these properties do not remain constant because of the ongoing pyrolysis. Further, the transport of devolatilized species is complicated by the fact that the porous medium, the coal char, is itself a reactive component that participates in pyrolysis reactions. Consequently, certain intrinsic mass transfer effects are inherently built into measured kinetic rates and experimental conditions must diverge widely from typical conditions (e.g. very high heating rate) to see mass transfer effects actually become the rate-limiting step.

The purpose of this section is to highlight some of the mass transfer effects that have been observed during the pyrolysis of coal particles. These effects include internal and external diffusion effects, as well as Knudsen flow in the micro- and mesopores.

Internal flow in pyrolyzing coal particles. Internal flow is the dominant mass transfer process in coal pyrolysis [Solomon, 1992]. The importance of the internal movement of pyrolysis species tends to depend upon whether they are gaseous or liquid at room temperature. Russel *et al*. presented measurements of both diffusional and bulk flow movement of gaseous species and found that, in general, the time-scale for evolution from particles no larger than 100μm was on the order of 10^{-3}s [Russel, 1979]. This study suggests that the coal pore system is capable of handling mass transfer of light volatiles in all but the cases of extreme heating rate. Thus, mass transfer is generally not considered important for describing gas evolution, even in softening coals.

The dynamics of liquid evolution from pyrolyzing coal particles are far more complex. The mechanism for movement of these species will depend upon whether the coal is nonsoftening (pore transport) or softening (bubble transfer) [Solomon, 1986]. Additionally, the phase equilibrium of the tar phase plays an important role in mass transfer because the pressure accumulation in the pore can drive tars into the liquid phase. As the pyrolysis pressure lessens, lower molecular weight species will preferentially distill from the liquid phase, leading to transient changes in the tar composition over the course of pyrolysis. The hindered nature of tar evolution also encourages tar coking reactions that in turn increase the yields of char and light gases [Yu, 2007]. The competition between transport from the coal particle and reaction with the coal char can lead to the picture of tar evolution as a plug-flow reactor system. Increased pressure or larger particle size serve to increase the effective residence time in the reactor, leading to greater amounts of coking and lower tar yields. A notable exception is bituminous coals, where explosive bubble eruption rapidly transports tars from the coal particle. Consequently, these softening coals show the highest tar yields per weight [Solomon, 1992]. For the system studied in this dissertation, it is difficult to identify the extent of mass transfer limitations despite the large particle sizes because of the very low temperatures and slow heating rates utilized in the studies.

External flow from pyrolyzing coal particles. External flow of pyrolysis products from coal particles is generally regarded as a minor effect and generally not relevant to explaining experimental outcomes [Gibbin, 1989; Serio, 1987]. The primary concern external to a pyrolyzing coal particle is deposition of evolved tar cokes. Typical pyrolysis systems will feature a flowing gas that serves to sweep products from the reactor. At even

normal flow rates, the boundary layer surrounding the particle is sufficiently small that residence time, assuming diffusional control, will be on the order of less than 1s. Once into the bulk flow created by the sweep gas, the residence time in the high-temperature zone is likely to be short. Thus, unless the experiment is occurring at extremely hot temperatures or the reactor has a very long residence time through an extended coal bed, the evolved tars are unlikely to coke on the surface of surrounding coal particles.

Knudsen flow in micro- and mesopores. A final consideration for mass transfer effects in coal particles is the flow in the smallest pores. Knudsen flow is a form of mass transfer considered to only occur in pores below 50nm [Pant, 2012]. It occurs when the mean free path of a gas molecules is considerably longer than the pore diameter, meaning that a collision with the pore wall is more likely to occur than a collision with another gas molecule. In effect, wall collisions provide a frictional resistance to gas movement, limiting their rate of movement through the pore. This effect can be seen in both diffusion and pressure-driven flow in micro- and mesopores.

Careful studies have not been performed on Knudsen effects in coal although it is generally accepted that transport resistance in micropores is an important hindrance to the rate of gas evolution in coals. Measurements have been made in shales and mudstones, providing some basis for the Knudsen diffusivity that dictates the rate of gas transport through the pore [Javadpour, 2007; Javadpour, 2009]. It has also been suggested that Knudsen treatments of gas flow also need to consider adsorption effects on the pore surface, although this issue can likely be resolved through the use of an effective Knudsen diffusivity.

Analysis of Prior Work

Determining the applicability of prior coal pyrolysis studies to UCTT is difficult because *in situ* coal pyrolysis physically differs from particle pyrolysis in several key respects. Conventional particle pyrolysis studies have confirmed the impact of temperature, heating rate, external pressure and particle size. However, no study has ever attempted to look at the results of coal pyrolysis with all of these effects occurring simultaneously with the addition of mechanical loading to create stress within the coal structure. This is not to say that prior studies are irrelevant to understanding UCTT, but rather to say that it will be necessary to properly simulate *in situ* conditions to better understand which parameters exert a primary influence on the outcome of pyrolysis. For example, pressure is traditionally associated with lowered tar yields due to increased mass transfer resistance promoting tar coking. In UCTT, the operating pressure is assumed to be above atmospheric, but *in situ* temperatures are unlikely to reach the threshold beyond which the kinetic rate of tar coking is much faster than the rate of mass transport.

The uncertainty of extrapolating conventional pyrolysis results to the scenario posed by UCTT presents a large open topic for scientific exploration. Topics that need to be clarified to better determine the utility of prior results include:

- understanding the impact of *in situ* stresses and confinement on the rates of product evolution and product compositions
- understanding the relevant time and length scales for reaction kinetics and mass transport under conditions of low pyrolysis temperatures, very slow heating rates and high pressure

- determining if devolatilization and mass transport during pyrolysis at extremely slow heating rates inhibits tar formation pathways
- assessing nitrogen and sulfur mobilization and ash transformations during long duration, low temperature pyrolysis

A more thorough understanding of these topics would help to guide process design and improve the accuracy of reservoir models. Additionally, a more thorough understanding of *in situ* coal pyrolysis would benefit UCG modeling and implementation.

Originality of the Described Work

This dissertation addresses a weakness in the understanding of mass transport in large coal particles during pyrolysis at slow heating rates. It describes in a semiquantitative fashion the evolution of porosity in large coal particles and coal blocks during pyrolysis as a function of temperature and heating rate. A preliminary study into the effect of confinement on final char porosity will also be presented. The described work also demonstrates the impacts of temperature and particle size on the rates of evolution and ultimate yields of chars, gases and liquids when pyrolyzed at heating rates that are slower than those previously studied. The threshold for plastic deformation will be demonstrated, allowing the estimate of the tipping point between devolatilization and mass transport. Finally, this dissertation will present evidence of a unique pore-clogging phenomenon that inhibits tar evolution at very slow heating. An analysis of Knudsen flow in the coal mesopore system will be presented to estimate the necessary pressure gradient to displace the trapped tars. Due to the large number of parameters examined in this work and equipment limitations, the impact of externally-applied pressure was excluded from these studies. Pressure is likely to be an important focus for future UCTT-related studies.

In total, this dissertation will offer strong evidence for the nature of mass transport in large coal particles under conditions that are similar, though not identical, to those that would be encountered in a UCTT scenario.

CHAPTER III

EXPERIMENTAL APPARATUSES AND METHODOLOGY

This chapter describes the experimental apparatuses used to conduct the described research and the procedures for running the various types of experiments detailed in later chapters. The intent is to provide enough detail on setup and methodology to allow experiments to be replicated by other researchers.

Coal Selection and Storage

All experimental work detailed in this dissertation was focused on a Utah high-volatile bituminous coal. This coal was chosen as a model system for the detailed studies for three primary reasons. First, it is regionally representative of western bituminous coals given its high volatile content, modest sulfur content and low ash content. Utah has both deep and shallow coal seams, meaning it is a candidate for UCTT but is also easy to obtain samples. Second, it is relatively dense but not brittle, making the mechanical properties ideal for cutting, coring and other sample handling procedures. Lastly, the Utah bituminous coals are swelling coals, meaning they show interesting plastic behavior during pyrolysis. This phenomenon was seen as interesting to explore in the context of porosity changes in an *in situ* setting.

Coal samples were obtained from the Skyline Mine in Huntington Canyon near Helper, Utah. Large blocks of at least 3kg in size were obtained from fresh cuttings at the

mouth of the mine. The blocks were not exposed to any precipitation or direct sunshine before they were acquired. Approximately 40 blocks were transported back to the University of Utah for storage adjacent to the combustion laboratory. The blocks were held in a cool, dry room within a large wooden crate to limit their exposure. Blocks were selected from the collection as appropriate to the particular experiment. For example, smaller square blocks were typically selected for block heating experiments while larger, flatter blocks were used for core preparation.

Ultimate and proximate analyses and heating value analyses were performed on three blocks to assess the approximate chemical composition of the selected bituminous coal. The three blocks sampled were used for core-based experiments and the sampling was done from the same part of the block where cores were drilled. Thus, the samples are representative of the coal used in the presented research. Analyzed samples were broken from the main block then ground to approximately 3mm particles. All ground coal from each sample was sent to ensure that there was no selective enrichment during the grinding process. Chemical analysis was performed at Huffman Laboratories in Golden, CO. Results are presented in Table 3.1. The results show a substantial range of moisture and ash content among the three samples. Volatile matter and elemental composition are less variable. As expected, the heating value corresponded to the ash content. In general, the variability of the bituminous coal samples suggests that the coal blocks are representative of the expected heterogeneity within the coal seam.

Table 3.1 Ultimate and proximate analyses of bituminous coal blocks

Property	Block 1	Block 2	Block 3
Fixed Carbon-%	44.96	50.45	41.53
Vol. Matter-%	40.74	42.95	40.22
Drying Loss-%	2.21	2.27	1.91
Ash-%	12.09	4.33	16.34
Carbon-%	67.30	74.46	64.70
Hydrogen-%	5.32	5.67	5.21
Nitrogen-%	1.39	1.58	1.17
Oxygen-%	13.28	13.50	12.09
Sulfur-%	0.62	0.46	0.49
HHV-BTU/lb	12110	13353	11657

Experimental Apparatuses

The following section describes the equipment used to perform pyrolysis experiments, as well as the equipment used to analyze samples after pyrolysis. The actual operating procedures will be discussed in the subsequent section.

Pyrolysis Reactors

Block pyrolyis reactor. The purpose of this reactor was to perform transient heating of large blocks of coal via embedded cartridge heaters. Time-temperature profiles in the block were monitored via embedded thermocouples. Blocks were subsequently sectioned and analyzed to determine the impact of the thermal history upon the coal porosity. The reactor was designed to pyrolyze continuous blocks of coal up to 5kg in size. The main chamber of the block reactor could accommodate blocks of 8”x7” and up to 6” in depth. Figure 3.1 shows a cross-sectional schematic of the block reactor. The size of allowable coal blocks was mainly constrained by the space taken up by electrical and thermocouple wiring.

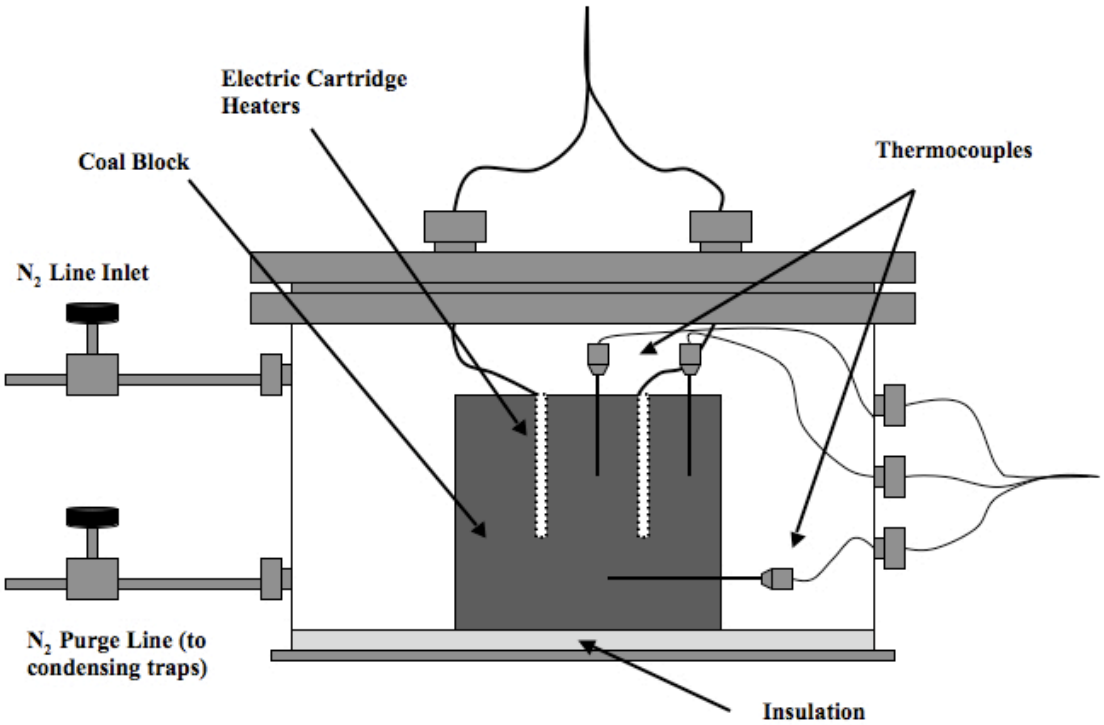

Figure 3. 1 Cross-sectional schematic of coal block reactor

The reactor body was an open, 9” deep, 11” diameter stainless steel cylinder with a welded-on base. The cylinder contained a machined rim that mated to the top flange of the reactor. A silicone gasket provided a seal between the reactor body and the top flange, and six bolts were used to secure the flange to the reactor during operation. The reactor body had four Swagelok ports welded on to it; two were used as feedthroughs for the electrical wiring that carried power to the heaters, and two were used as inlet and purge ports for the sweep gas. The removable upper flange held two Swagelok ports; one used for a feedthrough of the thermocouple wiring and one holding a pressure gauge. The base of the reactor was lined with sand to insulate the block from the reactor body. The outlet port was connected via heated copper piping to a bubbler train for capturing liquid volatiles.

Block heating was achieved via four embedded cartridge heaters. The heaters were ¼” x 3” resistance heaters capable of operation up to 760^{o}C per manufacturer specifications. Two cartridge heaters, manufactured by Tempco, contained type-K thermocouples grounded to the top end of the heater casing. The embedded thermocouples allowed the heaters to be monitored and controlled by a PID system. These heaters were teamed with unmonitored (no thermocouple) heaters manufactured by Omega Engineering. Due to similar resistances, it was believed that the response of unmonitored heaters would be similar to that of the monitored ones, thus two of each were used. The heaters were supplied power via an OPTO-22 PID control system. The OPTO system was coupled to the heaters via the embedded thermocouples. Each monitored heater was wired in parallel to an unmonitored one, allowing the same voltage to be applied to each. The OPTO software was designed to simultaneously ramp both sets

of heaters at a prescribed heating rate to a final temperature, then hold at the final temperature for a prescribed amount of time before commencing a controlled cooling ramp back to room temperature.

Heaters were arranged in a square pattern with each side of the square being 1.5" long. Each heated block also contained three embedded type-K thermocouples for recording the temperature profile at various regions of the block. The thermocouples were also connected to the OPTO system and their output was monitored and recorded for each experiment. The positions of the thermocouples could vary although one was always embedded in the center of square heater pattern. The thermocouples were placed 1.5" deep into the block. Figure 3.2 shows a typical placement pattern for the three thermocouples.

Tube furnace reactor. The tube furnace reactor was used to pyrolyze cored coal samples under more controlled conditions than could be achieved in the block pyrolysis reactor. This reactor was used to prepare samples for porosity analysis and also to collect char and tar yield data. The reactor could accommodate core samples of approximately 0.8" in diameter. The heated zone of the reactor was 12" long, but core samples were typically only 2 to 3" long and 9 to 14g in mass. The core preparation procedure limited the sample size more than the reactor did.

The tube furnace was a Lindberg Blue-M clamshell furnace with a 1" outer diameter. The furnace held a 24" long, 1" O.D. quartz tube that was sealed on both ends by 1" ultra-torr fittings with high-temperature o-rings. The upstream fitting was connected to a rotameter that controlled the sweep gas flow rate. The downstream fitting was connected via copper piping to a glass bubbler train that captured liquid volatiles.

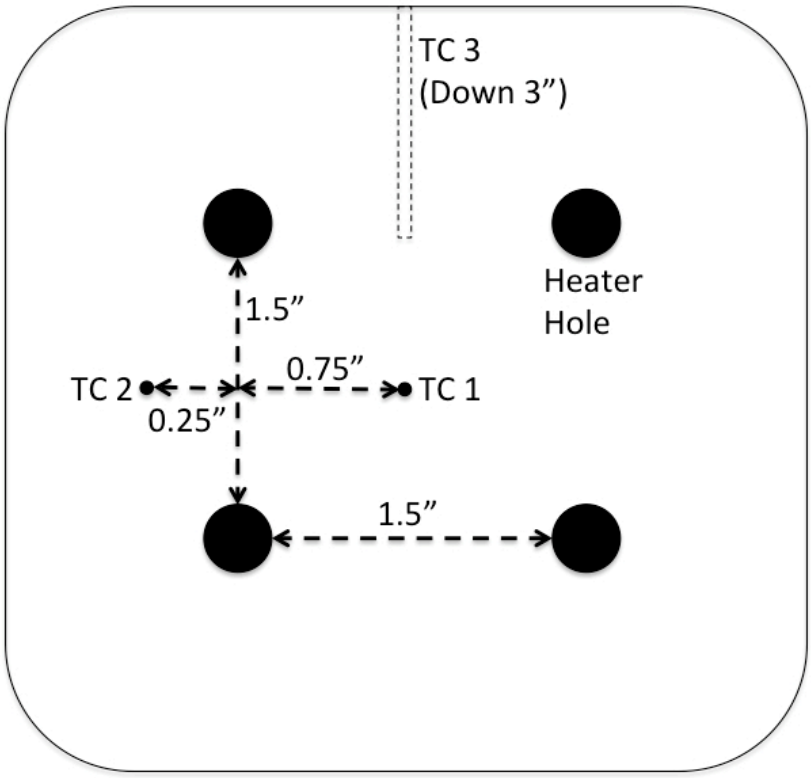

Figure 3. 2 Schematic of heater and thermocouple (TC) locations on coal block top

The metal portions of the downstream piping assembly were heated via heat tape to ensure that condensing tars did not block the flow of gases to the bubblers.

The tube furnace was controlled via a programmable, inline PID system. The furnace was capable of heating at rates up to 100K/min to 1200^{o}C per manufacturer specification. Constant temperatures could be held for up to 100hrs. The temperature was monitored by a single thermocouple that was held close to the surface of the quartz tube. For the purposes of this research, temperatures never exceeded 600^{o}C and the heating rate never exceeded 10K/min to extend the life of the furnace's heating element. Coal cores were positioned in the center of the furnace, adjacent to the thermocouple. A nitrogen sweep rate of 0.5scfh was used for all core experiments. This flow rate corresponded to an estimated residence time of less than 2s in the heated zone of the furnace. Given the relatively low operating temperatures (< 600^{o}C), tar coking reactions were not expected to be significant [Solomon, 1992].

For the collection of tar samples, the quartz tube was positioned in the furnace asymmetrically, such that only an inch of glass was exposed upstream and approximately 10 inches was exposed on the downstream side. The exposed glass was air-cooled, giving a surface temperature of 70^{o}C, allowing tars to condense on the inner surface of the quartz tube. A quartz wool plug placed just upstream from the outlet fitting provided a final surface for condensing any untrapped tars.

Confinement vessel. The purpose of the confinement vessel was to limit the ability of pyrolyzed coal cores to swell in the radial or axial directions during devolatilization. The vessel was composed of a cylindrical aluminum block with a hollow center that matched the outer diameter of the bituminous coal cores. The block was 1"

thick, accommodating cores of approximately 7g in weight. The block and core assembly was capped by two thick aluminum pieces. Nuts and bolts held the entire assembly together during pyrolysis. Two small port holes were drilled in the end blocks to permit the release of volatiles from the vessel.

The vessel was heated in a tube furnace with a 2.5" inner diameter. Heating conditions were identical to those used in the unconfined core experiments described above, with a maximum temperature of 600^{o}C and a maximum heating rate of 10K/min. A nitrogen flow rate of 6 scfh was used in this reactor, matching the free stream velocity used in the smaller tube furnace.

Supporting Equipment

Scanning electron microscopy (SEM). SEM imaging was performed on many coal samples to understand the evolution of macroporosity in large coal samples during pyrolysis. An FEI NanoNova field-emission gun SEM was utilized for this purpose. This particular SEM was advantageous for coal analysis because it had a low-vacuum detection mode that permitted imaging under up to 1 torr of water pressure. The purpose of the water was to dissipate charge accumulation on nonconducting samples. This allowed coal to be imaged without the need for any conductive coating. Generally, good structure resolution was seen between 100nm and 100μm. This covered the range of macroporous structure in the observed coal samples.

BET surface analyzer. The purpose of the BET surface analyzer was to measure the surface area and pore size distributions of the pyrolyzed coal samples. The instrument used was a Micromeritics Tristar II surface analyzer. Low-pressure isotherms were measured on degassed coal chars using carbon dioxide at 0^{o}C as a noncondensing

adsorbate. CO_2 was chosen after N_2 at 78K was shown to give erroneous isotherms (likely due to volumetric swelling effects). Isotherms were collected over a P/P_o range of 0.01 to 1. The BET surface area was extrapolated via regression of the first five points of low-pressure data. The complete isotherm was used to calculate the full pore size distribution via the BJH analysis method. These analyses were conducted automatically by the supporting software provided by Micromeritics.

Thermogravimetric analysis (TGA). TGA was used to compare the char yields and pyrolysis kinetics of very small coal particles at very slow heating rates. The purpose was to understand the pyrolysis behavior at the opposite extreme of particle size from the cores being used in the tube furnace reactor. The TGA instrument was a Q600 from TA Instruments. It was capable of performing steady temperature ramps at rates up to 20K/min to temperatures of 1000^{o}C. In the performed experiments, it was operated at 0.1 and 10K/min up to 600^{o}C, then held for 24hrs. The sample size was approximately 13mg of coal dust (< 38μm). Samples were held under a steady 50mL/min flow of nitrogen. This was found to be the slowest flow rate that would exclude oxygen and prevent fluidization of coal particles. Sample weight, temperature and derivative data were recorded every 30s for the duration of the experiment.

Experimental Methodology

The purpose of this section is to provide enough detail on experimental methodology to allow other users to replicate the described experiments. The intent is not to provide a step-by-step procedure for each type of experiment, but rather to explain and justify the methods used such that the methodology can be adapted to varying equipment,

acknowledging that each device carries with it operational vagaries that necessitate adaptation of procedure to develop the same effect.

Coal Block Preparation

Blocks of bituminous coal were prepared for use in the block pyrolysis reactor. Each block was selected to ensure a minimum of obvious large cleats. Blocks were cut with a handheld concrete saw to create flat faces perpendicular to the bedding planes. The purpose of the flat faces was to create a smooth surface for drilling heater and thermocouple holes. The blocks were faced perpendicular to the bedding planes because it was anticipated that heaters in a UCTT process would be oriented parallel to the bedding plane. Facing the blocks perpendicular to the bedding planes meant that heater holes would orient approximately parallel to them. It was necessary to choose blocks such that the two cut faces were 5” apart. Once cut, the flat surface needed to be at least 6” by 6” to ensure sufficient mechanical integrity to withstand drilling. Blocks typically ranged from 3 to 5kg after cuts were made.

After cutting faces, a drilling pattern was placed on one face. Heater and thermocouple locations were marked from the pattern with dots of yellow paint. The block was secured on a drill press table to ensure stability during drilling. Heater holes were drilled to 3.25” depth using masonry drill bits. These bits were found to be ideal for bituminous coal as they did not frictionally dissipate large amounts of heat while drilling. SEM analysis of coal samples adjacent to the heater holes show that only mild oxidation occurred during drilling. Thermocouple holes were drilled to 1.5” depth using a 3/32” metal-cutting bit. Great care had to be taken with these bits as they tended to overheat, causing tensile failure of the metal or induction of coal pyrolysis, causing the drill bit to

become stuck when tars condensed. It was determined through trial and error that the hole needed to be drilled in small increments to prevent the bit from overheating, each incremental bit of drilling required careful realignment of the bit and hole to ensure the bit was not strained and the drill needed to run until the bit had been completely backed out of the hole to prevent it from locking up. Water or other lubricants were not used to avoid affecting the coal composition.

Coal Core Preparation

Cores of bituminous coal were prepared for use in the tube furnace and confinement vessel reactors. Cores were prepared from larger blocks of coal using a diamond-grit hole saw. They were drilled perpendicular to the bedding plane of the coal block, usually because the block could be most stably secured to the drill press when laid flat on one of the planes.

Cores were drilled using a 7/8” diamond-grit hole saw. This particular drill bit was ideal because it did not cause much heating to the core surface, as determined by SEM analysis. The inner diameter of the hole saw was slightly smaller than the listed size, producing cores of approximately 2cm in diameter. Cores were prepared on a drill press with the block secured to ensure it did not move during drilling. Cores were drilled incrementally, with drilling interrupted at intervals to clean away dust and debris. The drill bit was kept rotating until the bit was clear of the coal surface to ensure it did not become stuck to the core. Drilling was continued until a core had exceeded the depth of the hole saw or a natural cleat had been reached, causing the core to break off on its own. If the core did not detach on its own, a screwdriver was used to pry the core off the block. All cores above 9g were accepted for experimentation; smaller cores were discarded. The

maximum possible core size was just under 15g. Water or other lubricants were not used to avoid affecting the coal composition.

Block Pyrolysis and Sampling

Coal blocks were heated in the block pyrolysis reactor. Experiments were conducted at two heating rates (0.1 and 10K/min) to a maximum heater temperature of 500^{o}C. This temperature was chosen to maximize the heater lifetime. The cartridge heaters were determined to have a roughly Gaussian temperature profile with a peak temperature in the center of the cartridge that was approximately 150K hotter than the ends when they were operated between 400 and 600^{o}C. Thus, when the terminal-grounded heater thermocouple read 350^{o}C, the heater was assumed to have a maximum temperature of 500^{o}C. After ramping to the ultimate temperature, the heaters were held constant for either 3 or 12hrs. The heaters were controlled by the OPTO system. The associated software allowed five parameters to be specified for each experiment: the target temperature, the number of steps to achieve the target temperature, the time length of the heating ramp, the time length of the hold at the target temperature and the length of the cooling ramp. 50 steps were used when ramping at 10K/min and 200 steps were used to ramp at 0.1K/min. Regardless of heating rate, the block was cooled at 10K/min. Blocks were heated under a slow flow of 3 scfh of nitrogen. The reactor was prefilled with nitrogen before pyrolysis to ensure oxygen was excluded.

After pyrolysis, the block was allowed to fully cool under a nitrogen atmosphere. Once cool, the outer portions of the block were cut away with a table saw or concrete saw. What remained was the 1.5”x1.5”x5” region between the four heater holes. If fracturing made the block appear mechanically unstable, some epoxy was used to prevent

disintegration. Once the central column of the block was isolated, it was then cross-sectioned at approximately 1.5" from the top surface of the block, corresponding to the region of maximum heater temperature. Two small samples were removed from the cross-section: one adjacent to the heater hole and one adjacent to the central thermocouple hole. These pieces were then subjected to three 1hr washings via sonication in warm xylenes to remove any coal dust or mobile tars at the surface. Washed samples were dried at 100^{o}C for 3hrs before SEM analysis was performed. These samples were retained for SEM analysis to analyze the difference in porosity development between the hottest region near the heaters and the cooler region of the block in the center.

Core Pyrolysis and Sampling

Coal cores were pyrolyzed in three different types of experiments: complete pyrolysis, char and tar yield profiles and confinement experiments. The details of each type of experiment vary; however, all experiments utilized two uniform heating rates, 0.1 and 10K/min, and three ultimate temperatures, 350, 450 and 600^{o}C. These temperatures were considered representative of the likely pyrolysis temperatures in a UCTT scenario. The heating rates were chosen in an attempt to distinguish rate effects within the realm of experimental feasibility (a ramp to 600^{o}C at 0.1K/min requires nearly 4 days to achieve the peak temperature).

The purpose of complete pyrolysis experiments was to measure the final char yield as a function of temperature and heating rate, and to determine the complete pore size distribution when the devolatilization process had ended. Core samples were heated at a linear rate to the ultimate target temperature, and then held at that temperature for 24hrs under a 0.5 scfh laminar flow of nitrogen. Following pyrolysis, samples were

cooled back to room temperature at 10K/min. Each set of six experimental conditions was tested on three different coal samples to assess the variability of the data collected. Core samples were weighed immediately before and after pyrolysis to determine the char yield at complete pyrolysis. Additional core samples from all three blocks were heated to 120^{o}C for 36hrs under a nitrogen sweep to determine the moisture content of each coal. Elemental analyses of the three coal samples are given in Table 3-1.

Char and tar yield profiles were collected to determine how temperature and heating rate affect the global kinetics of the devolatilization process in large coal particles. The pyrolysis procedure was performed analogously to the complete pyrolysis experiments, with one modification. At certain precise temperatures during the heating ramp, the quartz tube was removed from the furnace and the coal sample was dropped into a cooled, capped jar to quench the reaction and then obtain a precise measurement of the char yield at that temperature. The glass wool plug was removed from the quartz tube and placed in a beaker. The condensed tar on the surface of the quartz tube was then gently heated with a heat gun, and then washed into the beaker with acetone. The beaker was dried in an oven at 70^{o}C. The weight of collected tar was measured by difference. Char and tar yields were measured along the full heating ramp as well as the temperature hold until pyrolysis was complete. For example, for a target temperature of 450^{o}C, measurements were taken at 100, 200, 300, 350, 400 and 450^{o}C, as well as after 1 and 3hrs of pyrolysis at the maximum temperature. Devolatilization was found to be nearly complete after 3hrs for the 450 and 600^{o}C cases, regardless of heating rate. Due to the extensive amount of data collected in this experimental campaign, only one coal block

was used. However, certain pieces of data were repeated three times to get a measurement of variability.

The purpose of the confinement experiments was to test the effect of volumetric constraints on pyrolysis. These experiments were performed in the larger tube furnace apparatus using the aluminum confinement vessel. The experimental parameters were identical to the complete pyrolysis experiments. After pyrolysis, samples were cooled back to room temperature at 10K/min. Core samples were then carefully removed from the aluminum vessel for weight measurement. The same coal block used for the char and tar yield profiles was also used for this experimental campaign.

After pyrolysis, all samples from the complete pyrolysis and confinement experiments were prepared for SEM analysis. Cores were cross-sectioned near the center of the core. A piece was removed that contained both the curved outer edge of the core and material from near the center of the core. These pieces were then subjected to three 1hr washings via sonication in warm xylenes to remove any coal dust or mobile tars at the surface. Washed samples were dried at 100^{o}C for 3hrs before SEM analysis was performed. SEM analysis was used to perform pore size analysis on the cores as a function of temperature and heating rate.

Residual char from all three types of experiments were prepared for surface analysis. Char was pulverized and sieved to capture the fractions between 104 and 150μm. Any particles larger than 150μm were ground in a mortar and pestle and resieved. The captured fraction of particles was degassed in a vacuum oven at 80^{o}C for at least seven days to prepare for surface analysis.

SEM Imaging and Analysis

SEM images were collected on the FEG-SEM described above. Imaging was performed in low-vacuum mode under 0.30 torr of water pressure. The acceleration voltage on the gun was set to 5keV. This value was chosen to trade some resolution for greater topographic detail of sample surface. This tradeoff was found to give better detail on the morphological changes in the coal structure. Imaging was performed in a regimented fashion to ensure that user bias did not skew the results. The surface was initially focused at 800x magnification at a particular spot on the sample surface. After saving the first micrograph, four more images were saved at uniform intervals along a diagonal pattern. After collecting the first five images, the SEM was refocused to 5000x magnification and imaging was repeated along a perpendicular diagonal until ten micrographs had been collected to fully sample the region being examined. For block experiments, each piece yielded fifteen total micrographs. For the core pyrolysis samples, each sample yielded fifteen images at the particle edge and fifteen at the particle center for a total of thirty micrographs per sample.

SEM micrographs were analyzed to derive pore size distributions. Each image was analyzed manually due to the difficulty of programming a computer to recognize pores amongst other structures on the sample surface. Pores were counted on each collected micrograph, and each pore was measured by its maximum length and average width. From these data, average pore areas were calculated by an elliptical area approximation. Pores were grouped together on a logarithmic scale ($>0.001\mu m^2$, $>0.01\mu m^2$, etc.). The data set was aggregated for each experimental condition. To create pore size distributions, data from the five 800x micrographs needed to be scaled to the

data from the 5000x micrographs. To do so, the 0.01μm^2 pore size was chosen as a basis for comparison. For each experimental condition, the total pore counts in each size group for the 5000x micrographs were rescaled to make the 0.01μm^2 pore count equal that of the same group in the 800x micrographs. Once the datasets from the 800x and 5000x micrographs were merged, pore area size distributions were calculated and reported as probabilities by number fraction for each size group. This process was repeated for all examined experimental conditions.

BET Surface Analysis

The Tristar II surface analyzer was used to perform surface area measurements and full pore size distributions on powdered samples from all core pyrolysis experiments. The standard particle size used for analysis was 104 to 150μm. All samples were thoroughly degassed for at least one week in a vacuum oven at 80^oC to ensure that any residual volatiles were removed. Low-pressure adsorption isotherms were measured using CO_2 at 0^oC as a noncondensing adsorbate. Adsorption isotherms were measured over a P/P_o range of 0.01 to 1, with a 10-point desorption isotherm measured to look for hysteresis effects. Adsorption data were automatically analyzed by Micromeritics software to calculate BET surface area and the pore size distribution via the BJH method.

All char samples were subsequently checked for the presence of residual tars and oils that might alter the surface properties of the coal. After the initial surface analysis was performed on each sample, they were treated by Dean-Stark extraction in warm acetone for 2hrs. The char samples were then washed twice with warm acetone and again dried for at least one week at 80^oC. Isotherms were again collected in identical fashion and the same analyses were performed on the data.

TGA Analysis

TGA data were collected on finely ground coal samples to compare the pyrolysis kinetics at very small particle sizes where mass transfer resistances were not expected to be important. Samples of 38μm coal powder were prepared by grinding coal with a mortar and pestle. 13mg samples of powder were run in the TGA under a 50 mL/min flow of nitrogen. The instrument was ramped at either 0.1 or 10K/min to ultimate temperatures of either 350 or 600^{o}C. The pyrolysis was continued for 24hrs at the maximum temperature, with data collection occurring every 30s. The instrument recorded sample temperature, sample weight and the weight change derivative at each time interval.

CHAPTER IV

EXPERIMENTAL HEAT TRANSFER ANALYSIS

The purpose of this chapter is to analyze the heat transfer conditions of various experimental setups and determine what effect they have upon the actual heating rate of the coal samples utilized in the described research. This chapter is not intended to provide precise calculations of heat transfer in each experimental configuration. Rather, it is intended to provide comparisons of the relative impact of competing heat transfer mechanisms (conduction, convection and radiation) upon the actual heating rate of coal samples. Consequently, simplifying assumptions are frequently employed to make the analyses presented more computationally tractable.

This chapter will first present an analysis of block coal heating including modeling of the cartridge heaters based upon experimental measurements of the heater's temperature profile. It will also describe three different experimental setups performed in the tube furnace apparatus and the impact of convective heating on those cases. From the presented analyses, it will be argued that heat transfer is not a limitation at the slowest heating rate (0.1K/min) and that the coal particles exist in a pseudosteady-state with the reactor temperature.

Coal Block Heating Experiments

The purpose of the presented coal block heating model is to estimate the temperature profile and heating rates inside of a block that resembles those used in block heating experiments. By comparing experimental temperature data with model estimates, the physical processes that affect heat transfer and the resulting impact upon experimental conditions can be determined.

The block heating experiments, described in Chapter 3, utilize four cartridge heaters arranged in a square pattern to dissipate heat into the mass of coal. The heating rate is controlled by PID response to thermocouples embedded within the heaters. Additionally, three thermocouples are placed at known positions within the coal block to gain point measurements of the temperature profile in the block during transient heating. Consequently, enough is known about the temperatures and localized heating rates away from the heater surfaces to compare them to the transient heating model developed here.

The presented transient block heating model is based upon a finite difference method calculation. Several assumptions are made to reduce the complexity of the model, including:

- coal thermal properties that vary with temperature but do not account for changes caused by pyrolytic decomposition
- strictly radiative heat transfer at the interface between the heaters and the block, but no convective losses from the heater holes
- strictly conductive heat transfer within the coal domain
- convective and radiative heat transfer on open faces of the block, with the heat transfer coefficient determined by horizontal or vertical orientation

- zero-flux boundary condition (no heat transfer) on the bottom face of the block due to insulation on the reactor floor
- symmetrical block shape, allowing the amount of calculations to be cut in half
- latent heating of coal moisture up to its boiling point, plus heat of evaporation, but no further heating of moisture once it has been vaporized

The impact of these assumptions is not easy to assess given the physical situation of heating bituminous coal. For example, the coal's thermal properties are likely to change as it decomposes into char, but it is difficult to find a mathematical description of these changes. Likewise, heat is likely lost by convective outflow from the heater holes; however, swelling during pyrolysis may well seal off the heater holes, greatly reducing this effect. Measuring the existence and magnitude of this is difficult, but it is not expected to greatly impact the presented calculations.

The following sections present the mathematical development of the block heating model, including the modeling of the cartridge heaters, and present a comparison of model and experimental results.

Finite Difference Model of Block Heating

This section describes the mathematical framework of coal block heating model. A transient, two-dimensional finite difference approach was employed to approximate the heat transfer dynamics in the block. The 2-D coal block was assumed to be 6"x6" with 2 heater holes of ¼" width and 3" depth at the top face of the block. The heater holes were 2" apart, centered about the vertical midline of the block. The block was partitioned into uniform nodes of 1/8"x1/8".

Node temperatures were computed by calculating heat flux balances. Internal nodes were assumed to be only affected by conductive heating from the four cells that shared faces with the node being examined. Surface nodes and internal nodes adjacent to the heaters were subject to conductive as well as radiative and convective fluxes, depending upon the situation. Figure 4.1a shows a schematic of the heat flux balance for an internal node, while Figure 4.1b shows the flux balance for an external corner node. Because of the positioning of the external surface node at the very corner, only a fraction of the specified node face length was available for heat transfer. For simplicity, temperature gradients were assumed to be negligible in the third spatial dimension so that heat fluxes in this dimension could be ignored. This assumption weakens near the block corner where the block depth is small due to the diagonal profile through the block, but given the small temperature gradients in this region of the block, the introduced error is considered low.

Due to the differing heat transfer processes affecting different areas of the coal block, it was necessary to compose unique heat flux balances for each area. In total, there were ten unique balances derived for this model. Although this chapter will not list each of these balances, the MATLAB code used to calculate the entire model is listed in Appendix A. Each heat flux balance began with the same general equation (1) describing the transient energy accumulation in the node's control volume.

$$\rho C_p V_{node} \frac{\Delta T}{\Delta t} = \sum q_{cond} A_{cond} + \sum q_{conv} A_{conv} + \sum q_{rad} A_{rad} \quad (1)$$

For internal nodes, convection and radiation were ignored, reducing the right side of equation 1 to just the conductive term. Nodes adjacent to the heaters were assumed to

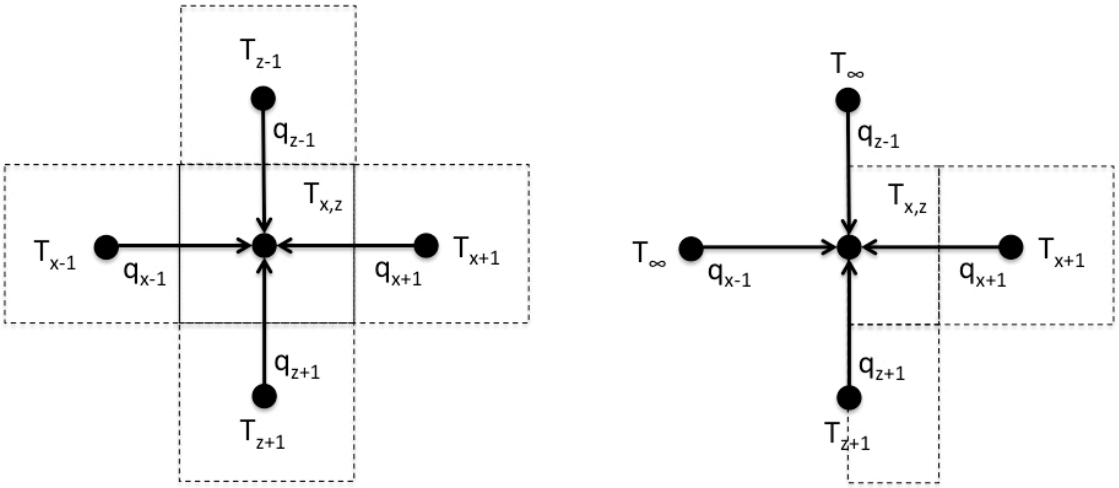

Figure 4. 1 Schematic of finite difference nodes for coal block heating at A) a fully internal node and B) an external corner node

have conductive and radiative fluxes, but no convection. External nodes (along block edges and faces) were assumed to have convective and conductive fluxes, but no radiative exchange with the surroundings. Conduction was assumed to be described by Fourier's Law while convection and radiation were described by the standard linear and quartic relationships, respectively. The discretized forms of the heat transfer relationships could be substituted into equation 1 and simplified for each of the ten unique regions of the block. For example, the internal node shown in Figure 4.1a was modeled by equation 2.

$$T_{n,t+1} = Fo\left(T_{n,z+1} + T_{n,z-1} + T_{n,x+1} + T_{n,x-1}\right) + (1 - 4Fo)T_{n,t} \quad (2)$$

The Fourier number, Fo, is defined as:

$$Fo = \frac{k\Delta t}{\rho C_p \Delta x^2} \quad (3)$$

By contrast, the balance for the external corner node shown in Figure 4.1b was modeled by equation 4.

$$T_{n,t+1} = 4Fo\left(T_{n,z+1} + T_{n,z+1}\right) + (1 - 4Fo)T_{n,t} + \frac{2\Delta t}{\rho C_p \Delta x}(h_v + h_h)(T_{n,t} - T_\infty) \quad (4)$$

A convective flux boundary condition was used at the top and side faces of the block, assuming a constant surrounding gas temperature of 25^{o}C. The bottom face was insulated, so a zero-flux boundary condition was used. The block was isothermal at 20^{o}C at the initial time. The thermophysical properties used for the bituminous coal are listed

in Table 4.1. Correlations for vertical (equation 5) and horizontal (equation 6) heat transfer coefficients were used [Incropera, 1996].

$$Nu_{horiz} = 0.15Ra^{1/3} \tag{5}$$

$$Nu_{vert} = 0.68 + \frac{0.670Ra^{1/4}}{(1+(0.492/Pr)^{9/16})^{4/9}} \tag{6}$$

These correlations required calculation of the Rayleigh number, which is defined as:

$$Ra = \frac{g\beta(T_{n,t}-T_{\infty})L^3}{\eta\propto} \tag{7}$$

Thermophysical parameters for nitrogen, the convective medium, are listed in Table 4.2. Radiative heat transfer was calculated assuming an emissivity for bituminous coal of 0.9.

The time step for each iteration of calculations was 1s for both the 10K/min and 0.1K/min heating cases. The temperature profile was calculated for up to 12hrs in the fast ramp case and 72hrs in the slow ramp case. The model of the temperature profile of the cartridge heaters used in the larger coal block model stems from an experimental analysis of the heater temperature profile and efficiency. This analysis is discussed in the following section.

Cartridge Heater Modeling

Due to their nonisothermal temperature profiles, shown in Figure 4.2, it was necessary to determine an approximate model for the heaters that could be employed in the block heating model. Experimental measurements of the heaters demonstrated the roughly Gaussian temperature distribution, with a maximum temperature very near the center of the heater body. It was also determined experimentally by calorimetry that the

Table 4. 1 Thermophysical properties for a bituminous coal [Howard, 1981]

Property	Value	Units
Density	1545	kg m^{-3}
Heat Capacity	500.06+0.829T	kJ kg^{-1} K^{-1}
Thermal Conductivity	$(0.495+3.966(273.15/T)^{-1/2})^{-1}$	W m^{-1} K^{-1}

Table 4. 2 Thermophysical properties of nitrogen [Incropera, 1996]

Property	Value	Units
Dynamic Viscosity	$26.4x10^{-6}$	m^2/s
Thermal Diffusivity	$38.3x10^{-6}$	m^2/s
Prandtl Number	0.69	
Thermal Conductivity	$33.8x10^{-3}$	W m^{-1} K^{-1}

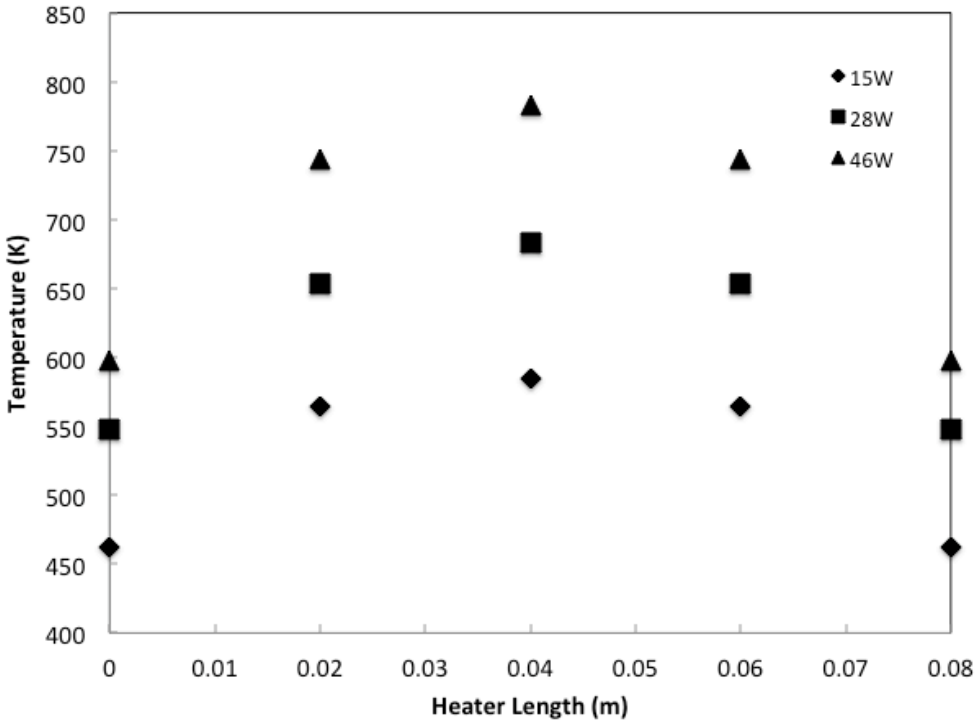

Figure 4. 2 Temperature profiles for cartridge heaters at specified power outputs

heater rating (in Watts) was accurate, meaning that the heater very efficiently dissipated heat. Consequently, the heater was modeled with the constraints that its temperature profile was Gaussian and its total power emission was the integral sum of the radiative power at each point on the heater surface. Mathematically, these constraints could be expressed as:

$$Q = \int qdA = \int_0^L \varepsilon\sigma(T(x)^4 - T_\infty{}^4)2\pi R dx \tag{8}$$

$$T(x) = T_{end} + Be\text{^}(-\gamma\ \llbracket(x - D\ /\ 2)\rrbracket\text{^}2\ ) \tag{9}$$

T_∞ was assumed to be 25°C, matching the temperature of the lab where measurements were performed. Because the heaters were controlled by a thermocouple grounded to the end of the heater, the set temperature was always the minimum heater temperature. As a result, equation 9 was written to ensure that the end temperature always matched the setpoint temperature and the maximum temperature at the center of heater body was determined by the constraint of equation 8.

To complete the heater model, it was necessary to find parameters for equation 9 that matched the measured experimental data. Good fit to the data was found at B=150 and γ =0.1. Figure 4.3 shows a comparison of this model to the experimental data. There is some deviation between actual and predicted temperatures, especially at the heater ends; however, this is not expected to be a problem because radiative heat transfer is less sensitive at lower temperatures. For the purposes of the coal block heating model, the cartridge heater model presented here is considered sufficient.

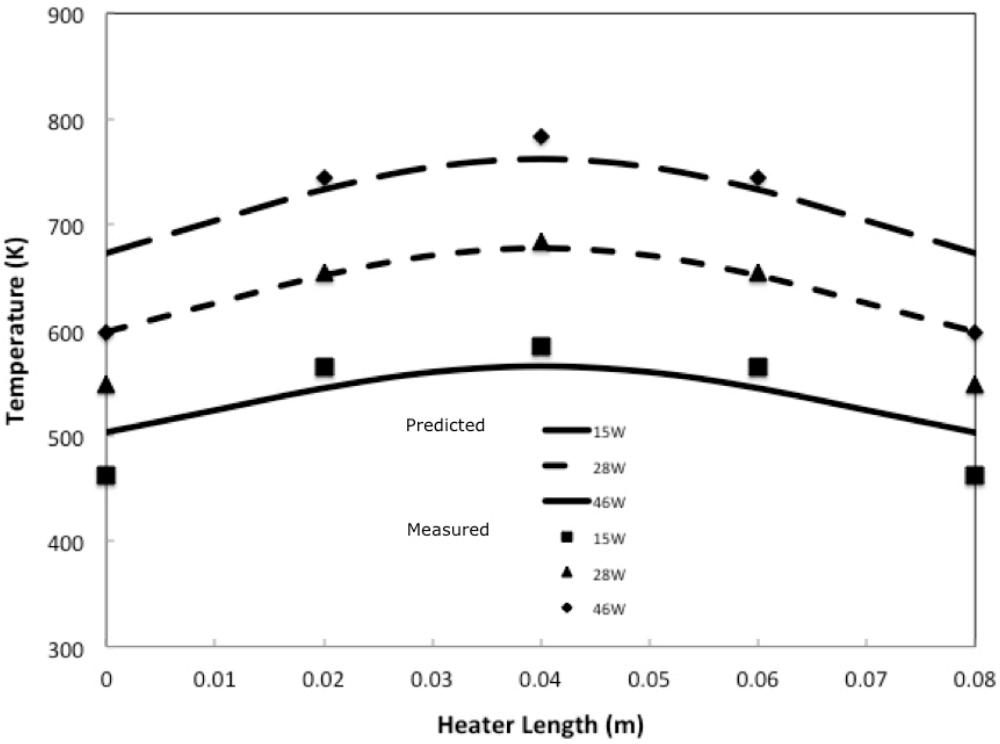

Figure 4. 3 Model predictions and measured values for cartridge heater temperature profiles

Coal Block Heating Results

The block heating model showed a substantial difference in heating behavior for the slow and fast heating cases, although both cases eventually converged upon the same temperature profiles. The temperature at the center of the block between the four heaters was predicted to converge to a value of around 380^{o}C for a 500^{o}C maximum heater setting. At a 10K/min heating rate, heat transfer into the coal block was limited, resulting in temperature hysteresis. The model shows peak temperatures being achieved nearly 3hrs after the heater has reached its maximum temperature. In contrast, the block center temperature follows the heater temperature fairly consistently in the 0.1K/min case. Figure 4.4 shows model-predicted temperatures at the block center for both cases, along with actual experimental measurements for both cases. The x-axis uses a normalized time in which the time to achieve the maximum heater temperature has a unit of 1, and each subsequent hour of pyrolysis at maximum heater temperature also has a unit of 1. This time normalization allows 10K/min experiments (~1hr heating time) and 0.1K/min experiments (~3 day heating time) to be directly compared. The experimental results are in qualitative agreement with the modeling results, although temperatures were not found to exceed 290^{o}C during experiments, likely due to heat losses not accounted for in the modeling assumptions.

The qualitative agreement between modeling and experiment bolster the idea that heat transfer is limiting when the heating rate is at least 10K/min. Several factors may explain why the experimentally measured temperatures fall short of the model predictions. First, thermocouple positioning is subject to error in a region where a fairly steep temperature gradient exists due to the Gaussian temperature profile of the heater.

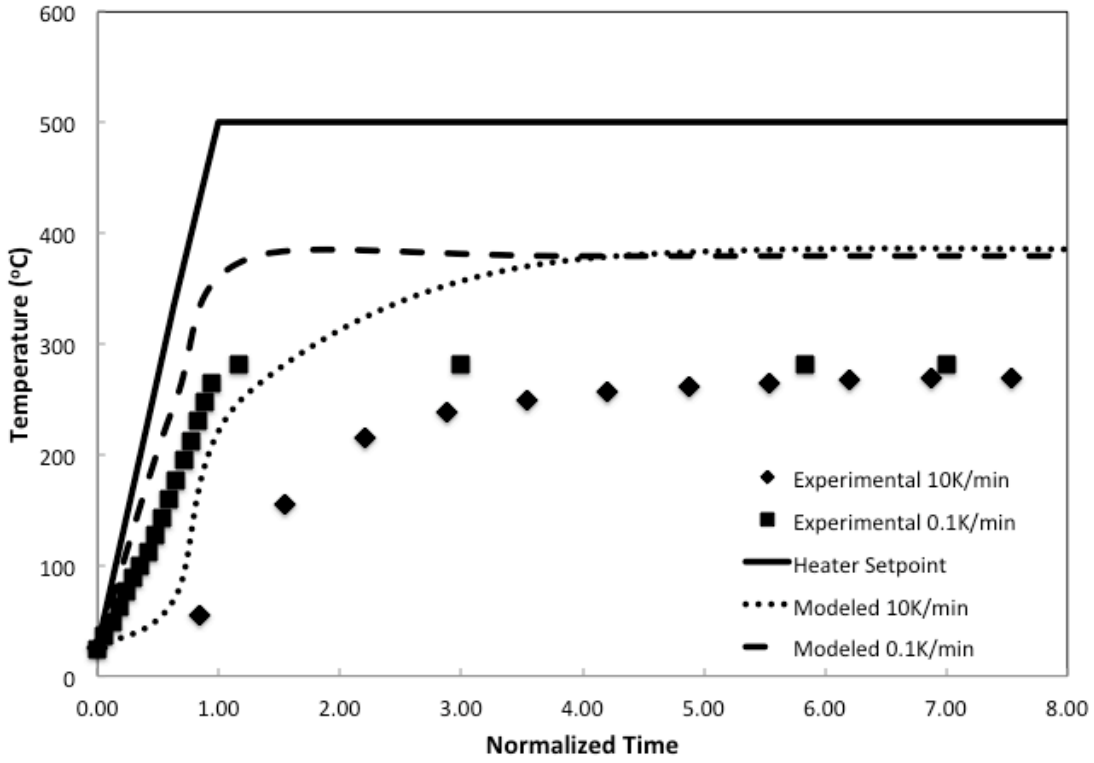

Figure 4. 4 Model predictions and experimental observations of block center temperature for slow and fast heating rates.

Additionally, heater position can vary, compounding the measurement error. Also, the model does not attempt to account for heat losses in the heater bore holes. Although the holes are only slightly larger than the heater diameters, space does still exist for convective heat dissipation. The thermal diffusivity of the coal may also decrease in response to pyrolysis, diminishing the rate of radiative heat transfer and increasing convective losses in turn. Lastly, the model does not account for a reaction endotherm or latent heating of liquid and gas products. Given the hindered release of pyrolysis products and the large volume of coal, these effects may cause a significant consumption of energy.

Tube Furnace Experiments

The tube furnace experiments comprise a series of experiments that were performed in a clamshell-style furnace. Coal particle geometries in this experimental setup varied from cores to packed gravel beds to powder in a ceramic boat. Consequently, each type of experiment had unique heat transfer considerations. The purpose of this section is to analyze the heat transfer conditions in each of these experimental setups and determine what impact they would have on the observed coal pyrolysis. It is important to analyze the magnitude of these impacts to ensure that observations of pyrolysis made at varying particle sizes are directly comparable. The analysis of coal core heating is accomplished through a transient conduction model that is similar to the block heating model described above. The analyses for gravel and powdered coal particles are accomplished via “back-of-the-envelope” calculations that reveal the magnitude of competing heat transfer processes during pyrolysis.

Core Heating Model

The development of the core heating model is analogous to the development of block heating presented earlier in this chapter. The major difference is that the heat flux to the coal core passes from the quartz tube to the core's external surface, rather than an embedded internal heater. Thus, the boundary conditions for the core particle differ from the coal block. The core's cylindrical geometry also necessitates a switch from Cartesian to cylindrical coordinates.

In this model, the core is supposed to be 2" long and 1" in diameter. Heat is presumed to enter the core strictly through radiative heat transfer over the entire surface of the core. Because the core is short compared to the heated length of the furnace, the heat source is considered to radiate at a uniform temperature that matches the setpoint of the furnace. Experimental characterization of the utilized tube furnace found this assumption to be valid as the heater element tended to radiate above the setpoint but the inner surface of the quartz tube closely matched the setpoint. There is also assumed to be a small convective loss caused by laminar flow of nitrogen over the core surface. By symmetry, the model reduces to a two-dimensional model that varies with length and radial distance from core center. There is a no flux boundary condition at the core center.

Cores are divided into nodes with equal radial spacing. Figure 4.5 shows a diagram of a conceptual internal node with conductive fluxes depicted. As a result of the cylindrical geometry, the areas for radial conductive heat flux vary for each node. As a result, the flux balances for each node become more complicated than the ones derived for a Cartesian system. For example, the heat flux balance for a fully internal node leads to the following expression for the node temperature at a fresh time iteration:

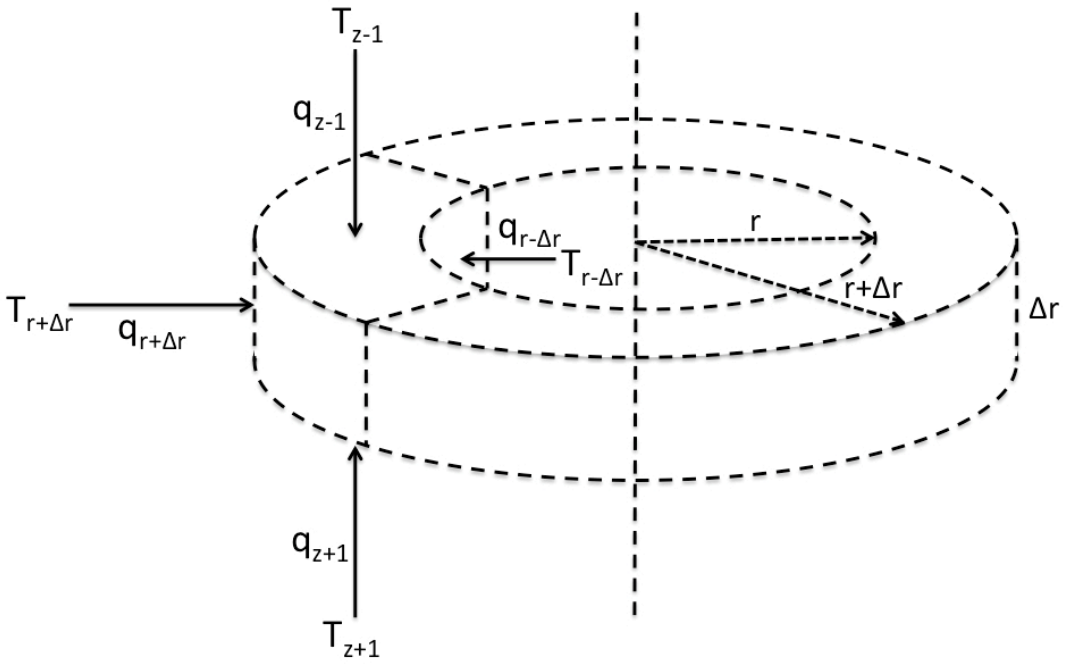

Figure 4. 5 Schematic of finite difference node for a cylindrical coal core

$$T_{n,t+1} = \frac{2\propto\Delta t}{2(r+\Delta r)\Delta r+\Delta r^2}\left(T_{n,r-1} - T_{n,t}\right) + \frac{2(r+\Delta r)\propto\Delta t}{(2(r+\Delta r)\Delta r+\Delta r^2)\Delta r}\left(T_{n,r+1} - T_{n,t}\right) + \frac{\propto\Delta t}{\Delta r^2}\left(T_{n,z+1} + T_{n,z-1} - 2T_{n,t}\right) + T_{n,t} \quad (10)$$

A full listing of the MATLAB code used to solve for the temperature profile in the coal core geometry is listed in Appendix A. The model was iterated at 1s time steps for both 10K/min and 0.1K/min heating rates. The thermophysical properties for coal and the surrounding nitrogen environment were the same as those listed in Table 4.2.

Coal Core Modeling Results

The core heating model shows distinct differences between the slow and fast heating rates. The results show a heat transfer limitation in particles of this size at a 10K/min heating rate, but no such limitation at 0.1K/min. Figure 4.6 shows a plot of the temperature profiles for the furnace, the core surface and the core center at the faster heating rate. It is apparent that there is a significant lag in heating at the particle center.

Figure 4.7 shows a plot of the temperature difference between the core surface and center for both heating rates. The plot is normalized to compress the heating ramp for the 0.1K/min case into the same space as the fast heating case, but the subsequent soak time at the maximum temperature is identical for both cases. From the figure, it can be noted that there is a small and constant temperature gradient in the coal core when heated slowly, while the fast heated core develops a large temperature lag that does not fully correct until after the furnace has been at its setpoint temperature for over 4hrs.

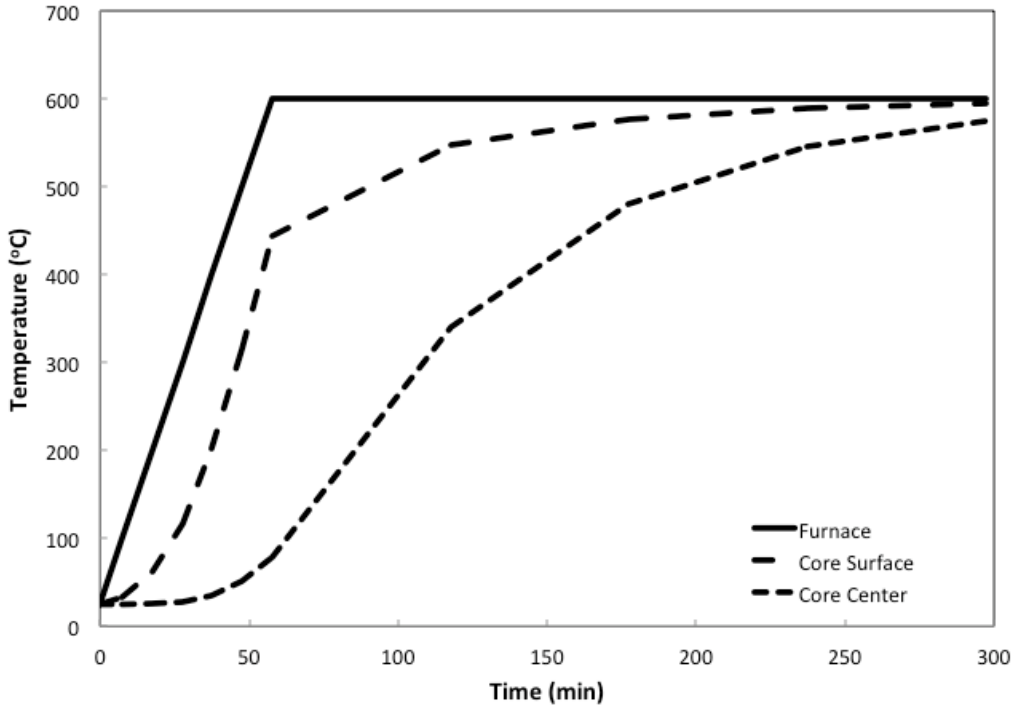

Figure 4. 6 Conduction model predictions for core heating at 10K/min heating rate

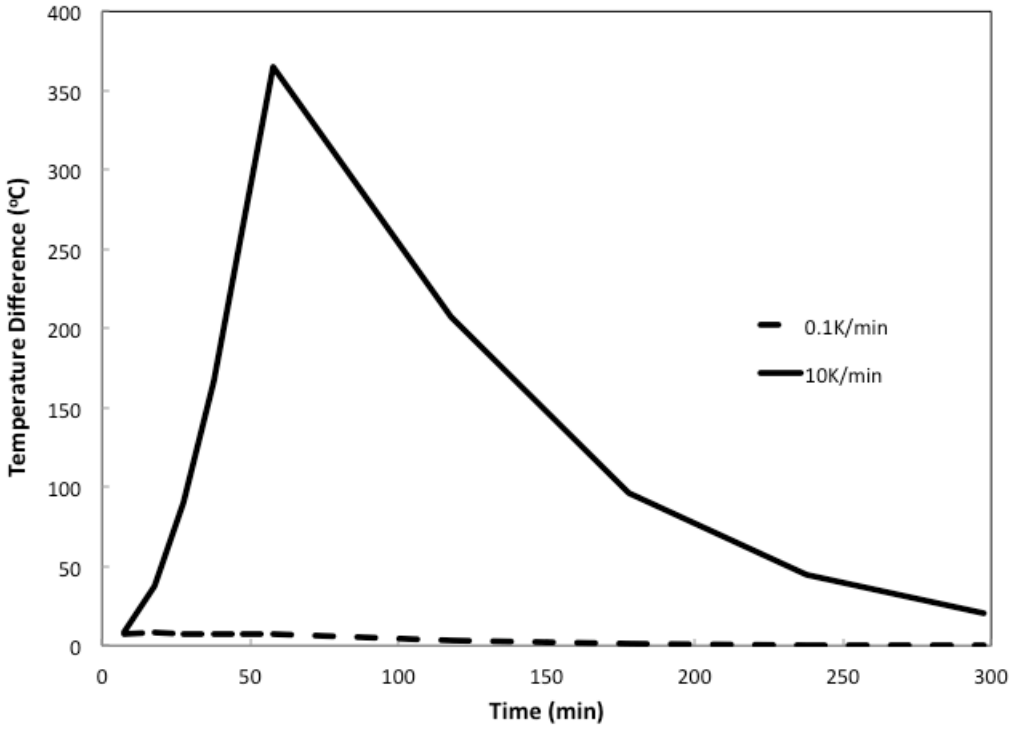

Figure 4. 7 Predicted temperature differences between core surface and center for slow and fast heating cases

The core heating model results show that conductive heat flow is limited at as low as a 10K/min heating rate. This result is important to the interpretation of core experimental results because it suggests that pyrolysis proceeds through the core in a wave with the surface region of the core achieving rapid devolatilization long before pyrolysis has even begun in the core center. The result also shows that the effective heating rate in the core center is around 3K/min, so porosity observations made at the core centers for slow and fast heating are actually separated by a smaller range than the furnace ramp rate would suggest.

The core heating model has several simplifications that must be remembered when interpreting the results. No account is made for the change in thermal properties caused by pyrolysis. Swelling, compositional changes and mass loss may all affect the thermal conductivity and heat capacity of the coal structure, leading to unknown changes in the rate of heat transfer. The model also likely oversimplifies the rates of radiative and convective heat transfer at the core surface, although the magnitude of impact is uncertain. So, the presented model is taken as a qualitative argument that a coal particle of about 1" diameter will have heat transfer limitations when heated at 10K/min or higher.

Gravel and Powder Heat Transfer

In the experimental scenarios in which gravel beds or powder beds are heated in the tube furnace, different heat transfer mechanisms must be weighed to decide which processes dominate. The most striking change as the particle size decreases from the 1" core to the 75μm powder is the decrease in conduction path length and the rapid increase in surface area.

To assess the effect that particle size has upon conduction time, a simple scaling analogy can be composed. Assuming conduction to be the dominant heat transfer mechanism within the coal particle, a simple partial differential equation to capture the transient temperature change can be composed:

$$\rho C_p \frac{\partial T}{\partial t} = k \frac{\partial^2 T}{\partial x^2} \tag{11}$$

When this equation is nondimensionalized, a very simple relationship for the characteristic time scale for conduction is found:

$$t_c = \frac{R^2}{\propto} \tag{12}$$

So, assuming that the thermal diffusivity of coal is not affected by particle size, it can be seen that the characteristic timescale for heat conduction is proportional to the square of the particle's approximate radius. Table 4.3 compares the characteristic conduction times for the three considered particle sizes when the largest conduction time is scaled to 1. By this analysis, the coal core that required 3hrs to become isothermal at 600^{o}C at a 10K/min heating rate would only require 0.1s as a 75μm particle.

The rapid conclusion is that conductive heat transfer is far less of a limitation to the actual particle heating rate at the smaller particle sizes. In this case, the greatly enhanced surface areas of smaller particles would aid both radiative heat transfer and convective dissipation. The balance between these two processes once again comes back to the experimental geometry.

In the packed gravel bed experiments, the 3mm coal particles are filled into a cylindrical bed inside the quartz tube. In this configuration, the coal is arranged similarly

Table 4. 3 Characteristic conduction times for coal particles

Particle Size	t_c
2 cm	1 minute
3 mm	1.4 seconds
75 µm	0.8 milliseconds

to a coal core, but with substantial void fraction to allow gas flow through the bed. The large total surface area and relatively minor heat conduction limitation is presumed to allow efficient radiative heat transfer between particles such that the temperature gradient between particles near the furnace wall and those near the center is smaller than the gradient through a coal core.

Aside from the more rapid response to the applied temperature ramp, convection is also expected to play a larger role in this system. Based upon the measured bed lengths for known amounts coal, the void fraction of the packed beds for the 3mm particles was found to be about 0.5. For a constant nitrogen volumetric flow rate of 0.75 scfh, the average gas velocity in the void spaces is 3cm/s. At this flow rate, the correlation of Sherwood *et al*. predicts the heat transfer coefficient in a packed bed to be ~17.6W/m^{2}K. In the limiting case of slow heating, the particle temperatures can be assumed to be in an isothermal pseudo-steady state, in which case the actual particle temperature can be estimated by a surface balance between radiative heating and convective cooling.

$$\varepsilon\sigma A_{part}\left(T_f{}^4 - T_s{}^4\right) = h_{pb}A_{part}(T_s - T_g) \tag{13}$$

When solving equation 13, the nitrogen purge was assumed to heat moderately prior to contacting the coal bed due to its short residence time in the furnace and its laminar flow, which does not encourage heat transfer to the gas. Assuming the N_2 stream to be near

200^{o}C, equation 13 could be solved for any furnace temperature. Figure 4.8 shows a plot of predicted particle temperatures as a function of furnace temperature. The departure from the furnace temperature in the pyrolysis zone is estimated to be around 25-40^{o}C. This estimate is confirmed by experimental data. Figure 4.9 shows a plot of mass loss from 1" coal cores and 3mm particles as a function of temperature at a heating rate of 0.1K/min. The figure shows that when the coal temperature is assumed to be the furnace temperature, the curves are offset, but when the 3mm particle temperatures are adjusted to account for convective losses, the mass loss curves are quite similar. The data suggest that heat transfer conditions in the two experiments account for the discrepancy between the measured mass losses.

The 75μm coal powder experiments present a slightly different scenario due to their arrangement in a ceramic boat. A stable bed could not be maintained in the cylindrical configuration of the core and gravel experiments because the small particles tended to fluidize, even at a laminar flow rate of nitrogen. Consequently, the particles were placed in a flat-bottomed ceramic boat that permitted nitrogen flow only over the open space above the boat. The particles showed no signs of fluidization in this configuration. It can again be qualitatively argued that the high surface area of the very small particles enabled very rapid response to radiative heat transfer from the furnace. However, in this situation, only the top-most layer of particles was prone to convective losses and direct radiative heating, accounting for a small fraction of the total surface area. Although natural convective cooling is possible in the void space between the particles, it is likely that gas outflow from the coal particles once devolatilization commences does not allow for much inflow of cooler gases into the void space of the

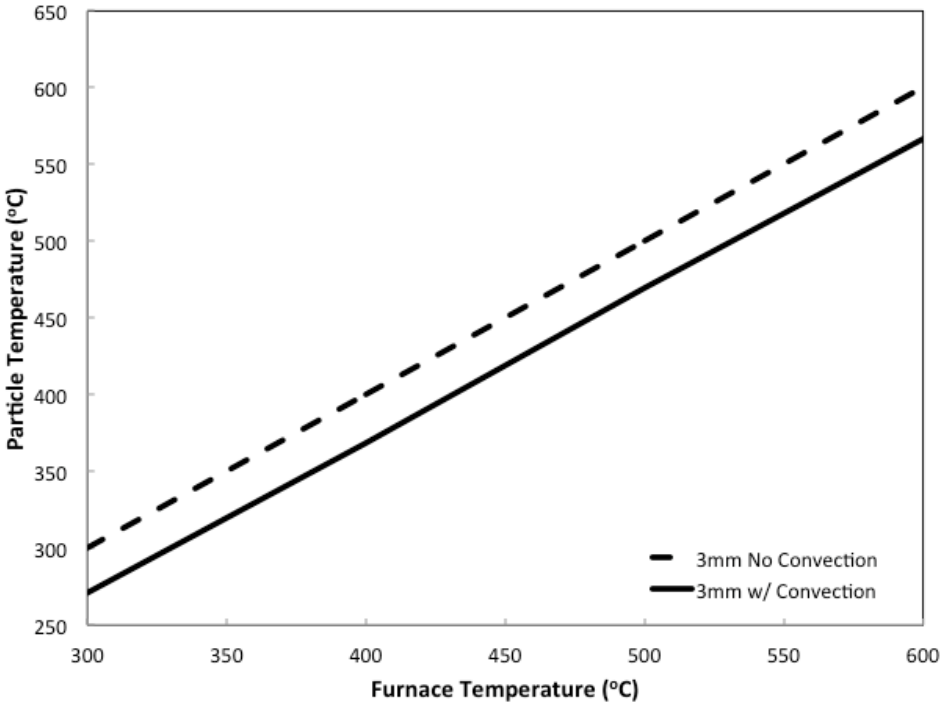

Figure 4. 8 Prediction of temperature for 3mm coal particles with and without convective cooling

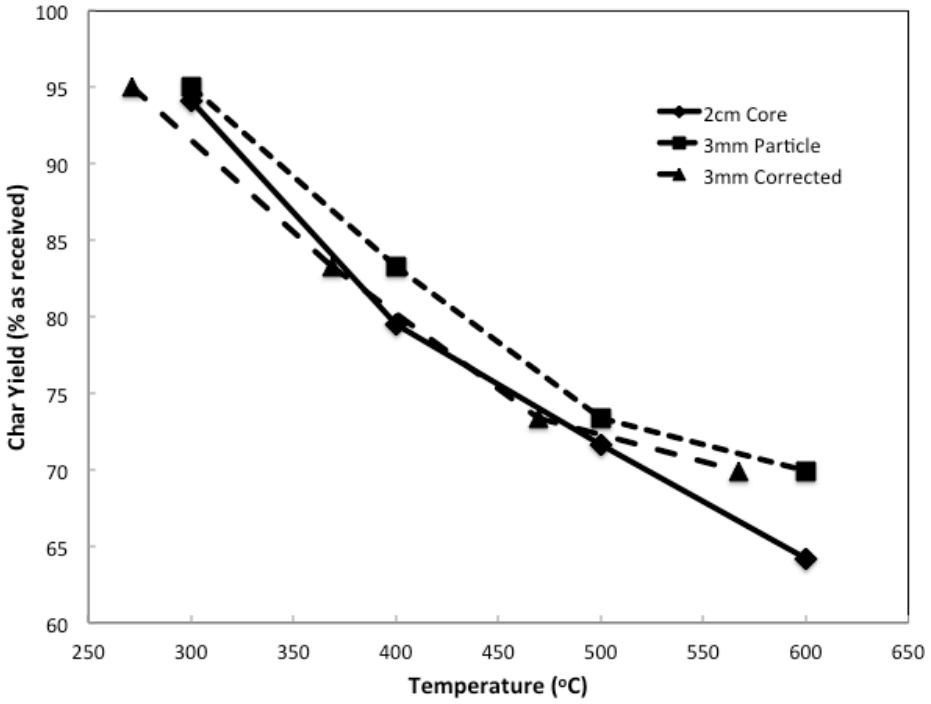

Figure 4. 9 Comparison of char yields for 2cm and 3mm coal particles including correction for convective cooling

bed, effectively stopping convective cooling. For this reason, a qualitative expectation is that the powder particles will respond similarly to the coal cores during heating. Mass loss data support this assumption.

Heat Transfer During Confinement Experiments

Core confinement experiments are not expected to have a large effect on the heat transfer characteristics of the coal core. The confinement vessel is made of aluminum and has a much higher thermal conductivity than the coal cores. The primary limitation to heat transfer is the lower emissivity of aluminum. Although the vessel is oxidized and roughened, it is still only likely to have an emissivity of around 0.2. This will diminish the rate of radiative heat transfer to the vessel from the ashing furnace used for these experiments.

Numerical modeling of the confined core experiment is more difficult than the other detailed simulations due to the range of response rates in aluminum radiation, aluminum conduction and coal conduction. Numerical instabilities tend to develop at the surface nodes very early in the simulation run. The instabilities could be eliminated by changing the time step and node size; however, these adjustments rapidly became intractable from the perspective of computational time, especially for slow-heating cases that required up to 3 days worth of heating to be simulated. Consequently, models have not been developed for the confined vessel experiments. However, it can be argued that an emissivity change from 0.9 to 0.2 reduces the radiative heat flux by approximately 80%, thus decreasing the heating rate by a similar amount. In this situation, wall-to-coal conduction may be the dominant form of heat transfer. Due to heating rate limitations in the furnace used for these experiments, it was considered sufficient to allow the furnace

to heat at its maximum rate to achieve the best possible heating rate inside the confinement vessel. At 0.1K/min, the rate of heat transfer to the vessel is not expected to be a problem.

Conclusions

The purpose of this chapter was to describe how heat transfer affected the pyrolysis conditions in the various experimental setups utilized in the described research. Pyrolysis was explored in coal particles ranging in size from fine dust to large blocks, each necessitating a slightly different heating method. Each experimental setup was differentiated according to the particle bed geometry and heat transfer method.

Transient heating in large coal blocks was shown to qualitatively differ between the cases of 0.1K/min and 10K/min heating rate. The coal in the slower heating rate model responded proportionately to the heater response while the coal had heat transfer limitations at the faster heating rate that slowed the effective heating rate at the block center. The modeling results agreed qualitatively with experimental results, although the actual block temperatures were found to be lower than the model predicted. The cause of the difference is uncertain although direct convective losses from the heaters is likely to limit the total power dissipated into the coal block.

Pyrolysis conditions in particles heated in the tube furnace were also differentiated by heat transfer conditions. A scaling analysis showed that the conduction time in a micron-scale powder was five orders of magnitude faster than for a 1” coal core. Consequently, it was shown that heat transfer limitations increased substantially with particle size at a 10K/min heating rate. At a 0.1K/min heating rate, all samples are believed to have small thermal gradients as steady state is approached and can be

approximated as isothermal during experiments. It was also demonstrated that the geometry used to heat 3mm gravel particles increased convective losses. A convection analysis gave a temperature decrease of 25 to 40K due to convection in that configuration, which agreed well with experimental results.

In general, it can be concluded that heat transfer is limited at a 10K/min heating rate but not at 0.1K/min for all coal domain sizes analyzed in this research. The experimental data support the notion that conduction no longer limits heat transfer below the 10K/min threshold, although the absolute temperature achieved becomes limited by the heater efficiency. In the following chapters, it will be demonstrated that not only heat transfer is affected by a reduction in heating rate, but the phenomenology of mass transfer as well.

CHAPTER V

POROSITY EVOLUTION IN LARGE BITUMINOUS COAL DOMAINS DURING PYROLYIS AT SLOW HEATING RATES

The purpose of this chapter is to describe the observable changes in porosity during the pyrolysis of large coal domains at very slow heating rates. First, macroporosity changes in pyrolysis are observed in 5kg coal blocks and general trends are described as a function of heating rate. Second, the observed trends from the block experiments are demonstrated in a more carefully controlled core pyrolysis reactor system, allowing for a more detailed description of porosity changes as a function of temperature and heating rate in large coal particles. Lastly, preliminary results are shown to demonstrate the effect of confinement on porosity changes in large coal particles during pyrolysis.

Results and Discussion

Block Results

5kg blocks of Utah bituminous coal were pyrolyzed via four embedded cartridge heaters at 10K/min and 0.1K/min heating rates to an ultimate maximum heater temperature of 500^{o}C. Samples were collected from each coal block in the vicinity of a heater and from near the centerpoint of the block. These samples were imaged via scanning electron microscopy to develop a qualitative understanding of the

macroporosity changes in the coal block as a function of heating rate and temperature. Image sets were subsequently analyzed to derive pore size distributions for each condition.

SEM imaging reveals substantial differences in observable macroporosity between blocks heated at 10K/min and 0.1K/min. Figure 5.1 shows typical images for an unpyrolyzed coal block at lower magnification (5.1a) and higher magnification (5.1b). Pore areas of $1.0\mu m^2$ or larger were observed infrequently; most observations of porosity were made at the higher magnification. Cleats of 1-5μm were the most common observation at low magnification. SEM images show the Utah Skyline coal used in these experiments is representative of bituminous coals with a densified, low-porosity structure.

Heating at a 10K/min rate promotes dramatic porosity changes near the interface between the coal and the heater. Figure 5.2 shows representative images at 800x magnification after 2hrs (5.2a) and 5hrs (5.2b). The coal shows an initial surge in large pores that is consistent with the plastic deformation typical of high-volatile bituminous coals. As the duration of pyrolysis increases, the near-heater pores appear to shrink, possibly due to the deposition of coked tars. Pore edges appear less sharply defined at extended times, consistent with the idea that pores have partially filled with coked tar.

Porosity changes near the block center are more difficult to assess at a 10K/min heating rate. Figure 5.3 shows representative images at lower magnification after 5hrs (5.3a) and 12hrs (5.3b). Fracturing seems to play a more dominant role than pore enlargement in this region of the block where the experimentally measured heating rate was closer to 1K/min due to heat transfer limitations. SEM imaging also shows that much

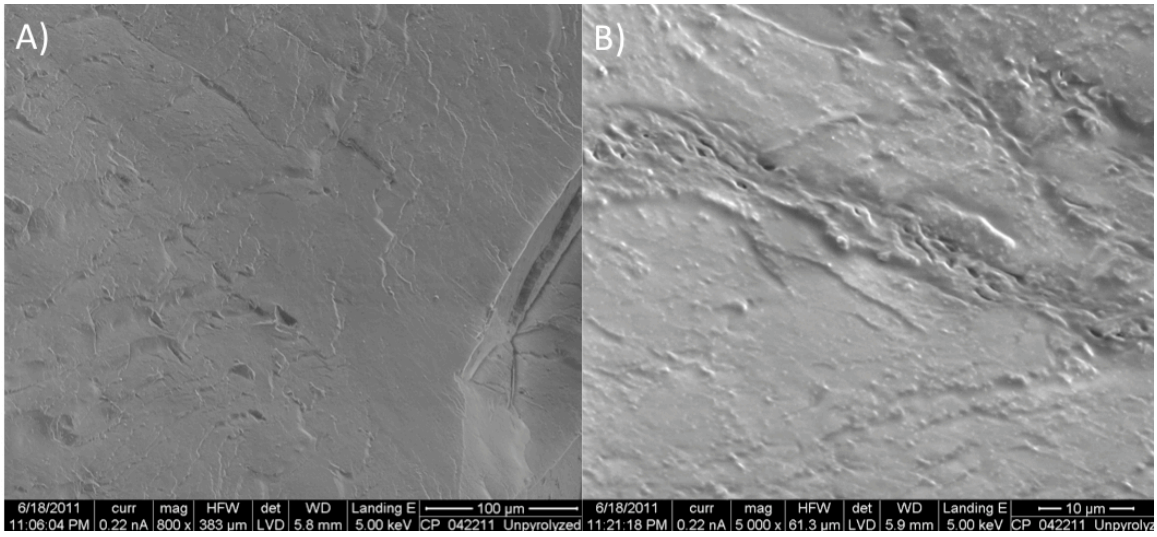

Figure 5. 1 SEM micrographs of unpyrolyzed bituminous coal at A) low magnification (100 µm scale bar) and B) high magnification (10 µm scale bar)

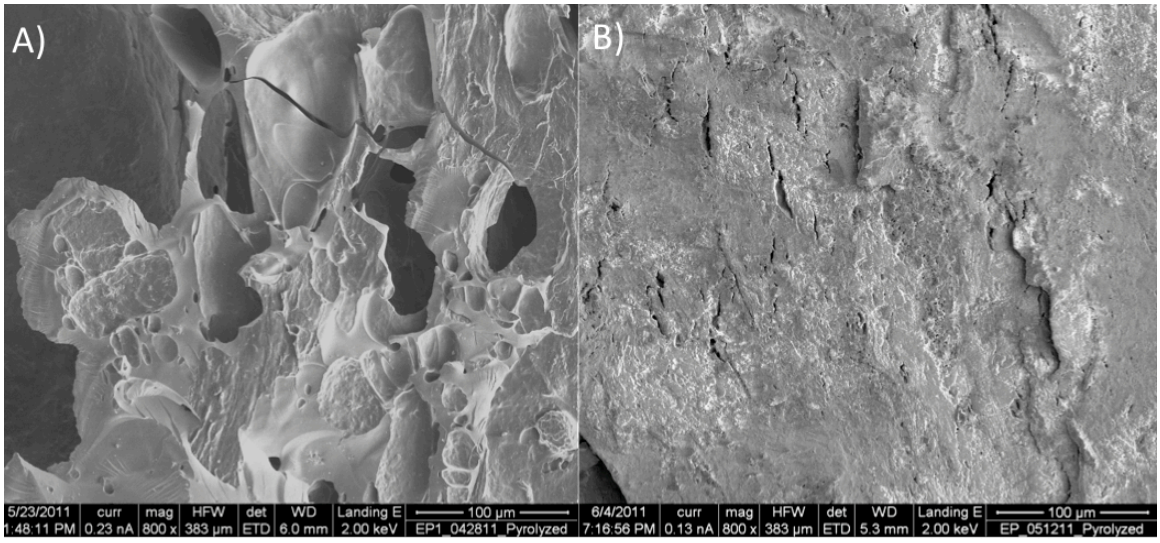

Figure 5. 2 SEM micrographs of bituminous coal adjacent to 500^{o}C heater surface after A) 2hrs and B) 5hrs of pyrolysis at 10K/min. Scale bars are 100 µm.

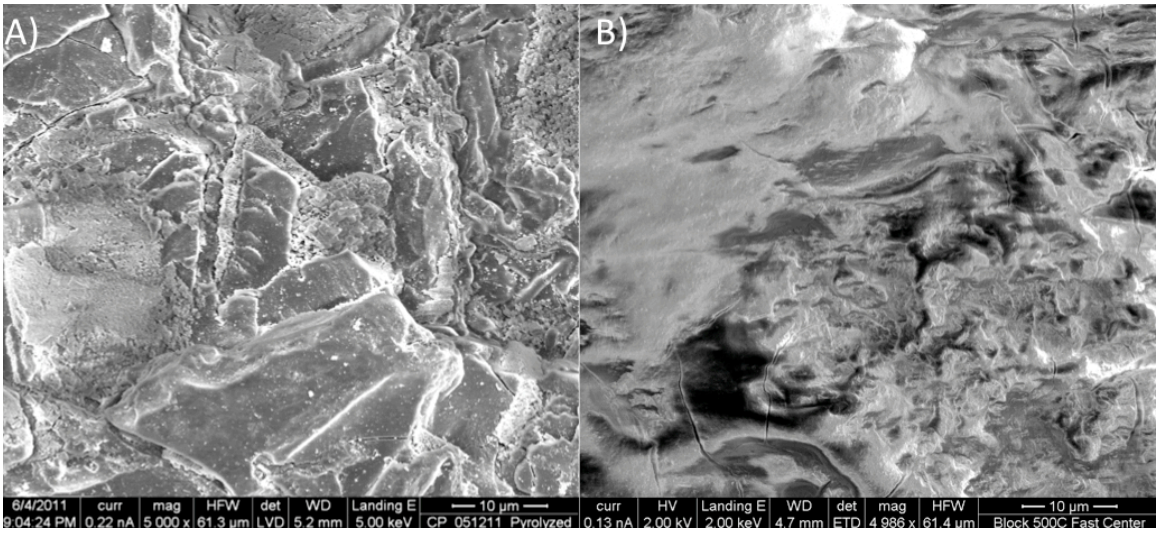

Figure 5. 3 SEM micrographs of bituminous coal near the block center after A) 5hrs and B) 12hrs of pyrolysis at 10K/min. Scale bar 10 µm.

of the available pore and fracture space is filled by tars that are not soluble when washed in xylenes at 40^{o}C. Figure 5.4 shows a close-up of a filled fracture at very high magnification. The tars appear to have receded from the walls of the fracture, possibly as the block cooled. Temperature data show that the block center has only reached the low threshold for pyrolysis by 5hrs of pyrolysis at the maximum heater temperature. Given the slow pyrolysis kinetics at around 300^{o}C, it is believed likely that the observed tars originated at higher-temperature regions of the block and were convectively transported through the network of pores and fractures to the cooler center region.

Block pyrolysis at a heating rate of 0.1K/min produces a substantially different trend than what is observed at 10K/min. SEM observations near the heat source and in the block center show little change in the porous structure of the coal. Figure 5.5 shows representative micrographs from near the block center at lower magnifcation (5.5a) and higher magnification (5.5b). There is little observable difference between nonpyrolyzed coal and pyrolyzed coal, and no noticeable change in fracturing at the slowest heating rate. Due to the frequent loss of material from friable coal blocks, mass loss from the blocks could not be measured with enough accuracy to determine if there was a significant difference in volatile yield as a function of heating rate.

SEM micrographs from each block pyrolysis experiment were analyzed to determine the pore size distribution for each case. Figure 5.6 shows the pore area probability distributions for coal near the heater surface as a function of pyrolysis time for 10K/min (5.6a-c) and 0.1K/min (5.6a,d). Figure 5.7 shows the pore area probability distributions for coal near the block center for both heating rates. In the near heater

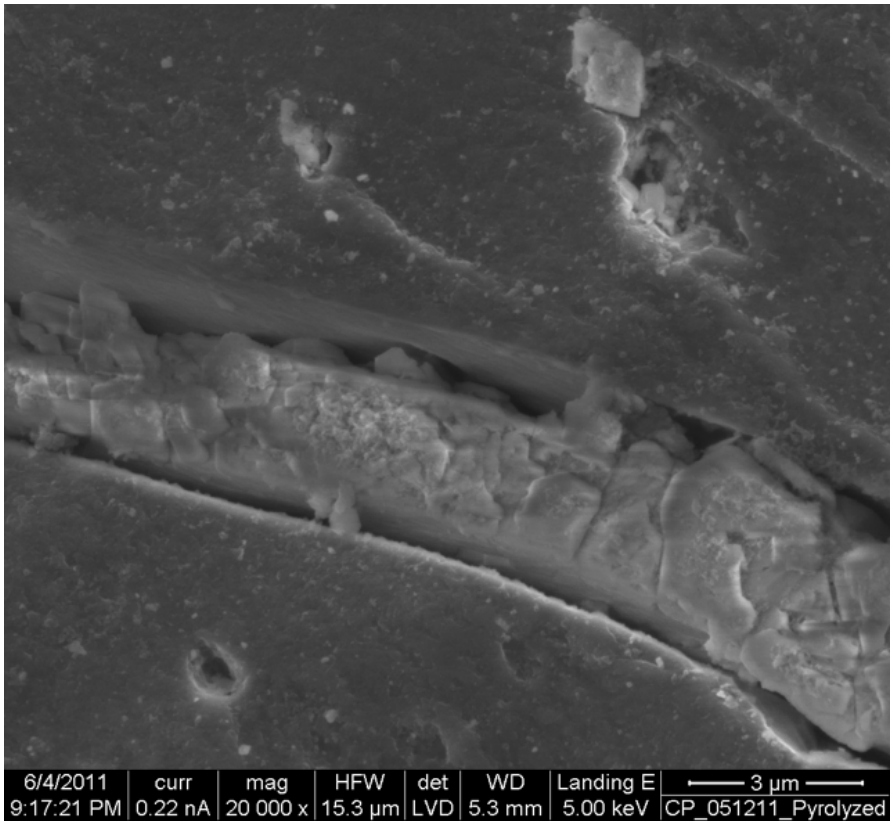

Figure 5. 4 SEM micrograph of an occluded fracture near the block center after 5hrs of pyrolysis at 10K/min. Scale bar 3 µm.

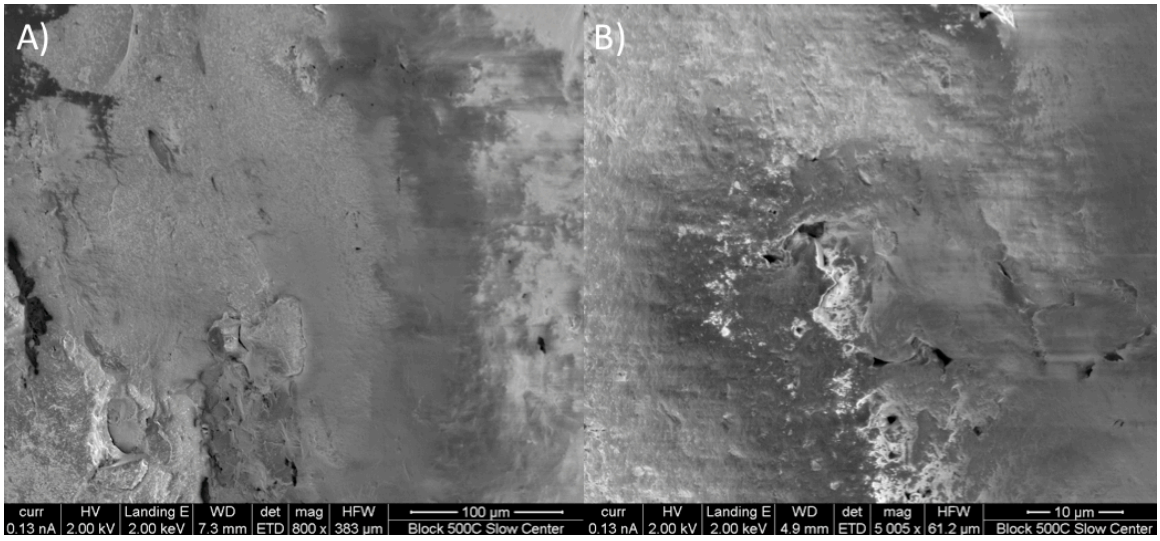

Figure 5. 5 SEM micrographs of pyrolyzed coal near the block center after 12hrs of pyrolysis at 0.1K/min. A) Low magnification (100 µm scale bar) B) High magnification (10 µm scale bar).

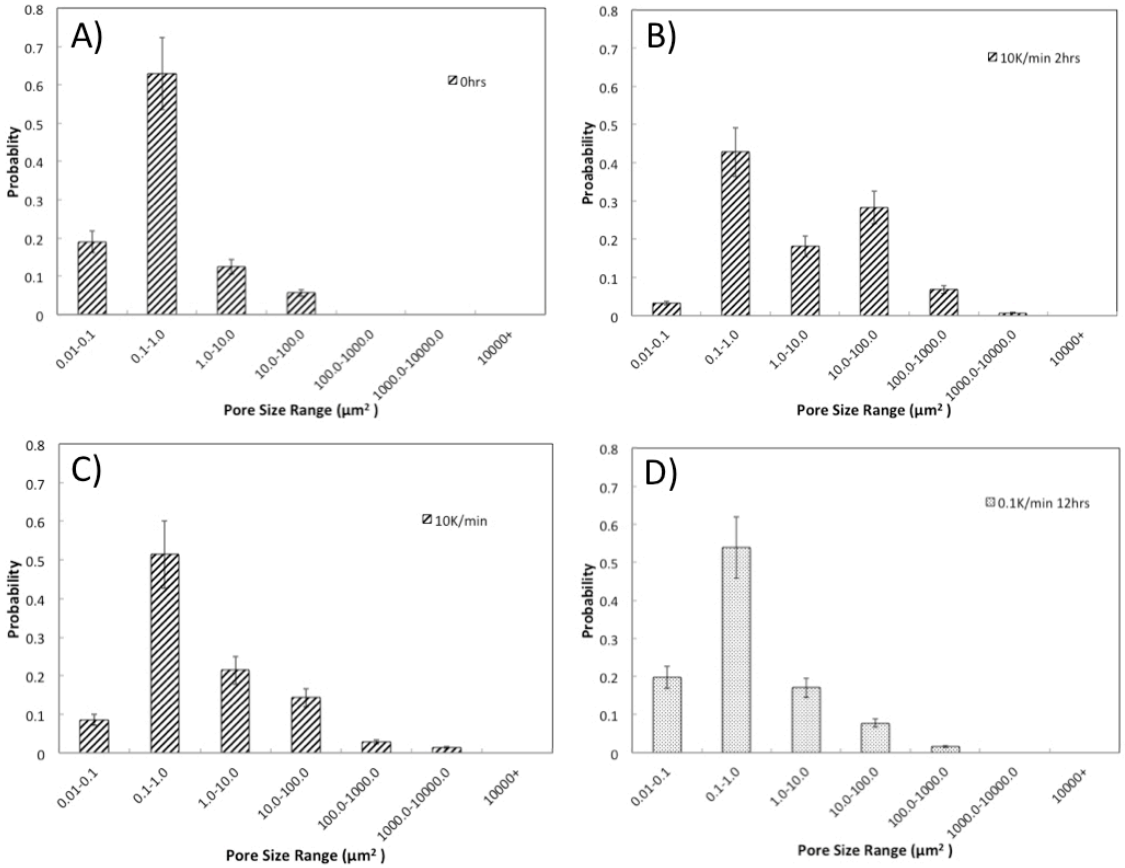

Figure 5. 6 Pore area probability distributions for coal block pyrolysis adjacent to the heater at A) 0hr pyrolysis time B) 10K/min for 2hrs C) 10K/min for 12hrs D) 0.1K/min for 12hrs

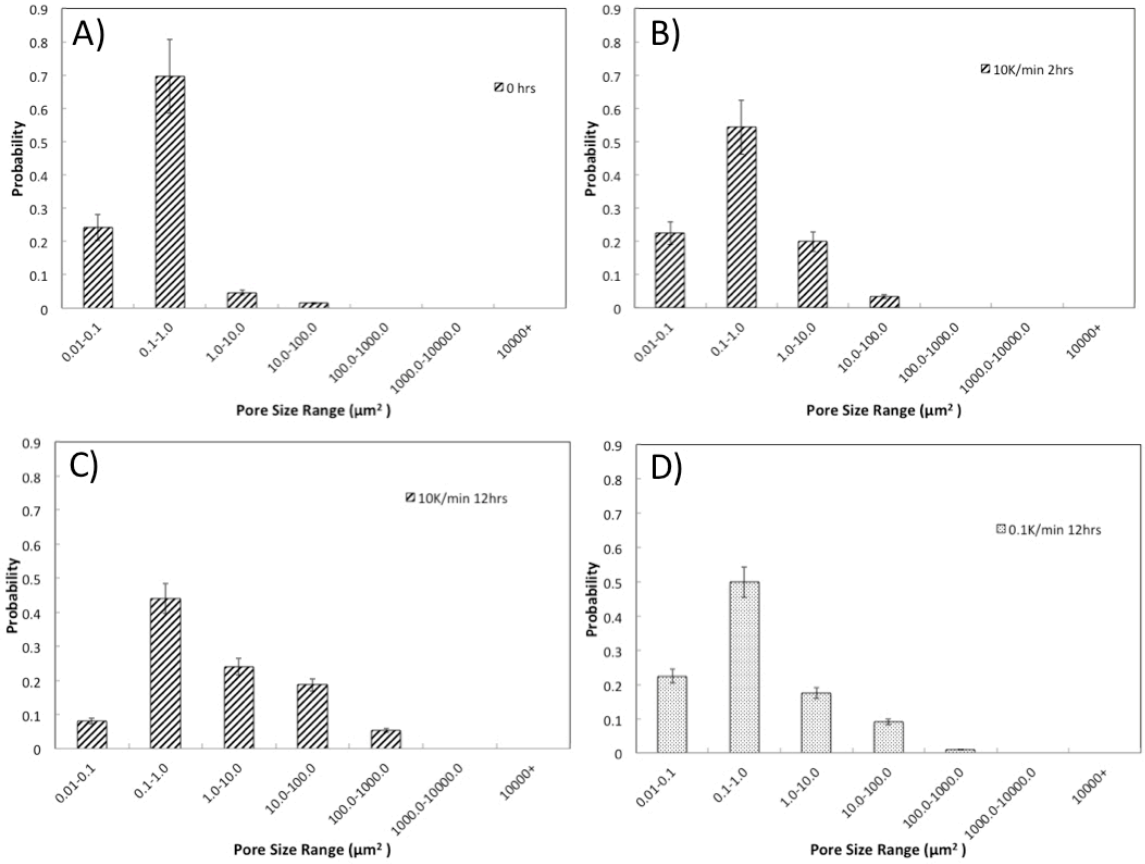

Figure 5. 7 Pore area probability distributions for coal pyrolysis near the block center at A) 0hrs B) 10K/min for 2hrs C) 10Kmin for 12hrs D) 0.1K/min for 12hrs

region, the observed plastic deformation early in the pyrolysis at 10K/min creates a bimodal pore distribution that eventually returns to a single peak as the larger pores become occluded. Pyrolysis at 0.1K/min only causes a slight broadening of the pore size distribution near the heater surface. At the block center, the pore size distribution is slightly broadened for both heating rates.

Discussion of Block Results

Results from the block experiments suggest several possible conclusions about the nature of porosity development in large coal domains during pyrolysis. First, the threshold for inducing plastic deformation in the coal occurs between a heating rate of 10K/min and 0.1K/min. This is evidenced by clear morphological changes in the char near the heater surface that are not observed at the slower heating rate. The pore size distribution shows a substantial increase in average pore size from that of unpyrolyzed coal at fast heating and high temperature but not at slow heating or lower temperature (< 350^{o}C). The absence of plastic deformation at a slower heating rate demonstrates that mass transfer from the coal block is accommodated by the existing pore system.

Second, SEM imaging shows that fracturing dominates over pore enlargement in internal regions of the coal block during rapid heating. The fracturing may be caused by the steep thermal gradient that exists between the heaters and the block core. Near the heater boreholes, the coal does have some space to expand; however, deeper in the block, any volumetric expansion caused by thermal swelling is confined by axial and radial force. In this situation, stress gradients may equilibrate by tensile failure. It is also possible that pressure-driven flow of pyrolysis products during devolatilization through the limited pore system leads to hydraulic failure as liquids condense in cooler regions of

the coal block. Neither of these two possible mechanisms can be distinguished from the available SEM data sets.

Third, rapid pyrolysis with some degree of volumetric confinement leads to a bimodal probability distribution in macropore areas. This effect, which is attributed to the inhibition of swelling, is discussed in greater detail below.

Core Results

Pyrolysis experiments using 2cm-diameter bituminous coal cores have been performed to better understand the relationship between ultimate temperature, heating rate and porosity changes. The tube furnace used to heat the coal cores makes it easier to control the heat transfer conditions via PID control and a fixed core size and geometry. The quartz tube was observed to provide some amount of radial confinement when coal swelling occurred, although cores could expand axially.

SEM micrographs of cores heated at 10K/min reveal the development of plastic deformation at temperatures above 350^{o}C. Figure 5.8 shows typical micrographs at lower magnification of coal cores heated at various temperatures for 24hrs. Little change in macroporous structure from that of uncharred coal is observed at a final temperature of 350^{o}C, but plastic deformation is evident at 450^{o}C. SEM observation at both the core surface and center show a fairly uniform distribution of porosity.

Little change in macroporous structure is seen at a 0.1K/min heating rate. Figure 5.9 shows typical micrographs at low magnification of coal cores heated at various temperatures for 24hrs. There is no evidence that plastic deformation has occurred in the

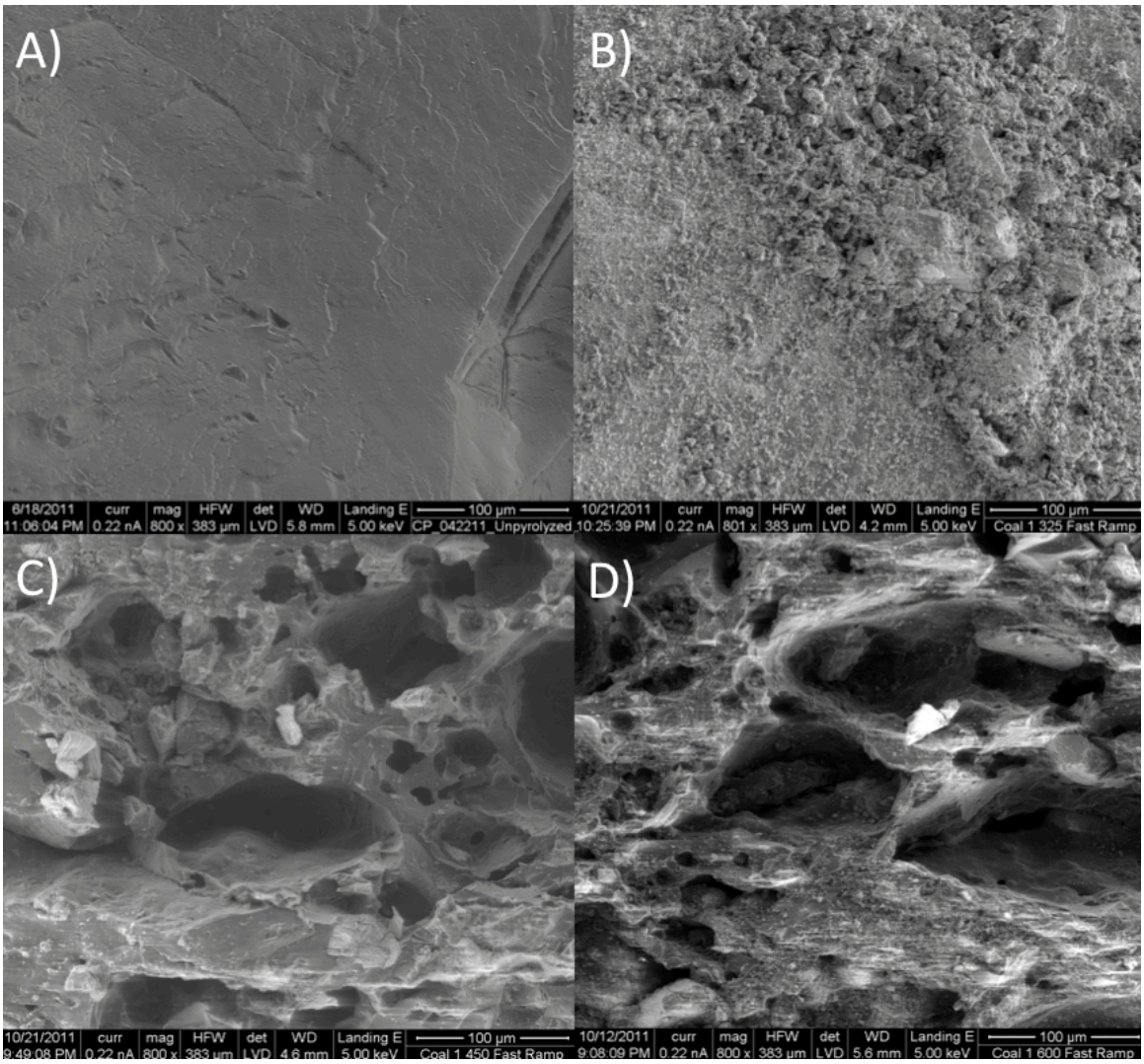

Figure 5. 8 Representative SEM micrographs for coal pyrolyzed at 10K/min heating rate (all scale bars 100 µm) A) Uncharred B) 350^{o}C C) 450^{o}C D) 600^{o}C

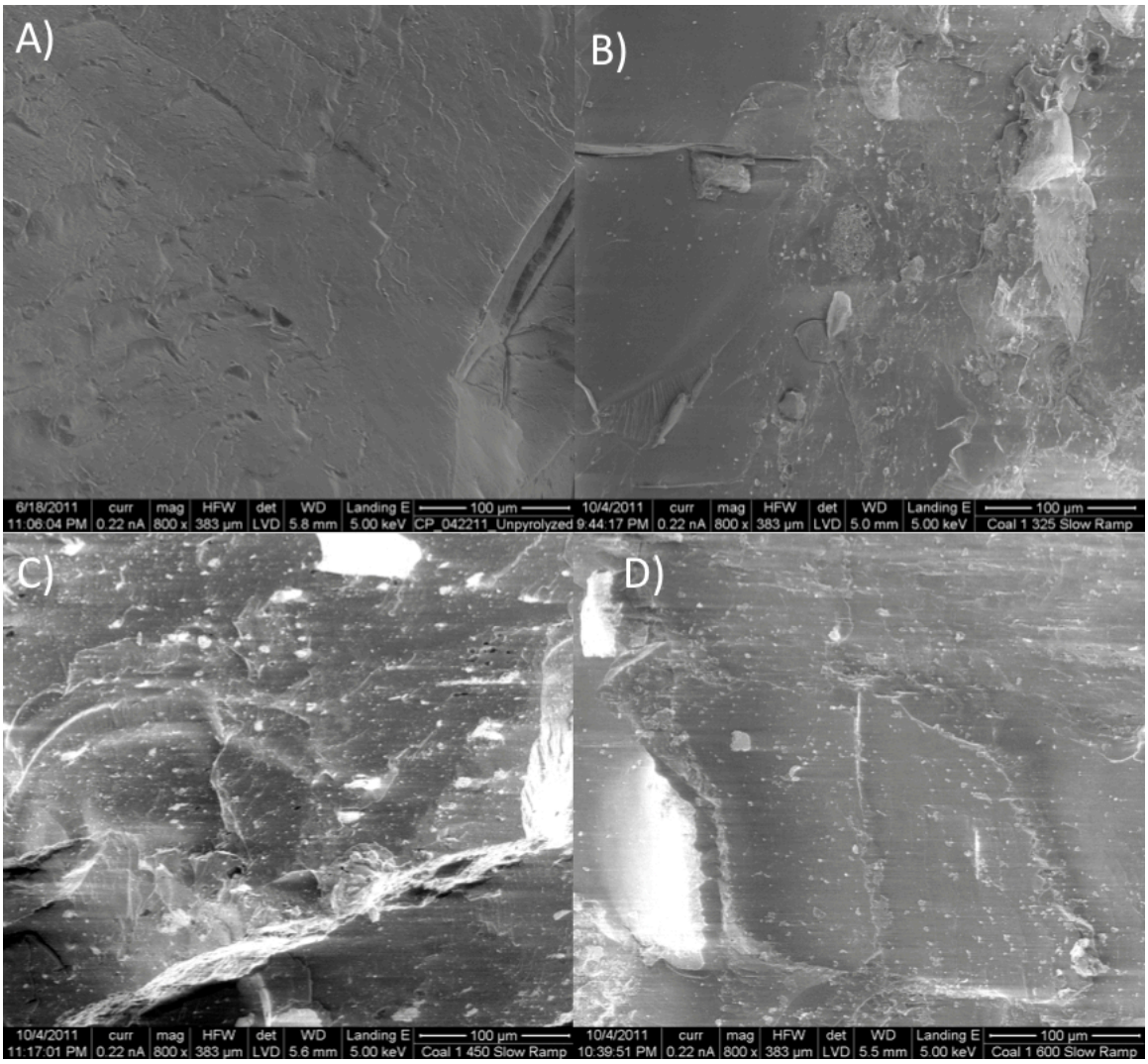

Figure 5. 9 Representative SEM micrographs for coal pyrolyzed at 0.1K/min heating rate (all scale bars 100 µm) A) Uncharred B) 350^{o}C C) 450^{o}C D) 600^{o}C

coal structure. No apparent differences are observed between the core surface and its center for any of the tested temperatures at the slower heating rate.

Pore size probability distributions derived from the SEM micrographs of pyrolyzed coal cores show the clear difference in porosity changes based upon heating rate. Figure 5.10 shows pore area probabilities for 10K/min at increasing ultimate pyrolysis temperatures. Figure 5.11 shows the probability distributions for 0.1K/min at increasing temperatures. At the faster heating rate, a clear upward shift in macropore areas is seen once the pyrolysis temperature exceeds 350^{o}C, followed by the development of a bimodal distribution at 600^{o}C, similar to that observed in block experiments. At the slower heating rate, virtually no change is seen in the macropore size distribution within the error of the experiment.

Low-pressure adsorption data reveal a more complicated relationship between heating rate and temperature upon the development of micro- and mesoporous structure in bituminous coal. All samples examined via SEM were analyzed via CO_2 adsorption after low-temperature degassing (80^{o}C) and again following a Dean-Stark extraction in refluxing acetone. BET surface area data and pore size/volume information via BJH adsorption were obtained from the measured isotherms.

BET surface area data show distinctly different trends before and after acetone extraction of the coal chars. Figure 5.12 shows surface area measurements before (5.12a) and after (5.12b) acetone extraction. The error bars represent one standard deviation based upon 3 replicate experiments. Before extraction, the chars heated at 0.1K/min show a larger internal surface area than those heated at 10K/min, especially as the pyrolysis temperature reaches 600^{o}C. After extraction, the surface areas are higher than those of

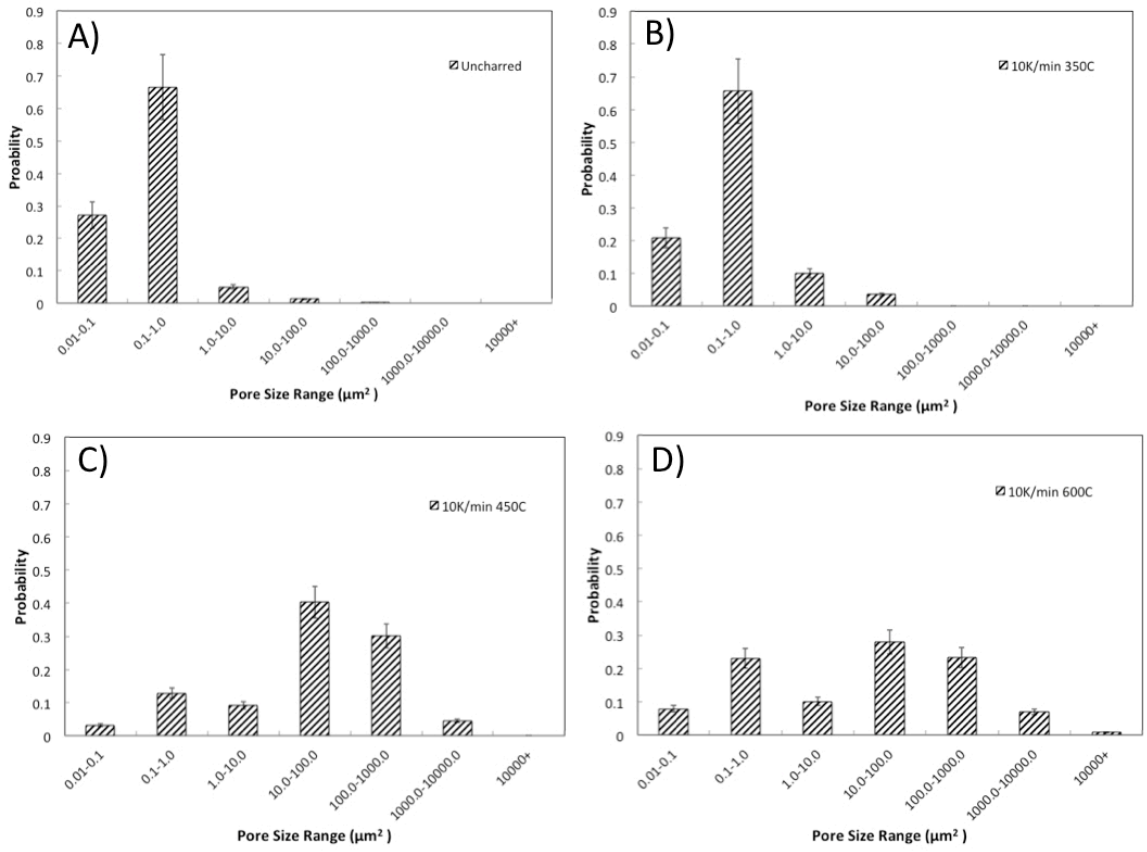

Figure 5. 10 Pore area probability distributions for coal cores heated at 10K/min to A)Uncharred B) 350°C C) 450°C D) 600°C

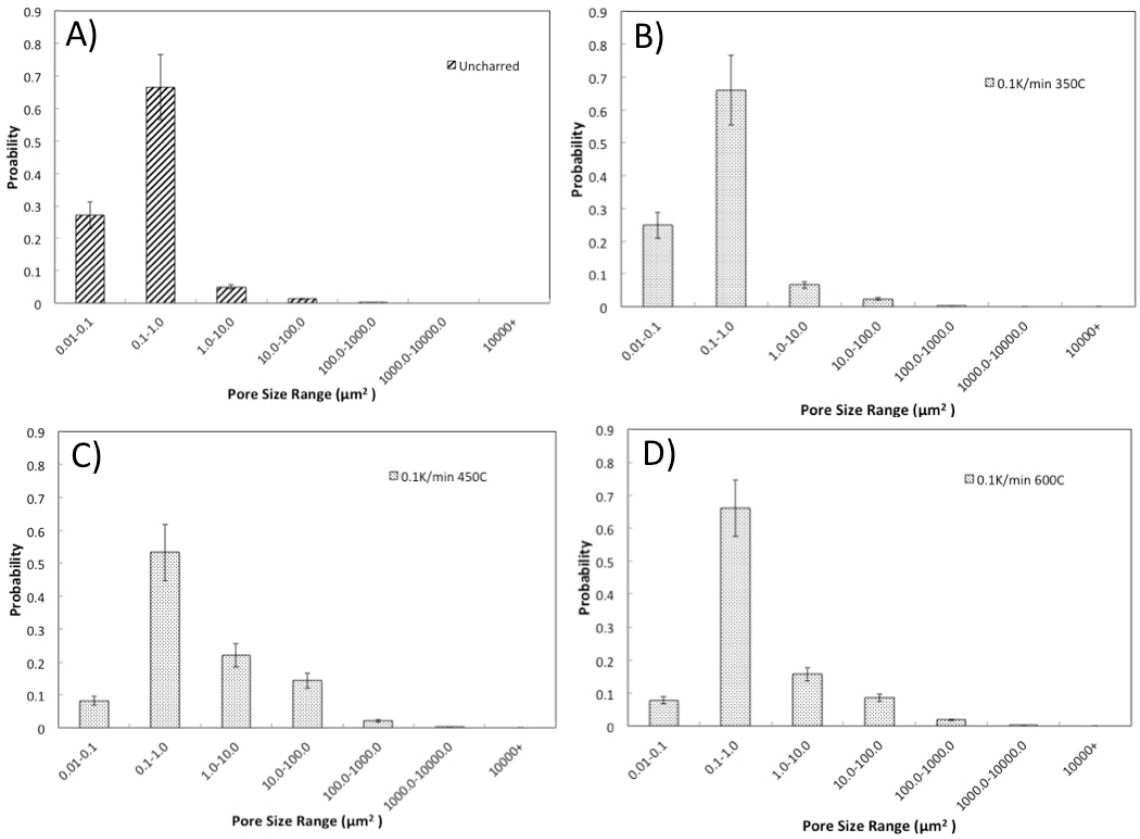

Figure 5. 11 Pore area probability distributions for coal cores heated at 0.1K/min to A)Uncharred B) 350^{o}C C) 450^{o}C D) 600^{o}C

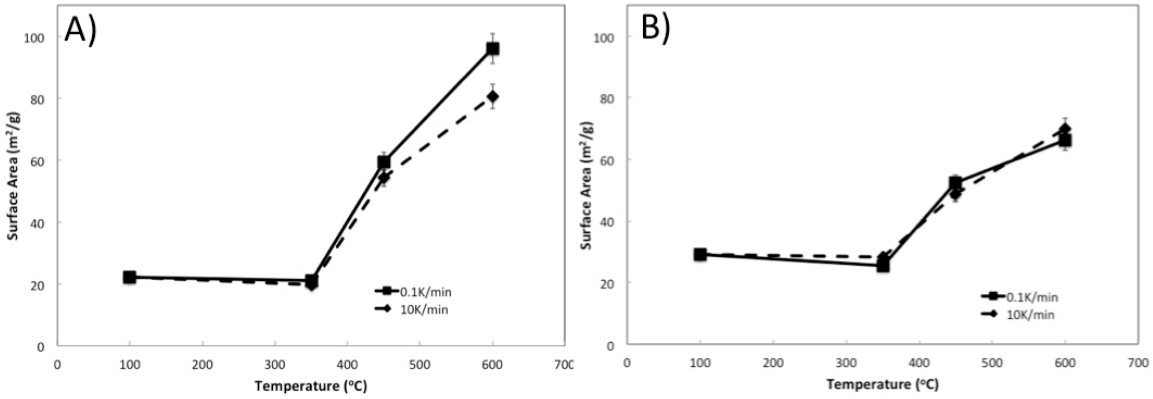

Figure 5. 12 Surface area measurements for pyrolyzed bituminous coal chars as a function of temperature and heating rate A) before acetone extraction B) after acetone extraction.

nonextracted chars at low pyrolysis temperatures and are lower at higher temperatures for all char samples. The decrease in surface area is most dramatic in the slowly-heated chars. After extraction, char surface area is primarily a function of pyrolysis temperature, not heating rate.

Total pore volumes in each char follow the same trends as BET surface area. Total pore volumes were calculated from a BJH adsorption analysis over a pore size range from 1nm to 250nm. Figure 5.13 shows total pore volumes before (5.13a) and after (5.13b) acetone extraction. The error bars represent one standard deviation based upon 3 replicate experiments. Before extraction, the total pore volume is larger for chars heated at 0.1K/min at 450^{o}C and above. After extraction, the most significant change occurs at 600^{o}C in the slowly-heated char, whose total pore volume decreases to below that of the more rapidly heated char. An analysis of incremental pore volumes in the micro- and mesoporous regions shows that most of the decrease in pore volume in the slow-heated char occurs from loss of pores sized 2 to 10nm. Figure 5.14 shows cumulative pore volumes in the mesoporous region before and after extraction under both fast and slow heating conditions. In general, major differences do not exist in the micro- and mesoporous structures between samples heated at varying heating rates.

Total pore volume analysis for cores heated at 0.1K/min to a particular temperature then instantaneously quenched suggests that tar retention may begin as low as 400^{o}C. Figure 5.15 shows total pore volumes for slowly-heated cores before and after acetone extraction. Before extraction, a surge in total pore volume is seen at 400^{o}C and continuing in a near-linear fashion to 600^{o}C. After extraction, the increase in total pore volume is significantly smaller on the interval of 400 to 500^{o}C, and nearly identical to the

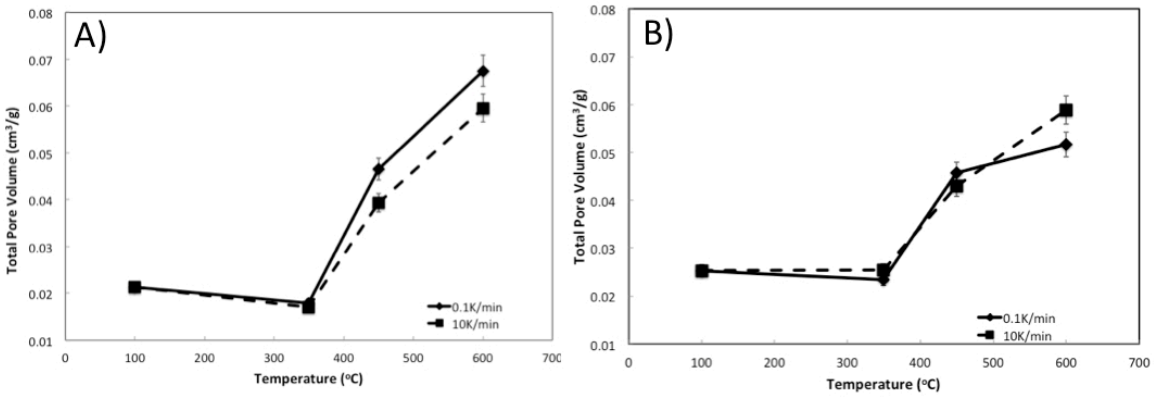

Figure 5. 13 Total pore volume measurements for pyrolyzed bituminous coal chars as a function of temperature and heating rate A) before acetone extraction B) after acetone extraction.

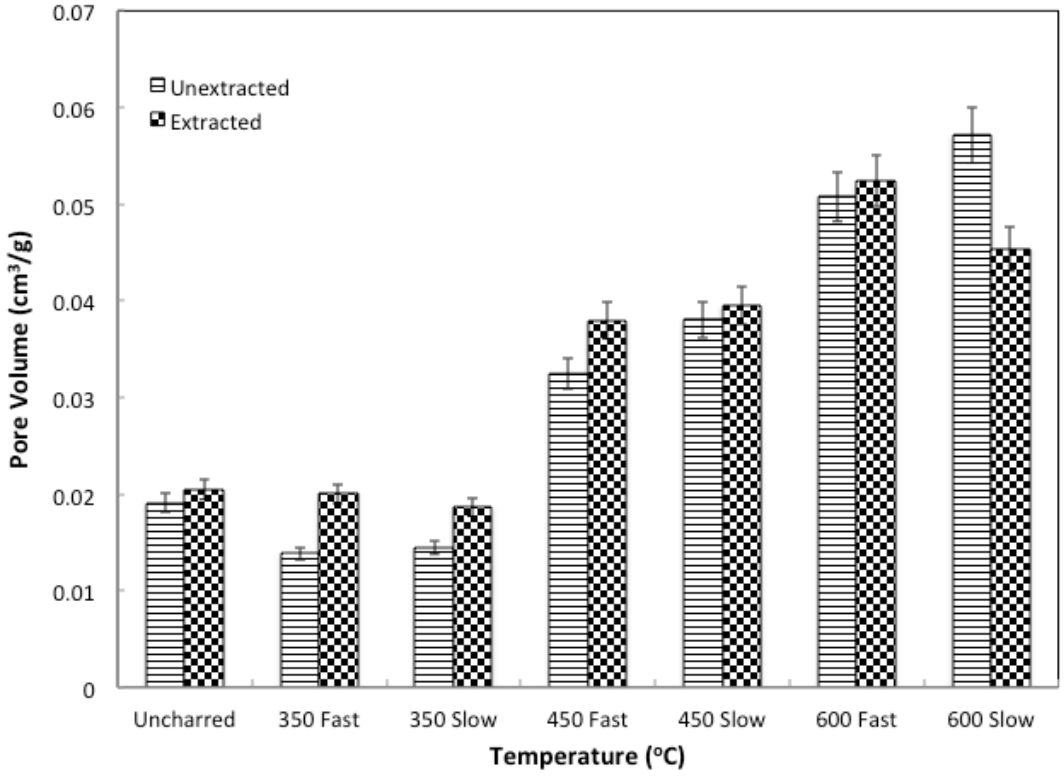

Figure 5. 14 Measured pore volumes in the mesoporous region (2-50nm) as a function of temperature for bituminous coal chars at fast (10K/min) and slow (0.1K/min) heating rates, before and after acetone extraction.

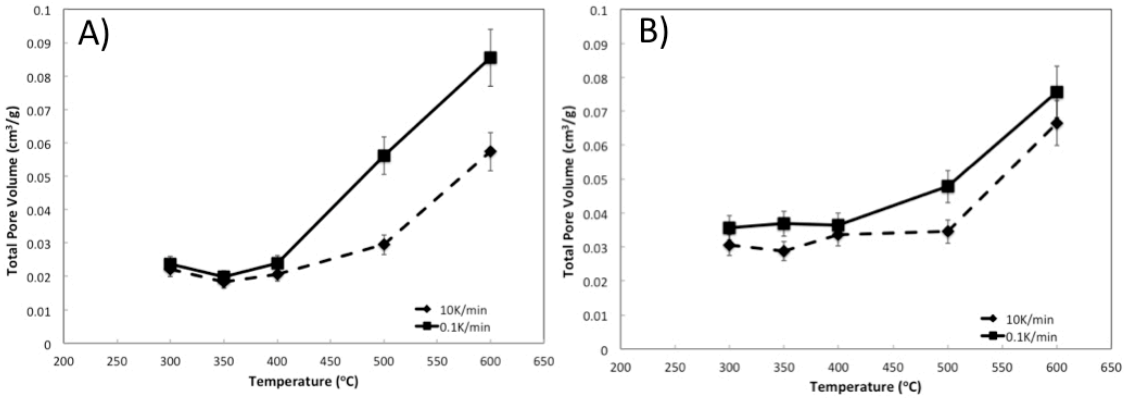

Figure 5. 15 Total pore volumes measured after coal chars were instantaneously quenched during pyrolysis A) before acetone extraction and B) after acetone extraction.

pre-extraction samples between 500 and 600^{o}C. This suggests that the retained liquid-phase components evolve between 400 and 500^{o}C.

Discussion of Core Results

The core porosity results highlight a number of significant effects for bituminous coal pyrolysis at low heating rates. First, a definite threshold occurs for plastic deformation. A substantial increase in macroporosity is not observed at 0.1K/min but is observed at 10K/min, provided the pyrolysis temperature exceeds 400^{o}C. This shows that the coal's native pore system is capable of accommodating mass transfer when the heating rate is very low. The lack of plastic deformation at the slowest heating rate would also imply that the successive activation of kinetic pathways at moderate pyrolysis temperatures occur gradually rather than sharply, causing no sudden surges in the devolatilization rate.

Second, pyrolyzed cores develop a bimodal macropore distribution at a higher heating rate, like the one measured in the block pyrolysis experiments. It is significant to note that the bimodal distribution is observed for a pyrolysis temperature of 600^{o}C at 10K/min heating rate, a condition at which the coal core was observed to swell to the full inner diameter of the reactor tube. As discussed in more detail below, this may suggest that the bimodal macropore distribution is an effect of confinement on the swelling phenomenon.

Third, despite the dramatic differences in macropore size and count observed between the two heating rates, very little difference is seen in the amount of micoporosity and mesoporosity. CO_2 adsorption data imply nearly identical internal surface areas and pore volumes for a given pyrolysis temperature for the two heating rates tested. The lack

of variation in micro- and mesoporous structure for the two heating rate suggests that the pressure buildup driving plastic deformation occurs at the interface between the mesoporous and macroporous networks.

Lastly, gas adsorption on very slowly heated chars may present an inaccurate picture of the surface properties of the char. Prior to acetone extraction, chars heated at 0.1K/min typically showed larger internal surface areas and pore volumes than those heated at 10K/min. Extraction was noted to produce a yellow coloration in the solvent phase. After extraction, the surface areas and pore volumes of the slowly heated chars decreased to match those of the more rapidly heated chars. Analysis of the gas adsorption data shows that the decreases come from a loss of mesoporosity. These results imply that the slowly heated chars may be retaining a liquid phase that can be solvent extracted. It is unclear whether this liquid phase retains some structure at room temperature that provides adsorption sites or solubilizes gas into the liquid. Although removing trapped material from the pore system would bring an expected increase in total pore volume, the apparent decrease in pore volume after removal of the liquid from the pore system may arise from CO_2 solubilization in the trapped liquids.

Confinement Effects

Coal cores were pyrolyzed under volumetric confinement to determine the effect of swelling inhibition on porosity, bridging the gap between the coal core experiments and the block pyrolysis experiments. Confinement was accomplished by encasing coal cores within an aluminum vessel whose inner diameter matched the outer diameter of an unheated coal core.

Confinement has a pronounced effect on coal porosity at a heating rate of 10K/min. Figure 5.16 shows pore area probability distributions at various ultimate temperatures after rapid pyrolysis under confinement. The pore area distribution shows a bimodal pattern at 450^{o}C and an even more widely segregated bimodal pattern at 600^{o}C. The porosity results demonstrate an increasing trend toward much larger pore sizes when the coal core is prevented from swelling. A core heated to 450^{o}C at 0.1K/min under confinement showed no change in its pore size distribution, suggesting that confinement had no effect on pore structure when swelling did not occur.

A total absence of confinement shows a dramatically different pore morphology compared to a confined coal core. Figure 5.17 shows SEM micrographs for a coal core heated to 600^{o}C with complete confinement (5.17a) and a coal core heated to 600^{o}C with full freedom to expand (5.17b). The final porous morphologies are unique to each with much smaller average pore sizes seen under unrestricted conditions and larger pores under confined conditions. Figure 5.18 shows pore size probability distributions for these two cases as well as the distribution for cores heated to 600^{o}C in the 1" tube furnace, a case that partially inhibited swelling. The distributions show a progressive pattern from a broadly distributed pattern under expansion to a widely separated bimodal distribution under full confinement.

The mechanical inhibition of swelling substantially affects the macropore size distribution of a bituminous coal. It should be noted that porosity for confined samples was observed by SEM near the core centers to ensure no unintended effects caused by the walls of the confinement vessel. The effect of confinement at a point well removed from the wall suggests that the confinement force exerts over a substantial distance. Although

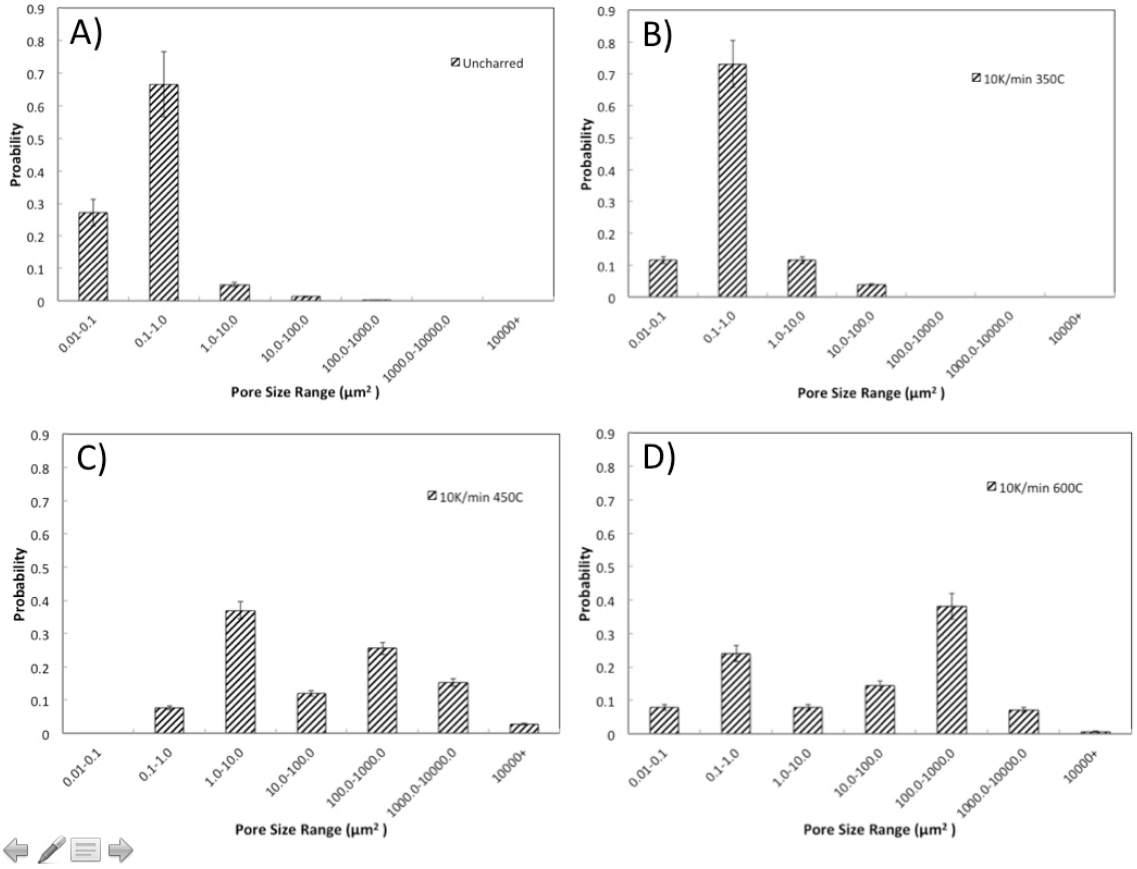

Figure 5. 16 Pore area probability distributions for coal cores heated at 10K/min under volumetric confinement to A) Uncharred B) 350°C C) 450°C D) 600°C

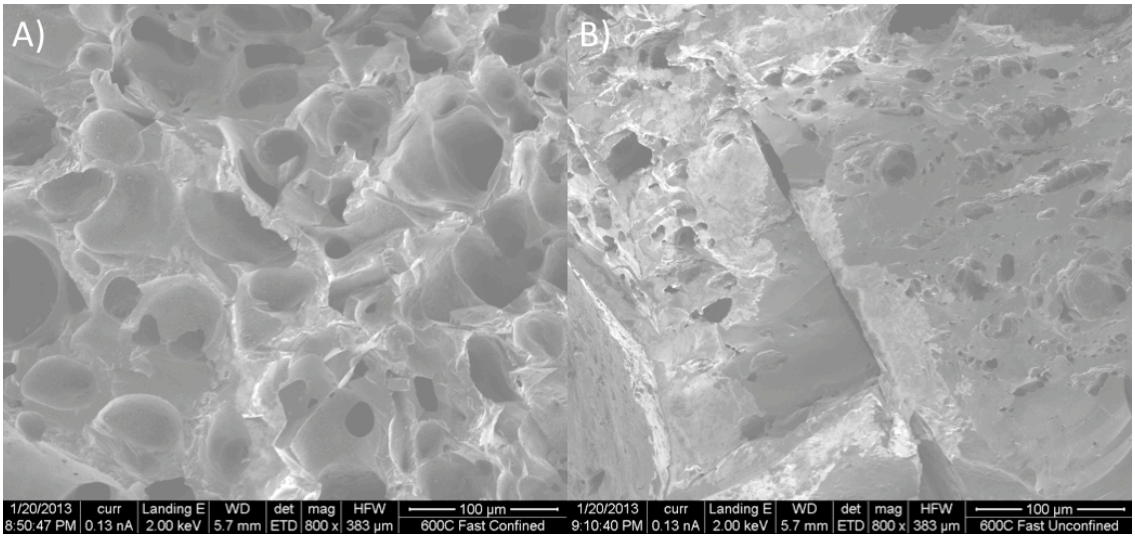

Figure 5. 17 SEM micrographs of bituminous coal cores heated at 10K/min to 600°C with A) full volumetric confinement and B) no volumetric confinement. All scale bars 100 µm.

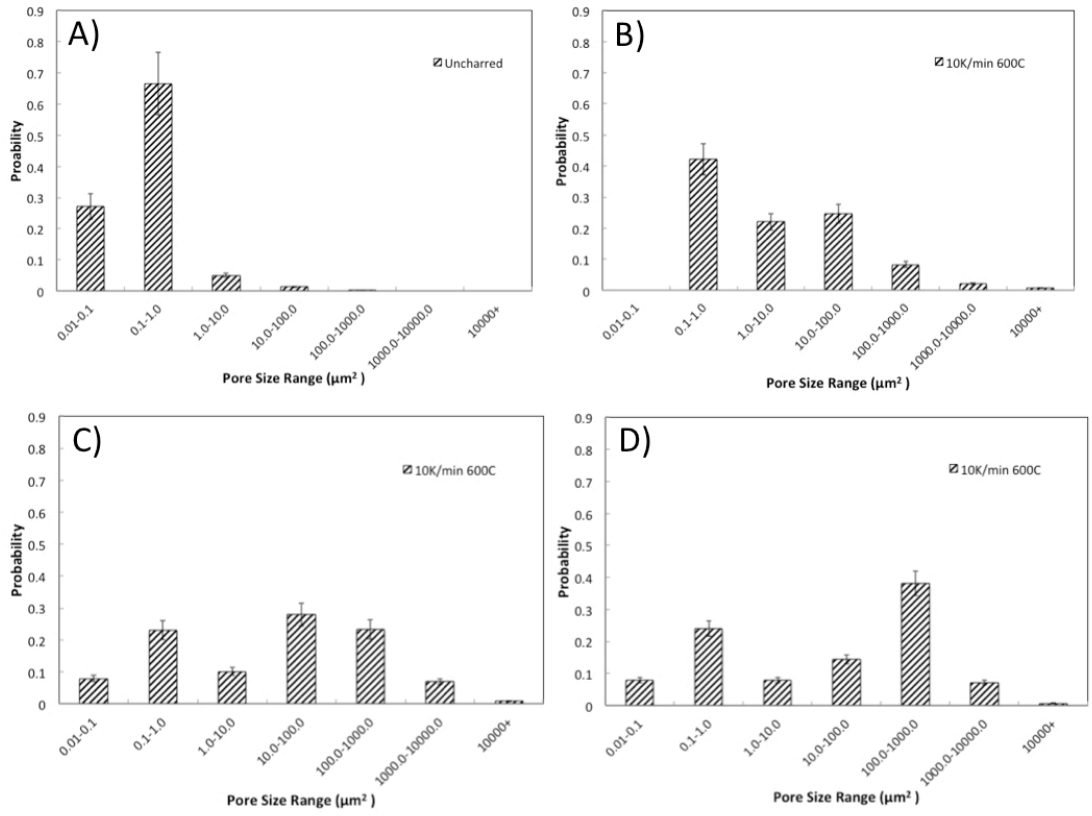

Figure 5. 18 Pore area probability distributions for coal cores pyrolyzed at 10K/min under varying degrees of volumetric confinement. A) Uncharred B) None C) Partial D) Full

the metaplast concept in plastic deformation posits a semisolid structure during rapid devolatilization, the data presented here suggest that a greater sense of order is maintained in the char structure to resist swelling deformation. This then seems to allow greater pressures to build in the pore spaces, leading to larger bubble ruptures when failure does occur.

Conclusions

Porosity changes were analyzed in large bituminous coal blocks pyrolyzed via embedded heaters as well as in free and volumetrically-confined coal cores pyrolyzed in tube furnaces. Pyrolysis was performed at heating rates of 0.1K/min and 10K/min in the temperature range of 350^{o}C to 600^{o}C. Macropore size distributions were derived from SEM image sets and surface areas, pore volumes and micro- and mesopore size distributions were collected from CO_2 adsorption isotherms via BET and BJH analyses. Several effects were observed that may be relevant to coal thermal processing in subsurface environments.

The development of large macropores associated with plastic swelling and deformation of the coal structure occurred at temperatures of 450^{o}C and above at 10K/min heating rate, but did not occur at 0.1K/min heating rate, regardless of ultimate pyrolysis temperature. Bimodal macropore size distributions were measured in samples where plastic deformation had occurred and some degree of volumetric confinement was present. This suggests that inhibition of swelling increases the pressure needed to allow product bubbles to rupture through the coal solid structure. In coal blocks, larger macropores were seen to recede in size over extended pyrolysis times. This effect was attributed to the deposition and coking of tars evolved from deeper within the block.

Extensive fracturing was observed in regions of the coal blocks removed from the heat source, but was not seen in any core samples. The effect is attributed to the mechanical relaxation of stresses caused by thermal expansion or devolatilization pressure.

The micro- and mesoporous structure of pyrolyzed bituminous coal was seen to vary little after complete pyrolysis at 0.1K/min or 10K/min heating rates. BET surface areas and total pore volumes over the size range of 1nm to 250nm were seen to be nearly identical for a given ultimate pyrolysis temperature. These trends were apparent only after samples had been extracted in refluxing acetone, yielding a colored solvent. Prior to extraction, samples heated at 0.1K/min showed increasingly higher internal surface areas and total pore volumes compared to those heated at 10K/min. The apparent decrease in total pore volume after removal of an acetone-soluble component from the pore system of the slowly-heated chars suggests that the acetone-soluble species may have been solubilizing CO_2 rather than adsorbing it.

The presented work bears relevance to coal pyrolysis in subsurface systems where heating rates are expected to be very low, perhaps on the order of degrees per day. At such heating rates, the pore system of a bituminous coal is capable of accommodating mass transfer of volatile species without swelling or deformation. This result is important because it shows that the modeling of subsurface mass transfer in extended coal seams during thermal processing can use the native coal macroporosity to handle bulk transfer processes. The possible retention of a liquid phase in the pore system of slowly-heated bituminous coal chars is also a significant result for subsurface processing for two reasons. First, it would imply that product yields and compositions obtained at higher heating rates would not be representative of those at very slow heating rates. Second, the

affinity for CO_2 adsorption or solubilization in this liquid phase may suggest an enhanced potential for carbon sequestration in coal seams that have undergone some degree of thermal processing.

CHAPTER VI

DEVOLATILIZATION AND MASS TRANSFER IN LARGE COAL DOMAINS DURING PYROLYSIS AT VERY SLOW HEATING RATES

The purpose of this chapter is to describe the observed trends in devolatilization for large particles of bituminous coal and correlate them to the porosity trends described in Chapter 5. Char yields are described for samples that have been pyrolyzed to completion, and char and tar yields are measured at instantaneous points during pyrolysis to compare the devolatilization trends at varying heating rates. Additional evidence is presented for the retention of a liquid-phase component within the char structure of samples heated at very slow heating rates. The chapter concludes with a simplified analysis of pressure-driven Knudsen flow to estimate an order of magnitude for the critical pore pressure to displace trapped liquids from the micro- and mesoporous structures of the slowly-heated coals.

Knudsen Analysis

This section gives a description of the mathematical methods used to estimate the pore pressure gradient during devolatilization, including the relevant assumptions given the available data. The purpose of this analysis is not to determine a precise pressure gradient, but rather to bound the threshold pressure gradient for displacing liquid

condensates from the smaller pores during devolatilization. The mathematical description presented here follows the work of Javadpour *et al.* [2007; 2009].

The total mass flux flowing through a nanoscale-sized pore can be considered a combination of flux due to Knudsen flow and advective flow, given as:

$$J = J_K + J_A \tag{1}$$

Knudsen flow is important in nanopores because the characteristic size of the pore is often much smaller than the mean free path of individual gas molecules, increasing the likelihood that collisions with the pore wall will provide resistance to molecular movement. A theoretical expression for the mass flux for Knudsen flow can be derived from the kinetic theory of gases as:

$$J_K = \frac{2rM}{3R_gT}\sqrt{\frac{8R_gT}{\pi M}}\nabla P \tag{2}$$

At the nanoscale, the no-slip boundary condition for advective flow is often invalid. In such cases, it has been argued that slip-flow is a better model for flow. In the situation of pyrolyzing coal, it is likely that fragmentation and recondensation of the coal structure creates a rough, nonstatic pore surface, boosting the validity of this assumption. In this description, the advective mass flux term is derived using the common Hagen-Poiseuille equation for fluid flow:

$$J_A = F\frac{r^2\rho_{avg}}{8\mu}\nabla P \tag{3}$$

The F term in equation 3 is a slip-flow analogue of the friction factor used in no-slip flow. For slip flow, it represents the increase in mass flow caused by slip at the fluid/pore

wall interface. A semitheoretical development of F by Brown *et al.* gives this term as [Brown, 1946]:

$$F = 1 + \left(\frac{8\pi RT}{M}\right)^{1/2} \frac{\mu}{p_{avg} r}\left(\frac{2}{\kappa} - 1\right) \tag{4}$$

In equation 4, κ is a measure of wall roughness that can range from 0 to 1. For the presented analysis, a value for κ of 0.5 is assumed due to lack of better information. Combining equations 2 and 3 and rearranging, an expression for the pressure gradient is obtained:

$$\nabla P = J\left[\frac{2rM}{3RT}\left(\frac{8RT}{\pi M}\right)^{1/2} + F\frac{r^2 \rho_{avg}}{8\mu}\right]^{-1} \tag{5}$$

Experimental data collected for this work provide values for J, r and T in equation 5. It is necessary to provide values for M and μ. M is assumed to be a weighted average of the molecular weights of representative gas species. The gas is assumed to be composed largely of H_2, CH_4, CO and CO_2, having an average molecular weight of ~17kg/kmol. The liquid phase is assumed to have an average molecular weight of 150kg/kmol. The precise weighting of gas to liquid was determined from experimental data. Gas viscosity was determined as a function of temperature using the Sutherland equation:

$$\mu(T) = \lambda\frac{T^{3/2}}{T+C} \tag{6}$$

Due to the wide number of species composing the gas phase, it is difficult to say the precise values for the parameters λ and C in equation 6. Consequently, CO_2 was chosen as a representative gas due to its moderate viscosity. The Sutherland parameters for CO_2

are $\lambda = 1.572 \times 10^{-6}$ Pa s $K^{-1/2}$ and C = 240 K [51]. A detailed discussion of how experimental data were applied to this analysis is given in Appendix C.

Results and Discussion

Volatile matter yields for bituminous coal cores are observed to be a strong function of temperature and a weak function of heating rate. Figure 6.1 shows volatile matter yields on a dry, ash-free basis after 24hrs of pyrolysis for both coal cores and powdered coals. The data for each condition are averaged over three different coal samples whose properties are described in Table 3.1 of Chapter 3. In general, coal cores heated at 10K/min show slightly higher volatile matter yields at ultimate temperatures of 450°C and above. A comparison of powdered coal samples gives a slightly larger volatile matter yield at a heating rate of 10K/min, but a larger measurement error decreases confidence in this trend. In general, the heating rate is seen to correlate less strongly to volatile matter yields than temperature.

It should be noted that volatile matter yields varied between different coal samples, but the observed differences between yields based upon heating rate were consistent. Table 6.1 shows the volatile matter yields for coal cores from all three samples at each ultimate temperature and heating rate. The ratio of volatile matter yield at the faster heating rate to that of the slower heating rate shows no trend at 350°C but consistently gives a higher yield at the faster heating rate at 450°C and above. The variability of the data is smallest at 600°C. This shows that coal cores heated at 10K/min will give a reproducibly small but real increased yield of volatile matter at higher pyrolysis temperatures.

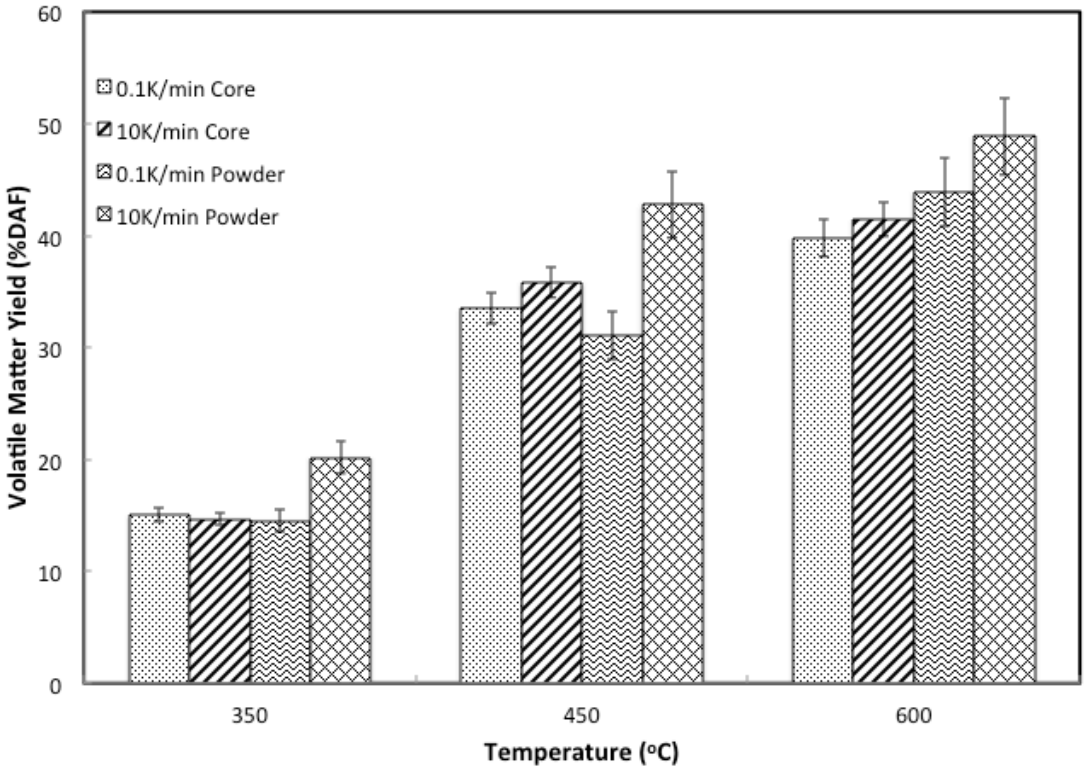

Figure 6. 1 Volatile matter yields for bituminous coal cores and powders as a function of temperature and heating rate.

Table 6. 1 Comparison of volatile yields from all tested coals

Temperature (°C)	Coal	VM Yield (% DAF) 0.1K/min	VM Yield (% DAF) 10K/min	Difference (%)
350	1	15.3	16.4	1.1
	2	15.2	16.1	0.9
	3	14.4	11.5	-2.9
450	1	36.1	36.5	0.4
	2	33.2	34.8	1.5
	3	31.2	36.1	5.0
600	1	38.9	40.5	1.6
	2	37.9	40.0	2.2
	3	42.6	43.9	1.4

The global kinetic trends for coal core pyrolysis also show a strong temperature effect but a lesser impact from heating rate. Figure 6.2 shows volatile matter yields from coal cores over the course of pyrolysis for both 10K/min and 0.1K/min heating rates. The x-axis has been normalized such that the time from room temperature to the ultimate temperature, e.g. 43mins at 10K/min and 4300mins at 0.1K/min to 450^{o}C, has a unit of 1 and each subsequent hour of pyrolysis at the ultimate temperature has a unit of 1. Cores heated at 10K/min show some degree of thermal hysteresis due to heat transfer limitations; however, this limitation is overcome at higher pyrolysis temperatures. For an ultimate temperature of 600^{o}C, the volatile matter yield for faster heating has caught up to the yield for slower heating by the time the reactor reaches its final temperature. Cores heated to 600^{o}C are also seen to consistently yield 2 to 3% more volatile matter at 10K/min heating rate than 0.1K/min.

Heating rate shows a more discernible effect on tar yield. Figure 6.3 shows measured tar yields for data points corresponding to volatile matter yields in Figure 6.2. The maximum tar yield was measured as 112mg/g coal at 600^{o}C for a 10K/min heating rate, but the tar yield was only 48mg/g coal at 0.1K/min at the same ultimate temperature. The significant decrease in tar yield between 10K/min and 0.1K/min demonstrates a threshold for liquid yield at very slow heating rates. It should be noted that the method of tar collection employed in this work did not collect the lighter tars or oils, likely leading to lower liquid yields than might be expected from a bituminous coal. Due to the difficulty of accurately measuring small quantities of tar obtained by solvent extraction, tar samples were not collected from within the char samples. It is unknown whether the

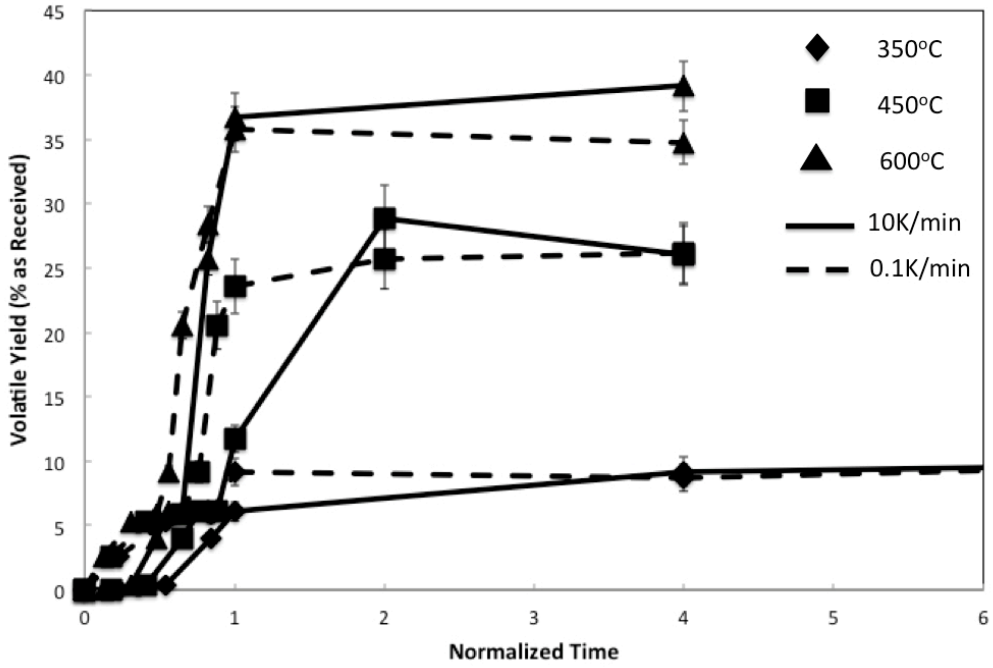

Figure 6. 2 Volatile matter yields for bituminous coal cores at various temperatures and heating rates

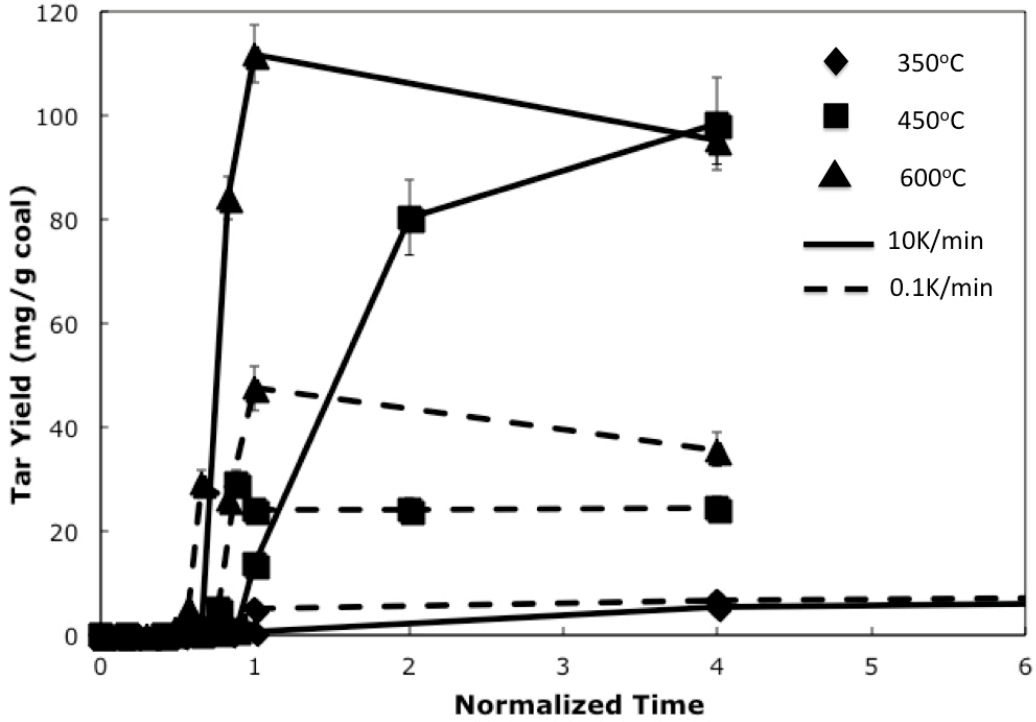

Figure 6. 3 Tar yields for bituminous coal cores at various temperatures and heating rates.

discrepancy in tar yields could be accounted for by deposition within the char, although the similarity in char yields as a function of heating rate makes this less likely.

Particle size may have some effect upon the tar yield at very slow heating rates. Figures 6.4 and 6.5 show volatile matter yields and tar yields, respectively, over the course of pyrolysis at 10K/min and 0.1K/min for particles spanning three orders of magnitude in average diameter. At a heating rate of 10K/min, particle size does not substantially affect the ultimate tar yield once the pyrolysis temperature has reached 600^{o}C. The differences in tar yield at lower temperatures may be due to heat transfer conditions for different particle sizes since tar yield measurements were made instantaneously when the furnace reached the setpoint temperature. The largest particles were likely substantially cooler on average at lower setpoints. At 600^{o}C for a 0.1K/min heating rate, tar yields are seen to peak at 65 mg/g coal for 75 μm particles compared to 48 mg/g coal for 2cm cores and 29 mg/g coal for 3mm particles.

The particle size effect on tar yields at very slow heating rates suggests a complicated mechanism for inhibition of tar yields. The difference in tar yields between 75 μm particles and 2 cm cores would represent 2-4% of the total mass of coal as received, an amount similar to the difference in volatile matter yields between slowly and more rapidly heated cores. The previously-described study of bituminous coal porosity by CO_2 adsorption has given evidence for the trapping of acetone-soluble tars within the pore structure of coals heated at 0.1K/min, but not coals heated at 10K/min. The volatile matter data presented here would support this theory and further suggest a relationship between particle size and devolatilization rate in the ability to displace condensing tars from the mesoporous structure of the coal.

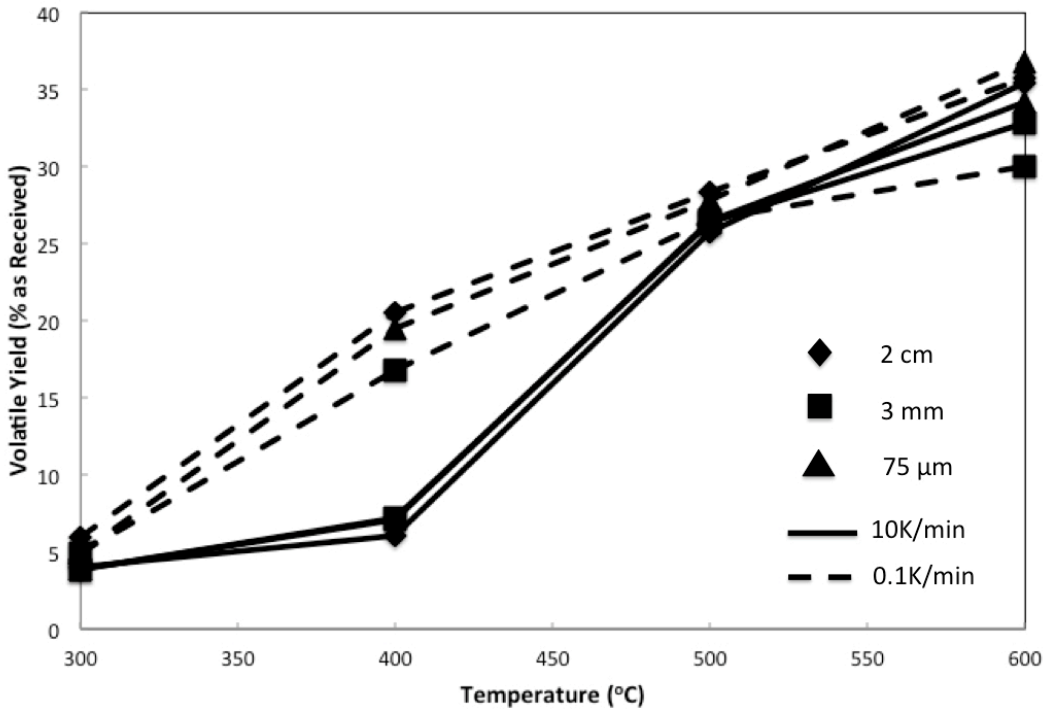

Figure 6. 4 Volatile matter yields during pyrolysis for various particle sizes and heating rates.

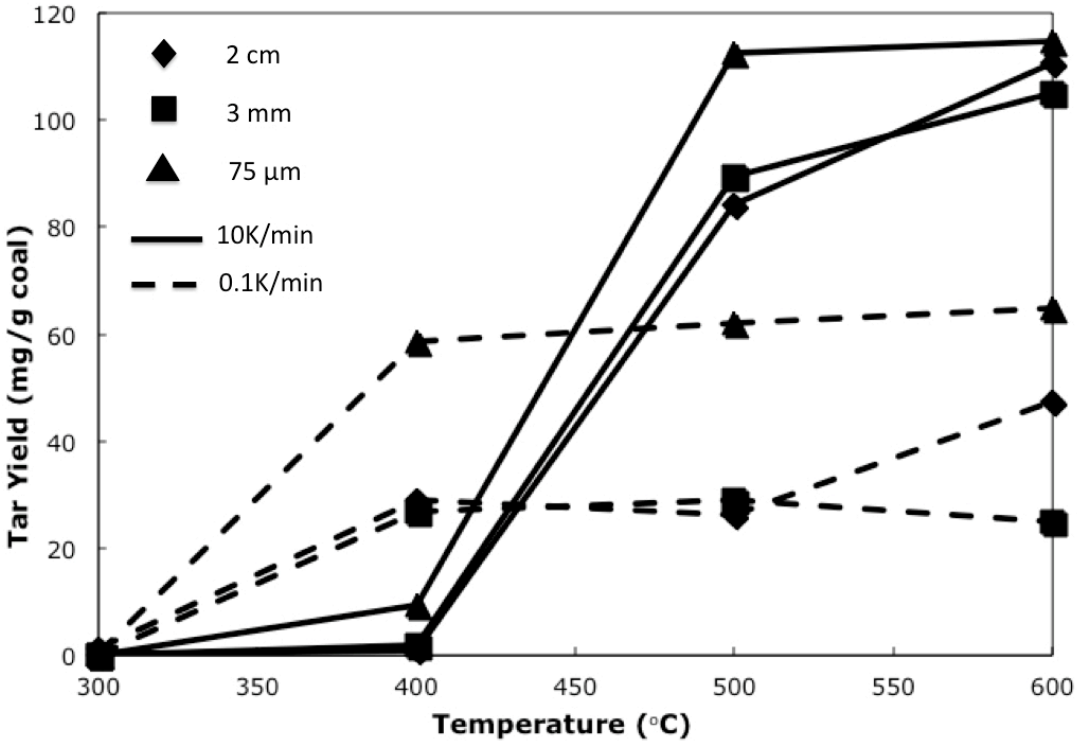

Figure 6. 5 Tar yields during pyrolysis for various particle sizes and heating rates.

An estimate of the necessary pressure gradient to displace trapped tars has been performed assuming pressure-driven Knudsen flow in the micro- and mesopores of the coal. Because the volatile evolution rates shown in Figures 6.2 and 6.4 showed devolatilization from the coal to be a function of temperature with any discrepancies in rate arising from heat transfer effects, TG analysis of 38 μm coal particles was used to obtain high-resolution mass flux data as a function of temperature. The TGA experiments were performed in similar fashion to all pyrolysis experiments, with a linear heating ramp to a final temperature, then a 24hr hold at the ultimate temperature. Figure 6.6 shows mass flux rates derived from TGA data for 10K/min and 0.1K/min heating rates. The peak devolatilization rate is seen near 450^{o}C for a 10K/min heating rate and 375^{o}C at 0.1K/min. A very broad but shallow secondary peak in the rate is seen at 540^{o}C at 10K/min heating rate. This secondary peak is more pronounced near 470^{o}C at 0.1K/min heating rate. The secondary peaks do not exceed the maximum devolatilization rates for both cases and in general, the flux of products from the coal structure decreases very slowly over the course of pyrolysis, suggesting that no sudden surges in devolatilization occur.

An analysis of Knudsen flow in the mesoporous system suggests a complicated mechanism for tar displacement. Given that the micro- and mesoporous structure of coal seems to evolve irrespective of particle size, little difference is seen in the pressure gradient necessary to drive mass transfer at the observed devolatilization rates. Figure 6.7 shows predicted pore overpressures (difference above atmospheric) for the studied particle sizes at 0.1K/min. The calculation shows over 1 atm of pressured differential is needed to drive mass transfer from the center of a 2cm core, but only 0.01 atm of

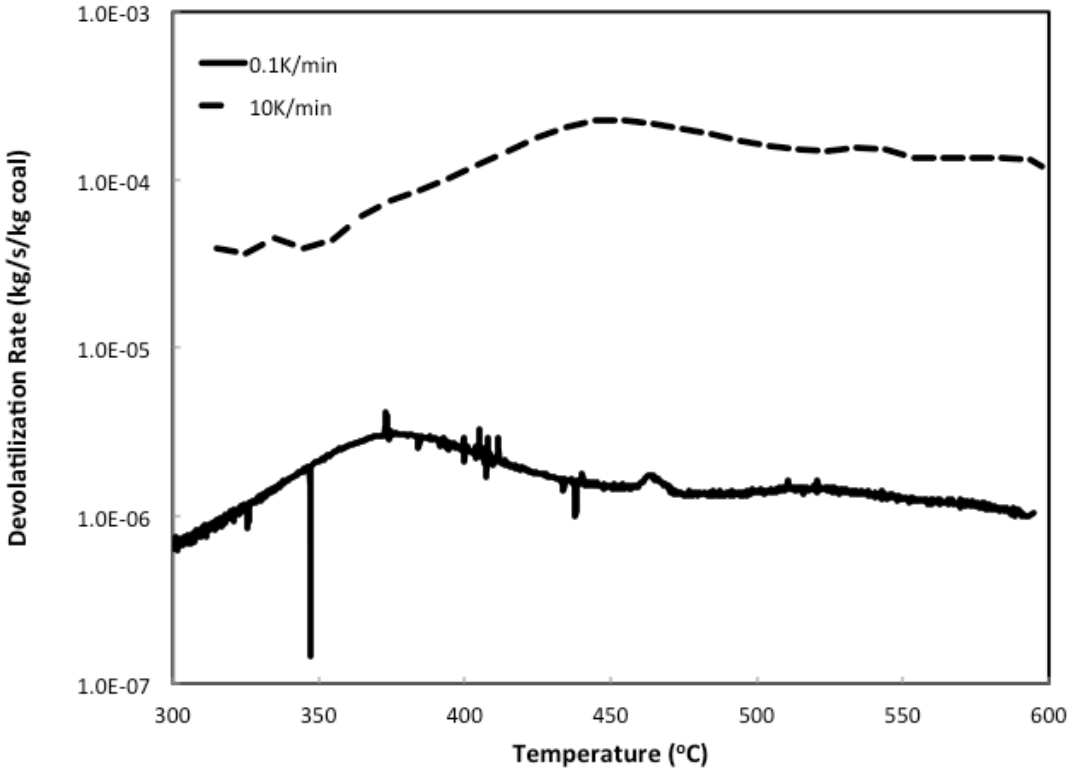

Figure 6. 6 Devolatilization rates measured by TGA for slow and fast heated bituminous coal powders.

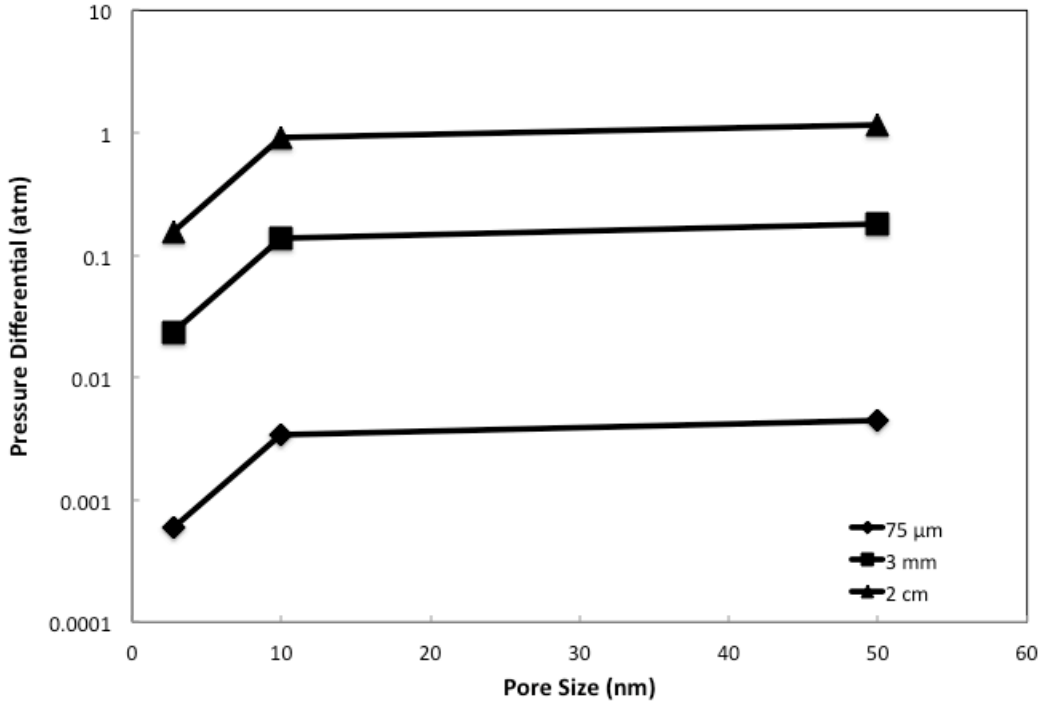

Figure 6. 7 Estimate of pressure differentials in nanopores at 0.1K/min heating rate for various particle sizes.

differential is needed from a 75 μm particle. Although the calculations show a larger pressure differential to drive tars out of the pore system in larger particles, a higher pore pressure would also encourage condensation of less-volatile components in the pore system. If this is occurring more readily in larger coal particles, the displacement of tars from clogged pores would depend upon the surface tension of the condensed tar. This value would be a complex function of temperature and tar composition.

Knudsen flow analysis also offers some insight into the necessary pressure to trigger plastic deformation in coal chars. Figure 6.8 shows pressure differential calculations for various particle sizes. For a 2cm core, a pressure differential of nearly 100atm is necessary to drive mass transfer during the peak of devolatilization while a pressure differential on the order of 0.1atm drives mass transfer in a 75 μm particle. The results fit the qualitative picture since a larger particle will require more pressure to deform the existing solid structure during pore enlargement.

It should be noted that the difference in tar yields between coal samples heated at 0.1K/min and those heated at 10K/min cannot be fully explained away by a tar-trapping mechanism. A gap of approximately 50mg/g coal exists between slowly and rapidly heated cases when heated to 600^{o}C, although this difference is not reflected in total volatile yields. Consequently, it is suggested that part of the decrease in tar yields can be attributed to the loss of tar formation pathways at very slow heating rates. Figure 6.9 shows a conceptual diagram of concentrations of hypothetical tar-forming components within the coal at slow and fast heating rates. It should be noted that the tar precursors in Figure 6.9 could include gas phase species and reactive species still bound within the

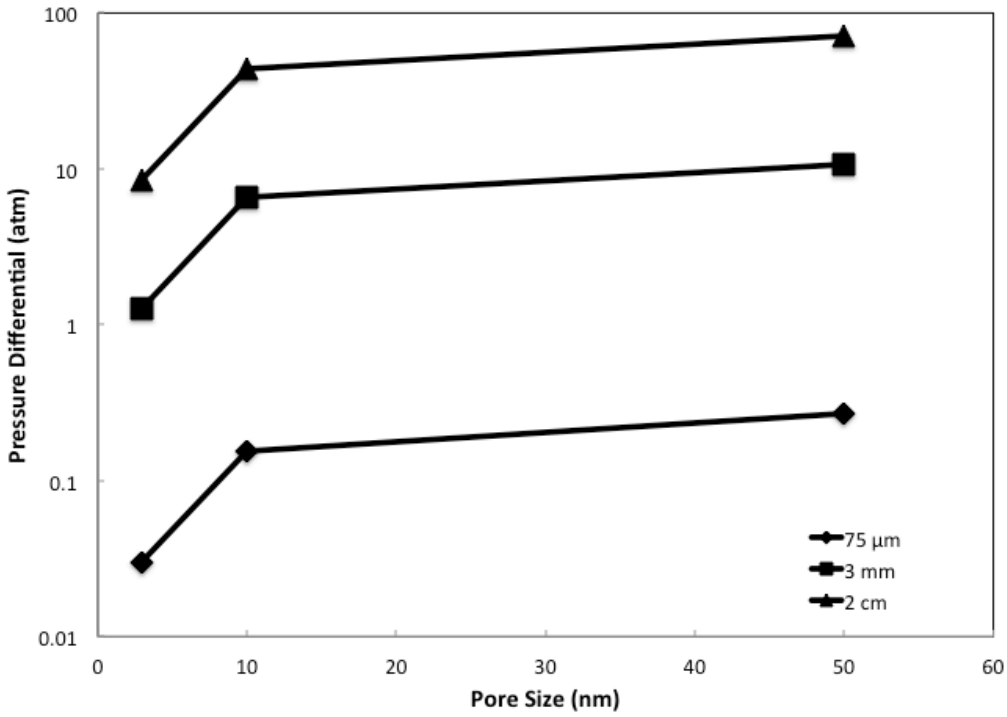

Figure 6. 8 Estimate of pressure differentials in nanopores at 10K/min heating rate for various particle sizes.

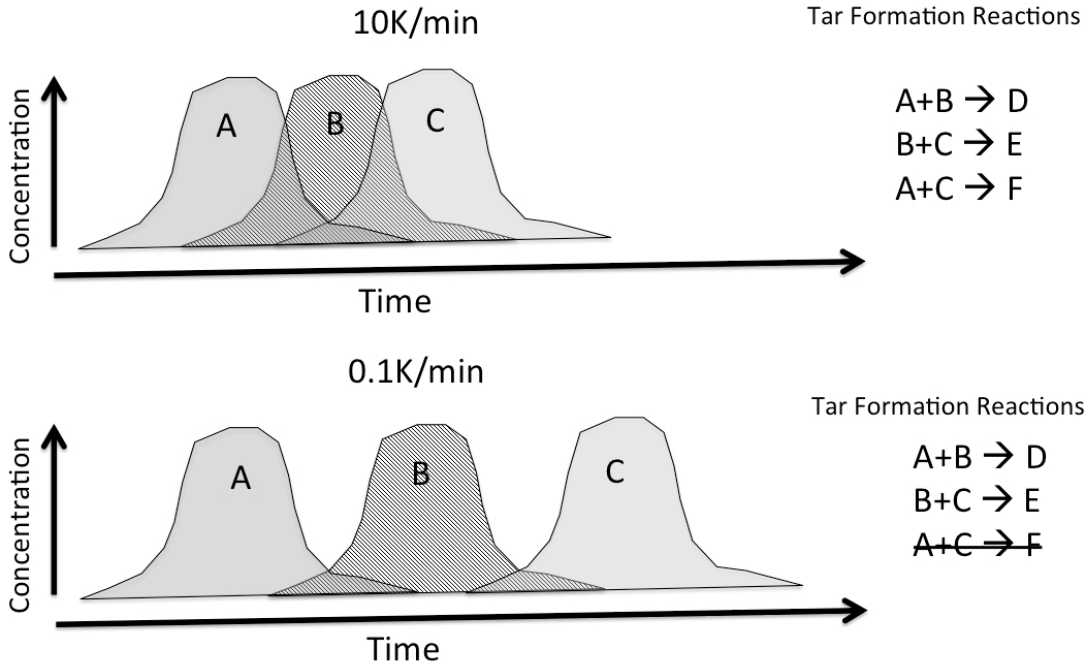

Figure 6. 9 Hypothetical tar precursor reaction scheme showing the impact of mass transfer on reaction pathways from the coal particle at very slow heating rates.

coal's macromolecular structure. In the slower heated scenario, certain components will have mostly devolatilized and evolved from the coal particle before they have the opportunity to react with components devolatilized at higher temperatures.

The idea of limitations in tar formation pathways is supported experimentally in this work and prior studies. From the presented TGA data, the sharper secondary peak seen in Figure 6.6 at 0.1K/min supports the idea that slower heating rates may partially deconvolute classes of reactions that would normally occur simultaneously at fast heating rates, supporting the idea that certain tar precursors evolve sequentially. Further, related porosity studies [see Chapter 5] have shown no evidence of deformation to the pore system of the observed bituminous coal at 0.1K/min heating rate, demonstrating that the pore system is capable of facilitating mass transfer at this heating rate. Several studies have concluded that internal mass transfer limitations are an important source of increased tar yield in bituminous coals at higher heating rates due to the increased potential for side-reactions of cleaved coal fragments [Anthony, 1976; Gavalas, 1980]. It is established that tar formation is governed by a simultaneous competition between fragmentation of the macromolecular structure into radicals, cross-linking of the macromolecular structure, recondensation of radicals and hydrogen abstraction (radical termination) [Solomon, 1992]. Low-temperature cross-linking is associated with an increase in tar molecular weight due to the eventual evolution of larger polyaromatic molecules partially composed of tar precursors that could have been evolved earlier [Smith, 1994]. Bituminous coals have been reported to experience minor amounts of cross-linking until above the temperature zone for tar evolution [Suuberg, 1985]. This might increase the likelihood that low-temperature fragments could fully detach, quench

and evolve before recondensation or cross-linking reactions could occur. This would increase the amount of light hydrocarbons and light oils evolved, neither of which could be quantitated by the collection methodology employed in this study.

It should also be noted that the devolatilization data support the idea that pressure-driven flow is the dominant mechanism for mass transfer, even at very slow heating rates. From the basic equations of change, characteristic time scales for diffusion and pressure-driven flow can be estimated as, respectively:

$$t_{c,diff} \sim \frac{L^2}{\mathcal{D}_{AB}} \tag{7}$$

$$t_{c,pres} \sim \frac{\rho v L}{\Delta p} \tag{8}$$

Even assuming a high value for the value of the binary diffusivity in equation 7, the experimental data still show that the characteristic time scale for pressure-driven flow is over ten orders of magnitude smaller than the time scale for molecular diffusion. Although the calculation is only a first-order approximation with substantial uncertainty, it is likely that pressure-driven flow will still be the dominant mechanism of mass transfer in larger coal blocks even at slower heating rates than those presented in this study.

Conclusions

Char yields from bituminous coal cores are a weak function of heating rate and a strong function of temperature during pyrolysis at the slow heating rates considered in this study. Tar yields are strongly related to heating rate with a peak tar yield of 112 mg/g coal at 10K/min and 47 mg/g coal at 0.1K/min. This decrease in tar yields at the slower

heating rate is at least partially due to the retention of soluble liquids in the pore space of the char. Particle size is shown to have some effect upon tar yields at very slow heating rates, with a peak tar yield of 65 mg/g coal at 0.1K/min. An analysis of Knudsen flow in the mesopore system based upon available devolatilization data shows up to 1 atm of pressure differential and 100 atm of pressure differential driving mass transfer from a 2cm core during pyrolysis at 0.1K/min and 10K/min, respectively. A basic scaling analysis gives a characteristic time scale for pressure-driven flow in the observed coal particles that is still many orders of magnitude smaller than the time scale for diffusion, suggesting pressure-driven flow is the dominant mass transfer mechanism even at very slow heating rates.

The studies described here are consistent with the previous description of pore-plugging in bituminous coals heated at very slow heating rates. The mechanism of tar retention in the porous network is still unclear and may involve related phenomena including tar composition, phase equilibria and surface tension in micropores. A more thorough understanding of the tar compositions of trapped and evolved tars over the course of pyrolysis may offer a more thorough understanding of the physics causing tar retention.

This study is important to understanding subsurface thermal processing of coal seams because of the apparent change in devolatilization phenomena below a threshold heating rate of 10K/min. Detailed kinetic data obtained at heating rates of 10K/min and above will not sufficiently describe the expected product distributions for subsurface pyrolysis at very slow heating rates. Although char yields are not affected much by heating rate, liquid yields are greatly suppressed, meaning a gas product that is richer in

tar precursors. Additionally, the retention of a trapped liquid phase in the coal's pore system for extended duration at elevated temperatures and pressures will likely drive the gas yields even higher due to tar coking reactions. To properly predict the devolatilization kinetics at 0.1K/min and slower, separate kinetic studies will need to be performed and compared to studies at higher heating rates.

CHAPTER VII

CONCLUSIONS

The work described in this dissertation represents an investigation of the phenomena of coal pyrolysis in very large particles at very slow heating rates. The context of the research is underground coal thermal treatment (UCTT), a proposed nonconventional hydrocarbon production method that would utilize deep coal seams. The idea draws in large part from related subsurface processing techniques, including underground coal gasification, *in situ* oil shale retort and coal-bed methane production. These fields are all rapidly maturing but questions remain how these processing methods would translate into sequestered coal seams. This dissertation seeks in some small part to begin to address some of the underlying questions regarding UCTT.

As with most subsurface techniques, it is anticipated that reservoir modeling will play an important role in the development of UCTT processing. In this context, many questions remain about the physical dynamics of heat transfer, mass transfer and primary and secondary pyrolysis kinetics within a coal seam that is being heated. Perhaps a most critical issue is identifying under what conditions bench scale physical data can be acquired to obtain a sufficient picture of coal pyrolysis under UCTT conditions. Based upon current best practices in other subsurface production methods, it is considered likely that heating rates within the coal seam would be measured in degrees per day. If this is the case, a relevant question would be what heating rate is sufficient to develop a

chemical kinetic model for coal decomposition and product evolution? The question is quite relevant because conventional pyrolysis studies have always achieved pyrolysis conditions on the time scale of seconds to hours where a UCTT process would achieve pyrolysis conditions on the time scale of months to years. The experimental effort required to heat samples and collect measurable products at such an extended time scale is onerous, so understanding the most efficient conditions to collect sufficient data is important to the validity of modeling efforts.

This dissertation has presented evidence of several phenomena that are not typically observed in the pyrolysis of small coal particles at high heating rates. Pyrolysis was studied in large blocks of bituminous coal as well as smaller coal cores to differentiate the evolution of porosity during pyrolysis when the heating rate is changed from 10K/min to 0.1K/min. Scanning electron microscopy (SEM) and low-pressure CO_2 adsorption were utilized to characterize changes to the porous network over the range of 1 nm to 100 μm. Devolatilization data including char yields and liquid yields were measured for a range of particle sizes from 75 μm to 2 cm at the same heating rates. A Knudsen flow analysis was performed based upon porosity and devolatilization data to determine the approximate pressure gradient driving mass transfer.

Key Results

Porosity changes in pyrolyzing blocks of bituminous coal were observed via SEM imaging. For a maximum heater temperature of 500^{o}C at a heating rate of 10K/min, coal near the heater surface was seen to develop larger pores consistent with plastic swelling of the coal structure. As pyrolysis progressed, these large pores became occluded with coked tars. Near the block center, where temperatures did not exceed 300^{o}C, fracturing

appeared to be a more important mechanism for permeability development than pore enlargement and most of the pore space appeared occluded with evolved tars. At a heating rate of 0.1K/min, little change was observed in the porous structure of bituminous coal. Calculation of the macropore area probability distributions from SEM image analysis revealed a significant change to the original distribution near the heater surface at a 10K/min heating rate. The pore area probability distribution became bimodal with an emerging peak at enlarged pore areas. As pyrolysis progressed, the bimodal pore area probability distribution reverted back toward a broadened single peak due to the observed tar coking.

To better understand the porosity changes observed in large blocks of bituminous coal, porosity changes were characterized in smaller blocks. SEM imaging and pore size analysis showed that the macropore size distribution did not change at a 0.1K/min heating rate over the range of 350 to 600^{o}C. In contrast, pore enlargement by plastic deformation was observed at 10K/min heating rate at temperatures of at least 450^{o}C. The bimodal pore area distribution was seen to occur at 600^{o}C for cores heated at 10K/min in a tube furnace. Pyrolysis of coal cores under complete volumetric confinement was shown to lead to a bimodal macropore area probability distribution at temperatures as low as 450^{o}C with an increased separation between the two peaks at 600^{o}C. The bimodal pore area distribution is characteristic of pyrolysis in bituminous coals that experience a volumetric limitation of swelling in the presented studies.

CO_2 adsorption analysis of the micro- and mesoporous structures shows that nanoscale coal porosity is primarily a function of pyrolysis temperature and heating rate does not have a large effect for the conditions studied. However, CO_2 adsorption did

provide evidence of a retained liquid phase in the pore system of coals heated at 0.1K/min. Very slowly heated coals initially showed higher apparent surface areas and pore volumes after pyrolysis; however, acetone extraction of the chars eliminated any observed differences between coals heated at 10K/min and 0.1K/min. The lack of significant difference in micro- and mesoporous structure between coals heated at 0.1K/min and 10K/min with obvious differences in macroporous structure demonstrate that plastic swelling and deformation occurs at the interface between mesopores and macropores.

Coal devolatilization studies for coal cores showed little difference in total volatile yields between 10K/min and 0.1K/min. Total measured char and volatile yields after 24hrs of pyrolysis showed yields were primarily a function of temperature with only a weak effect caused by heating rate. A more careful analysis of volatile yields over the course of pyrolysis showed that char yields were mainly a function of temperature, but liquid yields were strongly correlated to heating rate. Tar yields were reduced by over 50% at 0.1K/min heating rate over the observed yield at 10K/min. Particle size also had an effect on liquid yields with 75 μm particles yielding larger amounts of tar at a 0.1K/min heating rate compared to 3 mm and 2 cm particles, albeit less than the tar yields at 10K/min, which varied little with particle size. The discrepancy in tar yields is similar to the discrepancy in char yields due to heating rate, adding additional evidence for a tar trapping mechanism at very slow heating rates.

An analysis of Knudsen flow in the mesopores of the coal provides some information about the phenomena driving mass transfer in coals pyrolyzing at very slow heating rates. Coal particles of 2 cm and 3 mm were calculated to have intraparticle

pressure differentials of 1 atm and 0.1 atm, respectively, at 0.1K/min heating rate. The inability to displace tars from the mesopore system in larger particles despite the increased pressure differential suggests that pore plugging is being caused by a complex phenomenon. Intraparticle pressure differentials of up to 100 atm were calculated for 2 cm coal cores heated at 10K/min, offering an estimate of the available pressure to drive plastic deformation.

Impact on UCTT and Subsurface Processing

The work presented in this dissertation impacts the understanding of coal pyrolysis in a subsurface environment in several ways, including:

1) Identifying threshold phenomena at very slow heating rates – macroporosity and tar yields were shown to be strong functions of temperature and heating rate in bituminous coals, with a tipping point for these phenomena occurring between 0.1K/min and 10K/min heating rate. By contrast, mesoporosity and char yield were shown to be weak functions of heating rate but strong functions of temperature. Hence, detailed modeling of a UCTT process would likely need experimental kinetic data to be collected at very slow heating rates to accurately predict product compositions.
2) Identifying the importance of length scales – several observed phenomena were affected by relevant length scales. In block pyrolysis experiments, high heating rates near the heater surface produced increased fracturing away from the heat sources near the block center where the heating rate was slower by an order of magnitude. At slower heating rates, less fracturing was noted. The steepness of the stress gradient caused by thermal expansion of the coal structure was a likely

mechanism for inducing fractures. Likewise, particle size had an effect on the tar yields at very slow heating rates, with larger particles yielding less apparent tars. In general, the large length scales involved in pyrolysis of coal blocks create heat transfer limitations, although the subsequent impact upon mass transfer and devolatilization is varied.

3) Showing possibly enhanced carbon sequestration potential – several experiments provided evidence of a trapped liquid phase in the mesoporous system of bituminous coal chars produced at a very slow heating rate. Prior to extraction of this liquid phase, low-pressure CO_2 adsorption showed a significantly enhanced surface area and total pore volume compared to chars prepared at a higher heating rate. After extraction, little difference was seen in the micro- and mesoporous structure of coal chars, regardless of heating rate. This suggests that the presence of the trapped liquid component enhances the potential for retention of CO_2. Given the very slow heating rates expected in a UCTT process, this result would argue in favor of enhanced CO_2 sequestration capacity for coal seams that had undergone thermal treatment. However, to carry this forward, it will be necessary to understand the long-term fate of trapped tars as a result of their thermal history.

Suggestions for Future Work

Due to the novelty of the UCTT concept, very little work exists in regard to coal pyrolysis at conditions that are truly relevant to subsurface processing. Consequently, a very large amount of work remains to be done to create a comprehensive understanding of the relevant science. Within the narrower context of the work presented in this

dissertation, several experiments would help to clarify key results. The following experiments are recommended for future studies:

1) Permeability studies – heating rate was shown to have a substantial impact on macroporosity and possibly microfracturing in pyrolyzing bituminous coals. It did not have a substantial impact on micro- or mesoporosity. Consequently, gas permeability studies would clarify whether processing conditions produce a substantial impact on the actual capacity for mass transfer in pyrolyzed coals when compared to their native states. Increased hydrostatic pressure and pyrolysis under conditions of radial and axial load would more realistically simulate the actual nature of mass transfer in the subsurface environment.
2) Kinetic studies – although heating rate had only a minor impact on total volatile yields, it had a significant impact on tar yields. More detailed kinetic studies should clarify the inhibited mechanism that hinders tar yields at very slow heating rates. This result is not only relevant to understanding global kinetics under UCTT conditions, but it would also impact the general understanding of tar formation mechanisms and pathways in conventional coal pyrolysis.
3) Tar trapping – the precise mechanism of tar retention in very slowly heated bituminous coal chars is very unclear, although it is certainly a function of heating rate and particle size. Understanding the relevant phenomena is likely complicated by the tar's retention in mesopores where the length scale is measured in nanometers. Experiments on the bench scale would not accurately reflect the properties of the tar within a nanoscale pore. Extraction of the tar may provide some compositional clues as to the chemical nature of the tar and its

apparent ability to resist significant coking at 600^{o}C. However, understanding the dynamics of its evolution and trapping in the pore system would require a more complex experiment. It is proposed that changes in mesoporosity could be observed *in situ* using small angle x-ray scattering from a synchrotron source. If that data were combined with small angle neutron scattering, it might be possible to identify, via differences in the data, a pore size range that might be occluded with tars. The complexity and difficulty of such an experiment would likely require the assistance of a national laboratory to complete.

APPENDIX A

HEAT TRANSFER MODELLING CODES

The codes listed in this appendix were used in MATLAB software to calculate transient temperature profiles for the heating of coal blocks and cores. The results of these calculations are described in Chapter 4.

Block Heating

Main Program

```
%*********************************************************
%****************** 2-D Four Hole Model*******************
%*********************************************************
% This model simulates heat transfer in a 2-D cross-
% section of a coal block that is being heated by
% four embedded cartridge heaters. There is free
% convection on the outer edges and a radiation from a
% ramped heating
% source in the heater holes.
%*********************************************************
clear; clc; close all
delx = 0.0254/8; % node length, meters
```

```
delt = 1;       % iteration time, seconds


Acl = delx^2;

Vnode = delx^3;

 rho = 1545; % coal density, kg/m^3

mC = 0.7171; % Carbon weight percent

mH = 0.0468; % Hydrogen weight percent


Temp = zeros(49,49); % Define Temp matrix

Tempset = zeros(49,49); % Define Tempset matrix

To = 298; % Initial temperature, K

Thmin = 623; % Set heater temperature at the heater ends, K

Theater = zeros(24,1); % Initialize heater temps


% Initialize temperature node


for a = 1:49

   for b= 1:49

      Temp(a,b) = To;

   end

end

for c = 1:285800

   % Set heater ramp
```

```
    if (c < 275000)
        for n = 1:12
            Theater(n) = To + (c/275000)*((Thmin-To)+(150*exp(-0.1*(n-12)^2)));
            Theater(25-n) = Theater(n);
        end
    end
    for e = 2:48
        for d1 = 2:15
            Tempset(d1,e) =
(delt/rho/Cpc(Temp(d1,e))/Vnode)*(Acl*condflux(Temp(d1,e),Temp(d1-
1,e),kc(Temp(d1,e),mC,mH),delx) +
Acl*condflux(Temp(d1,e),Temp(d1+1,e),kc(Temp(d1,e),mC,mH),delx) +
Acl*condflux(Temp(d1,e),Temp(d1,e-1),kc(Temp(d1,e),mC,mH),delx) +
Acl*condflux(Temp(d1,e),Temp(d1,e+1),kc(Temp(d1,e),mC,mH),delx)) + Temp(d1,e);
        end
        for d2 = 19:25
            Tempset(d2,e) =
(delt/rho/Cpc(Temp(d2,e))/Vnode)*(Acl*condflux(Temp(d2,e),Temp(d2-
1,e),kc(Temp(d2,e),mC,mH),delx) +
Acl*condflux(Temp(d2,e),Temp(d2+1,e),kc(Temp(d2,e),mC,mH),delx) +
Acl*condflux(Temp(d2,e),Temp(d2,e-1),kc(Temp(d2,e),mC,mH),delx) +
Acl*condflux(Temp(d2,e),Temp(d2,e+1),kc(Temp(d2,e),mC,mH),delx)) + Temp(d2,e);
        end
```

```
        if (e > 25)
            for d3 = 16:18
                Tempset(d3,e) =
(delt/rho/Cpc(Temp(d3,e))/Vnode)*(Acl*condflux(Temp(d3,e),Temp(d3-
1,e),kc(Temp(d3,e),mC,mH),delx) +
Acl*condflux(Temp(d3,e),Temp(d3+1,e),kc(Temp(d3,e),mC,mH),dingus) +
Acl*condflux(Temp(d3,e),Temp(d3,e-1),kc(Temp(d3,e),mC,mH),delx) +
Acl*condflux(Temp(d3,e),Temp(d3,e+1),kc(Temp(d3,e),mC,mH),delx)) + Temp(d3,e);
            end
        end
    end
    for f = 2:15
        Tempset(f,1) =
(delt/rho/Cpc(Temp(f,1))/(Vnode/2))*(0.5*Acl*condflux(Temp(f,1),Temp(f-
1,1),kc(Temp(f,1),mC,mH),delx) +
0.5*Acl*condflux(Temp(f,1),Temp(f+1,1),kc(Temp(f,1),mC,mH),delx) +
Acl*condflux(Temp(f,1),Temp(f,2),kc(Temp(f,1),mC,mH),delx) +
Acl*convflux(Temp(f,1),To,htop(delx,Temp(f,1)))) + Temp(f,1);
    end
    for g = 19:25
        Tempset(g,1) =
(delt/rho/Cpc(Temp(g,1))/(Vnode/2))*(0.5*Acl*condflux(Temp(g,1),Temp(g-
1,1),kc(Temp(g,1),mC,mH),delx) +
```

```
0.5*Acl*condflux(Temp(g,1),Temp(g+1,1),kc(Temp(g,1),mC,mH),delx) +
Acl*condflux(Temp(g,1),Temp(g,2),kc(Temp(g,1),mC,mH),delx) +
Acl*convflux(Temp(g,1),To,htop(delx,Temp(g,1)))) + Temp(g,1);


   end
    for i = 2:48
      Tempset(1,i) =
(delt/rho/Cpc(Temp(1,i))/(Vnode/2))*(Acl*condflux(Temp(1,i),Temp(2,i),kc(Temp(1,i),
mC,mH),delx) + 0.5*Acl*condflux(Temp(1,i),Temp(1,i-1),kc(Temp(1,i),mC,mH),delx)
+ 0.5*Acl*condflux(Temp(1,i),Temp(1,i+1),kc(Temp(1,i),mC,mH),delx) +
Acl*convflux(Temp(1,i),To,hvert(delx,Temp(1,i)))) + Temp(1,i);
   end
   for j = 2:25
      Tempset(j,49) =
(delt/rho/Cpc(Temp(j,49))/(Vnode/2))*(0.5*Acl*condflux(Temp(j,49),Temp(j-
1,49),kc(Temp(j,49),mC,mH),delx) +
0.5*Acl*condflux(Temp(j,49),Temp(j+1,49),kc(Temp(j,49),mC,mH),delx) +
Acl*condflux(Temp(j,49),Temp(j,48),kc(Temp(j,49),mC,mH),delx)) + Temp(j,49);
   end
   for k = 2:24
      Tempset(16,k) =
(delt/rho/Cpc(Temp(16,k))/(Vnode/2))*(Acl*condflux(Temp(16,k),Temp(15,k),kc(Temp
(16,k),mC,mH),delx) + 0.5*Acl*condflux(Temp(16,k),Temp(16,k-
```

```
1),kc(Temp(16,k),mC,mH),delx) +
0.5*Acl*condflux(Temp(16,k),Temp(16,k+1),kc(Temp(16,k),mC,mH),delx) +
Acl*radflux(Temp(16,k),Theater(k))) + Temp(16,k);
      Tempset(18,k) =
(delt/rho/Cpc(Temp(18,k))/(Vnode/2))*(Acl*condflux(Temp(18,k),Temp(19,k),kc(Temp
(18,k),mC,mH),delx) + 0.5*Acl*condflux(Temp(18,k),Temp(18,k-
1),kc(Temp(18,k),mC,mH),delx) +
0.5*Acl*condflux(Temp(18,k),Temp(18,k+1),kc(Temp(18,k),mC,mH),delx) +
Acl*radflux(Temp(18,k),Theater(k))) + Temp(18,k);
   end

   Tempset(1,1) =
(delt/rho/Cpc(Temp(1,1))/(Vnode/4))*(0.5*Acl*condflux(Temp(1,1),Temp(2,1),kc(Temp
(1,1),mC,mH),delx) +
0.5*Acl*condflux(Temp(1,1),Temp(1,2),kc(Temp(1,1),mC,mH),delx) +
0.5*Acl*convflux(Temp(1,1),To,hvert(delx,Temp(1,1))) +
0.5*Acl*convflux(Temp(1,1),To,htop(delx,Temp(1,1)))) + Temp(1,1);
   Tempset(16,1) =
(delt/rho/Cpc(Temp(16,1))/(Vnode/4))*(0.5*Acl*condflux(Temp(16,1),Temp(15,1),kc(T
emp(16,1),mC,mH),delx) +
0.5*Acl*condflux(Temp(16,1),Temp(16,2),kc(Temp(16,1),mC,mH),delx) +
0.5*Acl*convflux(Temp(16,1),To,hvert(delx,Temp(16,1))) +
0.5*Acl*convflux(Temp(16,1),To,htop(delx,Temp(16,1)))) + Temp(16,1);
```

```
   Tempset(18,1) =
(delt/rho/Cpc(Temp(18,1))/(Vnode/4))*(0.5*Acl*condflux(Temp(18,1),Temp(19,1),kc(T
emp(18,1),mC,mH),delx) +
0.5*Acl*condflux(Temp(18,1),Temp(18,2),kc(Temp(18,1),mC,mH),delx) +
0.5*Acl*convflux(Temp(18,1),To,hvert(delx,Temp(18,1))) +
0.5*Acl*convflux(Temp(18,1),To,htop(delx,Temp(18,1)))) + Temp(18,1);
   Tempset(1,49) =
(delt/rho/Cpc(Temp(1,49))/(Vnode/4))*(0.5*Acl*condflux(Temp(1,49),Temp(2,49),kc(T
emp(1,49),mC,mH),delx) +
0.5*Acl*condflux(Temp(1,49),Temp(1,48),kc(Temp(1,49),mC,mH),delx) +
0.5*Acl*convflux(Temp(1,49),To,hvert(delx,Temp(1,49)))) + Temp(1,49);

   Tempset(16,25) =
(delt/rho/Cpc(Temp(16,25))/(0.75*Vnode))*(Acl*glarbus(Temp(16,25),Temp(15,25),kc(
Temp(16,25),mC,mH),delx) +
0.5*Acl*condflux(Temp(16,25),Temp(17,25),kc(Temp(16,25),mC,mH),delx) +
0.5*Acl*condflux(Temp(16,25),Temp(16,24),kc(Temp(16,25),mC,mH),delx) +
Acl*condflux(Temp(16,25),Temp(16,26),kc(Temp(16,25),mC,mH),delx) +
Acl*radflux(Temp(16,25),Theater(24))) + Temp(16,25);
   Tempset(18,25) =
(delt/rho/Cpc(Temp(18,25))/(0.75*Vnode))*(Acl*condflux(Temp(18,25),Temp(19,25),k
c(Temp(18,25),mC,mH),delx) +
0.5*Acl*condflux(Temp(18,25),Temp(17,25),kc(Temp(18,25),mC,mH),delx) +
```

```
0.5*Acl*condflux(Temp(18,25),Temp(18,24),kc(Temp(18,25),mC,mH),delx) +
Acl*condflux(Temp(18,25),Temp(18,26),kc(Temp(18,25),mC,mH),delx) +
Acl*radflux(Temp(18,25),Theater(24))) + Temp(18,25);
   Tempset(17,25) =
(delt/rho/Cpc(Temp(17,25))/(0.75*Vnode))*(0.5*Acl*condflux(Temp(17,25),Temp(16,2
5),kc(Temp(17,25),mC,mH),delx) +
0.5*Acl*condflux(Temp(17,25),Temp(18,25),kc(Temp(17,25),mC,mH),delx) +
Acl*condflux(Temp(17,25),Temp(17,26),kc(Temp(17,25),mC,mH),delx) +
Acl*radflux(Temp(17,25),Theater(24))) + Temp(17,25);

   for l = 1:25
      for m = 1:49
         Tempset(50-l,m) = Tempset(l,m);
      end
   end
   Temp = Tempset;
   if (c==275750)
      Temp
   end
end
```

Coal Thermal Property Functions

```
function Cpc = Cpc(Tnode)
Cpc = 500.06 + 0.829*Tnode;
```

```
function kc = kc(Tnode, mC, mH)
kinv = (mC/1.47) + (mH/0.0118)*sqrt(273.15/Tnode);
 kc = 1/kinv;
```

Heat Transfer Coefficient Functions

```
function htop = htop(L, Tnode)
Pr = 0.69;
k = 33.8e-3;
 htop = 0.15*k*(RN(Tnode, L)^(1/3))/L;

function hvert = hvert(L, Tnode)
Pr = 0.69;
k = 33.8e-3;
hvert = (k/L)*(0.68 + 0.670*(RN(Tnode, L)^0.25)/(1+(0.492/Pr)^(9/16))^(4/9));

function RN = RN(Tnode, L)
 g = 9.81;
beta = 0.0025;
Tinf = 293;
nu = 26.4e-6;
alpha = 38.3e-6;
 RN = g*beta*(Tnode - Tinf)*(L^3)/nu/alpha;
```

Core Heating

Main Program

```
%*********************************************************

%******************** Coal Core Model **********************

%

% The purpose of this model is to estimate the

% temperature profile in a heating core of bituminous coal

% similar to those used in my core experiments.

%

%*********************************************************

clear; clc; close all

 % Define repeatedly used constants

 diam = 0.75;              % core diameter, in

delr = diam*0.0254/2/10;   % grid size, m

delt = 0.1;               % time step, s

eps = 0.5;               % emissivity

sigma = 5.67e-8;          % Stefan-Boltzmann constant, Wm-2K-4

rho = 1545;               % coal density, kg/m3

ramprate = 0.1/60;            % temperature ramp, degrees C/s

alphaa = 8.418e-7; % Initialize temperature matrix to 298K


Temp = zeros(80,20);

Tempnew = zeros(80,20);
```

```
Tro = 298;
 for a = 1:20
    for b = 1:80
        Temp(b,a) = 298;
    end
end

% Build radius vector to determine radial distances
 rad = zeros(1,11);
for c = 1:11
    rad(c) = 10*delr-(c-1)*delr;
end

% Calculate temperatures in the core
Tr = 298;

for g = 1:100000
    if (Tr < 873)
        Tr = Tro + g*delt*ramprate;
    else
        Tr = 873;
    end
```

```
for d = 2:40
   for e = 2:9
      Tempnew(d,e) = (2*alphac(Temp(d,e))*delt)*(Temp(d,e-1)-
Temp(d,e))/(2*rad(e+1)*delr+delr^2) +
(2*rad(e+1)*alphac(Temp(d,e))*delt)*(Temp(d,e+1)-Temp(d,e))/(2*rad(e+1)*delr +
delr^2)/delr + (alphac(Temp(d,e))*delt/delr^2)*(Temp(d+1,e)+Temp(d-1,e)-
2*Temp(d,e)) + Temp(d,e);
   end

   Tempnew(d,1) = (2*rad(1)*eps*sigma*delt)*(Tr^4 - Temp(d,1)^4)/((2*rad(1)*delr -
delr^2)*rho*(500.06+0.829*Temp(d,1))) + (2*(rad(1)-delr)*alphaa*delt)*(Temp(d,2)-
Temp(d,1))/(2*rad(1)*delr - delr^2)/delr + (alphaa*delt/delr^2)*(Temp(d-
1,1)+Temp(d+1,1)-2*Temp(d,1)) + Temp(d,1);
   Tempnew(d,10) = (2*alphac(Temp(d,10))*delt)*(Temp(d,9)-Temp(d,10))/delr^2 +
(alphac(Temp(d,10))*delt/delr^2)*(Temp(d-1,10)+Temp(d+1,10)-2*Temp(d,10)) +
Temp(d,10);
end

for f = 2:9
   Tempnew(1,f) = (0.25*eps*sigma*delt)*(Tr^4 -
Temp(1,f)^4)/(delr*rho*(500.06+0.829*Temp(1,f))) + (alphaa*delt/delr^2)*(Temp(2,f)-
Temp(1,f)) + (2*alphaa*(rad(f+1)+delr)*delt)*(Temp(1,f-1)-
```

```
Temp(1,f))/((2*rad(f+1)*delr-delr^2)*delr) + (2*alphaa*rad(f+1)*delt)*(Temp(1,f+1)-
Temp(1,f))/((2*rad(f+1)*delr+delr^2)*delr) + Temp(1,f);
end
 Tempnew(1,1) = (2.5*rad(1)*delr - delr^2)*eps*sigma*delt*(Tr^4 -
Temp(1,1)^4)/((2*rad(1)*delr - delr^2)*delr*rho*(500.06+0.829*Temp(1,1))) +
(2*(rad(1)-delr)*alphaa*delt)*(Temp(1,2)-Temp(1,1))/((2*rad(1)*delr-delr^2)*delr) +
(alphaa*delt/delr^2)*(Temp(2,1)-Temp(1,1)) + Temp(1,1);
Tempnew(1,10) = (0.25*eps*sigma*delt)*(Tr^4 -
Temp(1,10)^4)/(delr*rho*(500.06+0.829*Temp(1,10))) +
(alphaa*delt/delr^2)*(Temp(2,10)-Temp(1,10)) + (2*alphaa*delt/delr^2)*(Temp(1,9)-
Temp(1,10)) + Temp(1,10);

for h = 1:10
   for i = 1:40
      Tempnew(i,20-h+1) = Tempnew(i,h);
   end
end
 for j = 1:20
   for i = 1:40
      Tempnew(80-i+1,j) = Tempnew(i,j);
   end
end
 Temp = Tempnew;
```

End

Thermal Diffusivity Function

```
% This function calculates the thermal diffusivity of the
% coal for a user-input temperature, based upon the density,
% heat capacity and thermal conductivity of a bituminous
% coal
 function alphac = alphac(Temp)
 rho = 1545;    % coal density, kg/m^3
mC = 0.7171;   % Carbon weight percent
mH = 0.0468;   % Hydrogen weight percent
 Cp = 500.06 + 0.829*Temp;  % heat capacity, J/kgK-1
 kinv = (mC/1.47) + (mH/0.0118)*sqrt(273.15/Temp);
k = 1/kinv;    % thermal conductivity, Wm-1K-1
 alphac = k/rho/Cp; % thermal diffusivity, m2/s
```

APPENDIX B

EXPERIMENTAL VARIABILITY AND ERROR

As with most coal research, the complex and heterogeneous nature of the substrate makes error analysis and the interpretation of experimental results more difficult. The purpose of this appendix is to provide a mixture of qualitative and quantitative observations of experimental variability and error to better understand the limits of the conclusions that can be drawn from the work presented in this dissertation. This appendix contains observations of coal variability and a discussion of how error and variability were accounted for in the reported error bars shown in most figures.

Observations of Coal Variability

This section will discuss observations of the physical coal characteristics and explore whether these characteristics had any reproducible impacts on the reported data.

Coal Physical Characteristics

By virtue of working in large particles and blocks, the heterogeneity of coal assumes a larger role in understanding experimental outcomes. Coal pyrolysis has traditionally been studied using powdered coals with a well-characterized particle size distribution to ensure that local variations in chemical structure, ash composition, etc. become averaged out in the quantitative measurements made upon them. Large coal particles, such as the cores used in many of the experiments presented in this dissertation,

cannot be made homogeneous because their size necessitates crossing stratigraphic layers in the coal body. Even a 2" core may represent several tens of thousands of years of evolving depositional environment and organic sources.

The possibility for heterogeneity impacting experimental outcomes is made obvious in Table 3.1. The three observed blocks, although chosen randomly, likely represent nearly the full range of possible variability in composition for a Utah high-volatile bituminous coal. It should be noted that these blocks each came from fresh mine cuttings, meaning this high level of variability existed within a very confined region of the coal seam. Further, samples sent for elemental analysis were pulverized from larger pieces to ensure that measurements were representative of the average composition of each particular block.

Sample preparation also suggested the high degree of compositional variability in the coal samples. Blocks prepared by cutting with a concrete saw showed a surprising degree of structural integrity, even when they were heavily cleated. However, failure appeared to occur more often in blocks with larger bright bands, suggesting that such layers were weaker than dull bands. Core preparation proved even more dependent upon coal composition. Cores were most likely to fail at cleats or bright bands, limiting the core length that could be isolated at certain areas of a given block. Many cores were seen to fail where no structural weakness could be detected, suggesting possible failures propagating through systems of microcleats. High mineral content also seemed to increase the likelihood of core breakage, with coal 3 being the most difficult coal sample from which to isolate cores.

Experimental Behavior

These observations of coal behavior during cutting carry implications for the performed experiments. In blocks, the tendency to hold together despite heavy cleating may have created nonuniform heat transfer conditions between blocks. Cleats were likely pathways for volatile release, allowing heat to be convectively removed from the block. It can be reasonably argued that more heavily-fractured blocks were less conducive to efficient heat transfer, resulting in lower internal temperatures. Likewise, the inability to isolate cores from cleated or high-mineral regions of the block may have biased those experiments toward the behavior of dull coal bands.

An examination of the experimental data derived from the coal samples listed in Table 3.1 shows correlation to some of the reported trends, but not all. For example, coal 2 consistently yields the largest amount of volatile matter (as shown in Table 6.1) as would be expected from its proximate analysis. However, coal 1 does not consistently yield more mass for a given condition despite having a higher measured volatile content (including water) than coal 3. The higher variability in yield for coals 1 and 3 may owe to their higher mineral contents if inclusions are not distributed consistently in each core.

The porosity data present a more complicated picture of the impact of coal composition on the experimental outcome. Figure B.1 shows macropore area probability distributions for all three coals at a pyrolysis temperature of 450^{o}C at 0.1K/min heating rate. Figure B.2 shows the probability distributions at the same temperature and 10K/min heating rate. At the slower heating rate, the pore size distributions are quite alike with only coal 3 showing a slight increase in larger pores. However, at 10K/min heating rate, each coal produces a distinctly different pore size distribution with coal 1 representing

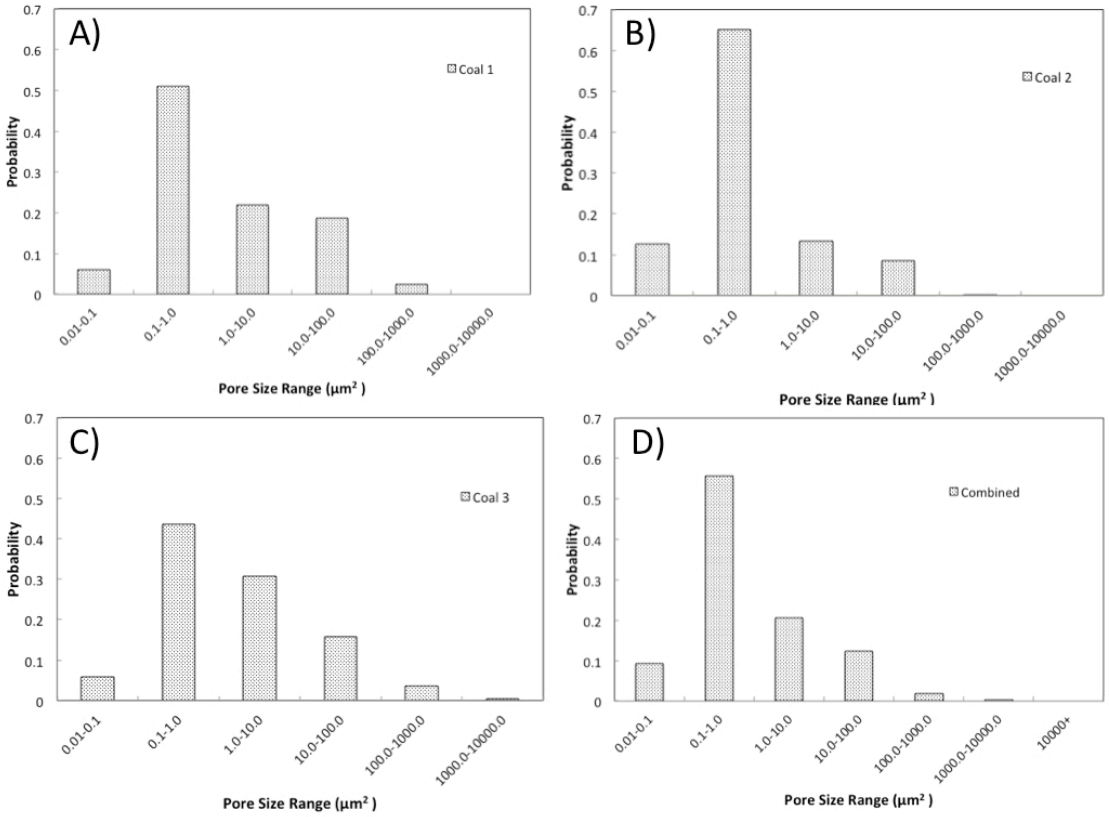

Figure B. 1 Pore area probability distributions for pyrolysis to 450°C at 0.1K/min heating rate. A) Coal 1 B) Coal 2 C) Coal 3 D) Combined

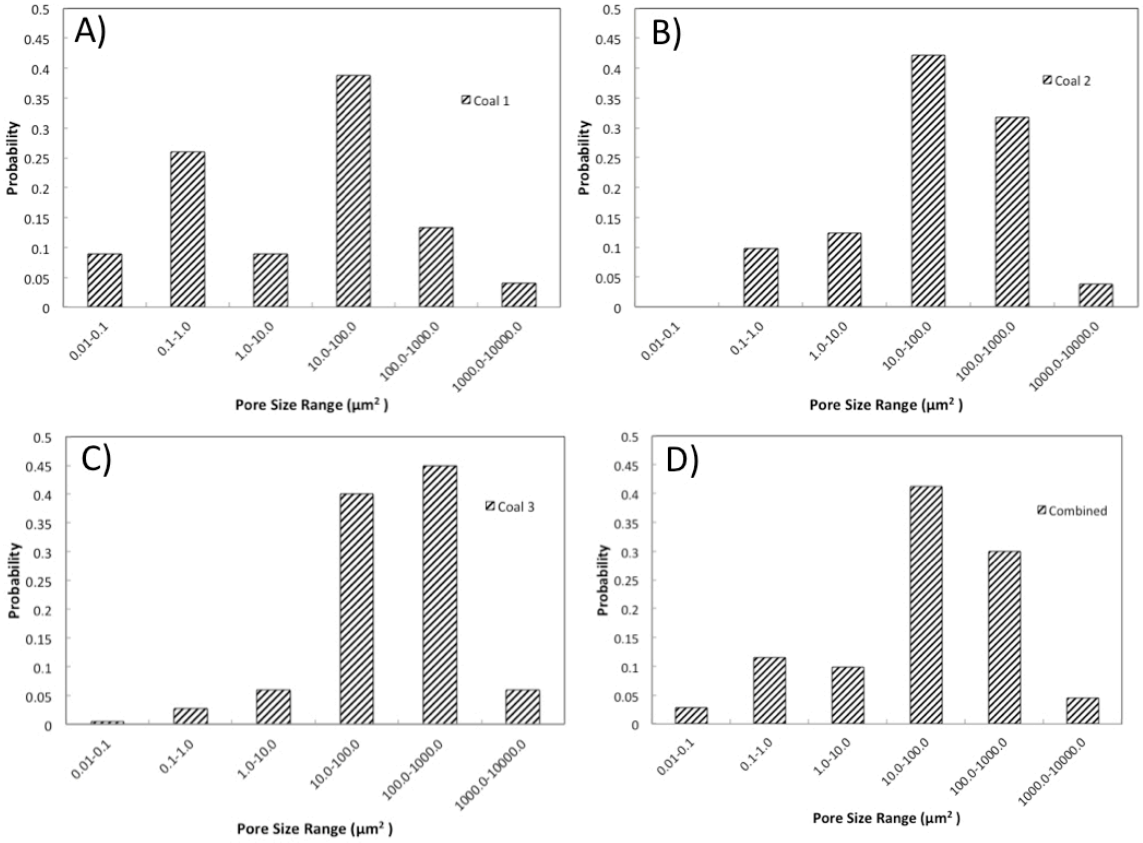

Figure B. 2 Pore area probability distributions for pyrolysis to 450°C at 10K/min heating rate. A) Coal 1 B) Coal 2 C) Coal 3 D) Combined

the biggest outlier. Again, this behavior does not directly correlate to the chemical compositions of each coal.

The lack of consistency in trends extends to the BET data measured on each coal sample reported in Table 6.1. Figure B.3 shows measured surface areas before acetone extraction for each coal as a function of temperature for 10K/min (B.3a) and 0.1Kmin (B.3b) heating rates. Under these circumstances, coals 2 and 3 have a somewhat uniform difference in behavior consistent with the increased amount of volatiles released from coal 2. However, coal 1 behaves nearly identical to coal 3 at 10K/min and to coal 1 at 0.1K/min. Figure B.4 shows the same data after acetone extraction. In this situation, the behavior of samples is now more consistent, with coal 1 falling between coals 2 and 3. In summary, before acetone extraction, there is only a weak correlation of surface area to the coals' proximate analyses, but after extraction, the surface area trends are quite consistent with the known trend in measured volatiles.

From the gathered data, a few conclusions can be drawn regarding the impact of coal variability on experimental outcomes, including:

1) It is best to present the data by averaging over all 3 coals because typically one coal in each experiment has acted as an outlier while the other two have acted uniformly. Averaging pulls in some variability while not allowing it to skew the data too much toward the outlying case.
2) It is impossible to simply correlate any proximate characteristic of a given coal to the expected outcome of an experiment. Variability in measured data may be correlated to the chemical composition of a given coal or it may be due to variability within each block. It is impossible to discern which case is true.

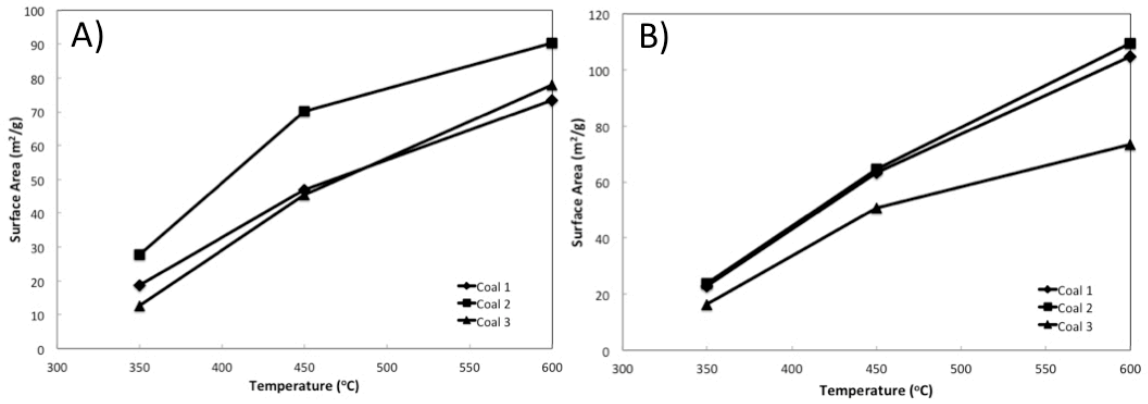

Figure B. 3 Surface area measurements for each coal before extraction at A) 10K/min and B) 0.1K/min.

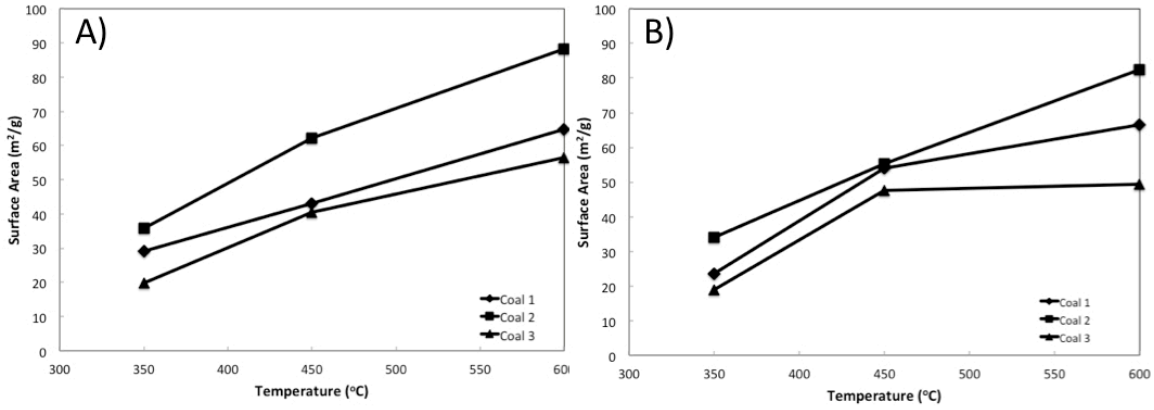

Figure B. 4 Surface area measurements for each coal after acetone extraction at A) 10K/min and B) 0.1K/min.

3) Although variability is high between different coal samples, the numerous differences in behavior observed between 10K/min and 0.1K/min heating rates are consistent enough to lend confidence that coal pyrolysis behavior does correlate to heating rate in spite of possible chemical variability.

Error and Variability Analysis

In the presentation of experimental data, it was necessary to present estimates of uncertainty for most experiments in order to identify what phenomena varied by experimental parameters. The purpose of this section is to highlight potential sources of experimental error and describe how uncertainty was measured for the various types of experiments presented in the body of the dissertation.

Sources of Error

Experimental error is generally thought to be smaller than the sample-to-sample variability of the selected bituminous coal. This has guided the decision to generally focus on sample variability when calculating the experimental uncertainty. Table B.1 gives a brief accounting of the expected primary and secondary sources of error for the major types of experiments described in this work.

Block experiments are believed to have been most prone to error due to certain difficulties in working with large blocks. Samples removed for SEM analysis were typically taken from adjacent to the heater borehole and the center thermocouple. However, heater and thermocouple placement may have varied by up to 10% due to the difficulties of precise drilling on a surface with nonuniform hardness. Given the Gaussian temperature profile of the embedded heaters, temperature gradients were quite steep

Table B. 1 Error sources for presented experiments

Type	Experiment	Primary Error	Secondary Error
Block	SEM Analysis	Sample collection	Pore measurement
Core	SEM Analysis	Pore measurement	Pore identification
Core	Char/Tar Yields	Drying losses	Transfer losses
Core	CO_2 Adsorption	Weighing error	Regression error

in the block. Thus, so much as a 5mm offset in sampling location could lead to obtaining material pyrolyzed at a much lower temperature.

SEM image analyses for both block and core experiments were prone to measurement error, although efforts were made to minimize this. Pore size distributions were calculated and reported on a logarithmic scale, creating broad pore size categories. Doing so substantially reduced the number of pores that were likely to be poorly sized. SEM analysis was also complicated by image interpretation, especially at small pore sizes or images with many pores. At high magnification, it was difficult to ascertain whether certain small structures (< 100 nm) were actual pores or simply shallow depressions on the sample surface. In images with large numbers of pores, complicated and often three-dimensional pore shapes made it occasionally difficult to determine whether two pores were unique or joined. Unfortunately, there is no way to truly know the amount of error created by these analysis issues. For this reason, the entirety of the SEM analysis was done by the author to ensure that the measurement error was consistent across all experiments.

Core experiments were not prone to much measurement error due to the use of a high-precision scale, but the measurement of liquid yields may have had significant error. Liquid collection was generally observed to be efficient although experiments at higher temperatures may have increased the likelihood of liquids escaping to the bubbler system. A bigger concern was weighing after collection. To expedite data collection, liquid samples were evaporated from the acetone solvent in an oven at 70^{o}C. The elevated drying temperature increases the likelihood that lighter oils were lost in this step. Consequently, liquid yields are reported as tar yields since the higher molecular weight

species are the most likely to have been measured. It is expected that the tar yield is a good proxy for the total liquid yield.

BET measurements were prone to measurement errors due to the small sample sizes used for gas adsorption. With samples on the order of hundreds of milligrams, the weighing error was likely 1-2%. This is still not believed to be a major source of error. Additionally, adsorption data techniques rely upon regression methods to extract useful information. A sampling of BET data suggests that these regressions had uncertainties in the range of 2-3%.

Estimation of Uncertainty

The following section is intended to explain how uncertainty estimates were created for the various experiments performed in the presented work. Uncertainty was considered to be a combination of quantifiable error plus observed variability of coal samples.

SEM imaging. The greatest potential source of uncertainty in determining macropore size distributions from SEM images was measurement error. Images analyzed digitally were subject to measurement errors of 2 pixels and those analyzed manually were subject to errors of 0.25mm. The impact of these errors was on the order of a 10% change in the pore area estimate at very small sizes. The uncertainty became much less at larger pore sizes.

To estimate the uncertainty, pore size data were carefully sorted at two critical categories: 0.1 μm^2, the smallest category, and 10 μm^2, the pore size category that was used to weight data between 800x and 5000x magnification sets. For both thresholds, counts were made of all pores within a set interval ($\pm$10% at 0.1 μm^2 and $\pm$1% at 10 μm^2).

A conservative estimate was made that half of the pores meeting these criteria were erroneously miscategorized. Consequently, uncertainties for these pore size categories were estimated as half of the sum of pores within the interval divided by the total number of pores within the size categories above and below the threshold. In general, the uncertainty was typically 5-15% with the higher uncertainties commonly seen in samples with fewer observed pores. To complete the uncertainty estimate, a standard 5% uncertainty was added to all estimates to account for missed pores.

Core char and tar yields. Uncertainties in char and tar yields from core experiments were considered to derive mainly from sample variability due to the accuracy of weighing equipment (weight to tenths of milligrams for multigram samples). Measurements were considered especially accurate for char samples that were rapidly quenched into a preweighted jar then capped, assuring that any subsequently released volatiles would still be accounted for in the final weight measurement. Consequently, the sample variability (ranging from 0.3 to 3.1%) was reported as the uncertainty for these experiments.

Uncertainties for tar yields were more complicated due to the potential for transfer losses and drying losses, and sample sizes on the order of tens to hundreds of milligrams. Replicate data on certain samples suggest that sample variability had a large range with some conditions only giving 7% variation in yield and others giving 21%, but even these data still comingle uncertainty from error and variability. It is estimated that measurement error could be as high as 10% for tar yields, and possibly higher for very small tar yields. Given the lack of information on the actual error in the measurement, the uncertainties for tar yields were reported as the measured sample variability.

Adsorption data. Measurements made via CO_2 adsorption were reported with mixed confidence. BET surface area measurements were reported by the analytical software with a calculated confidence interval. In general, the expected error of the data regression was only 2-3% of the measurement, so the larger sample variability was consistently reported as the uncertainty in BET measurements. Data from BJH adsorption analysis were not reported with an uncertainty. Given the difficult nonlinear curve-fitting algorithm necessary to BJH analysis, it is expected that uncertainty is higher in these data. Uncertainties for BJH-derived data were reported as sample variability; however, given the lack of concrete information on analysis error, the slimmest possible conclusions were construed from this data set.

APPENDIX C

DESCRIPTION OF KNUDSEN ANALYSIS CALCULATIONS

The purpose of this appendix is to explicitly detail how experimental data were utilized to calculate the pressure drop due to Knudsen flow according to the analysis described in Chapter 6. This should offer a full accounting of the assumptions and methods that were used in the presented analysis. The calculations presented below are for a 2cm core heated at 0.1K/min.

BJH Data Analysis

BJH data were used to estimate the amount of cross-sectional area for mass transfer at particular pore sizes as a function of temperature. Due to a lack of available information, pores were assumed to be cylindrical in shape (consistent with BJH theory) and have a uniform length that was five times the diameter. This assumption was used to convert the incremental pore volumes calculated for various pore diameters into incremental cross-sectional areas. It was necessary to know the cross-sectional areas for a range of pore sizes because the data showed that available cross-sectional area decreased as pore size increased, indicating a possible bottleneck for mass transfer. The Knudsen flow calculations were performed at various pore sizes to determine how such a bottleneck might affect the estimated pressured drop. An example of the cross-sectional area calculation for a sample heated to $300^{o}C$ at 0.1K/min is shown in Table C.1. This

Table C. 1 Cross-sectional areas for slowly-heated coal at 300°C

Radius (m)	Incremental Pore Volume (cm^3/g)	Incremental Pore Cross-Section (m^2/g)
2.31E-08	3.27E-04	1.42E-03
1.77E-08	2.06E-04	1.16E-03
1.58E-08	2.88E-04	1.82E-03
1.44E-08	2.05E-04	1.43E-03
1.28E-08	2.45E-04	1.91E-03
1.14E-08	2.58E-04	2.27E-03
1.00E-08	3.22E-04	3.22E-03
8.77E-09	3.18E-04	3.63E-03
7.74E-09	3.75E-04	4.84E-03
6.85E-09	5.06E-04	7.39E-03
6.09E-09	4.56E-04	7.49E-03
5.42E-09	5.67E-04	1.05E-02
4.78E-09	7.72E-04	1.61E-02
4.19E-09	8.28E-04	1.97E-02
3.64E-09	1.12E-03	3.07E-02
3.12E-09	1.43E-03	4.57E-02
2.69E-09	1.48E-03	5.51E-02
2.35E-09	1.67E-03	7.09E-02
2.08E-09	1.92E-03	9.23E-02
1.85E-09	1.87E-03	1.01E-01
1.65E-09	2.18E-03	1.32E-01
1.49E-09	2.56E-03	1.72E-01
1.34E-09	2.78E-03	2.08E-01
1.20E-09	3.40E-03	2.83E-01
1.08E-09	3.46E-03	3.21E-01
1.00E-09	1.61E-03	1.61E-01
9.56E-10	1.88E-03	1.97E-01
9.08E-10	2.24E-03	2.47E-01

calculation was repeated over a temperature range of 300 to 600°C to determine the changes in available area for mass transfer.

Volatile Molecular Weight Calculations

Average volatile molecular weights were calculated using liquid and gas yield data as a function of temperature. It was assumed that liquids had an average molecular weight of 150 g/mol and light gases had an average molecular weight of 17.1 g/mol based upon a 3:3:2:2 molar ratio of $CO/H_2/CO_2/H_2O$, respectively. Liquid and gas yields were converted to an approximate molecular weight as follows:

$$\overline{MW} = \frac{m_{gas}+m_{liq}}{\frac{m_{gas}}{17.1 g/mol}+\frac{m_{liq}}{150 g/mol}} \quad (1)$$

Calculated values for the volatile molecular weight for 2cm coal particles are shown in Table C.2.

TGA Data Analysis

TGA data were used to estimate the mass flux emitted from coal particles as a function of temperature. It was assumed that since little difference in devolatilization rate was seen over a broad range of particle sizes at a given heating rate, these TGA data could be used for all particle sizes once standardized to a uniform weight basis (in this case, per 1 kg). The mass flux was calculated as the incremental mass loss divided by the time interval and the cross-sectional area for mass transfer. The cross-sectional areas were calculated as described above. Table C.3 shows some TGA data scaled to 1 kg and

Table C. 2 Average volatile molecular weight calculations

Temperature (^oC)	Liquid Yield (g/g coal)	Gas Yield (g/g coal)	Avg Moles	Avg. Mol. Wt. ($g\ mol^{-1}$)
300	1.23E-03	5.78E-02	3.39E-03	17.4
400	2.91E-02	1.76E-01	1.05E-02	19.6
500	2.62E-02	2.58E-01	1.52E-02	18.6
600	4.75E-02	3.11E-01	1.85E-02	19.4

Table C. 3 Mass flux calculations from TGA data

Time (min)	Temperature (^oC)	Mass (kg)	Mass Loss ($kg\ s^{-1}$)	Area (m^2)	Mass Flux ($kg\ m^{-2}\ s^{-1}$)
2005.5	300.0	1.00000			
2006.5	300.2	0.99996	6.448E-07	1.046E-02	6.163E-05
3113.5	400.0	0.87779			
3114.5	400.1	0.87765	2.403E-06	1.052E-02	2.285E-04
4222.5	500.0	0.76816			
4223.5	500.2	0.76807	1.465E-06	1.708E-03	8.581E-04

the calculated mass flux values for a coal particle assuming an average pore diameter of 10 nm.

Knudsen Flow Calculations

Calculations for average pressure gradients were performed according to the equations outlined in Chapter 6. Table C.4 shows values for the Knudsen and slip flow terms, the pressure gradient and the important parameters used to calculate these terms. Once pressure gradients were calculated over all temperature for which mass flux data were available, the maximum value for the pressure gradient was isolated from the data. To find the absolute pressure differential in a 2 cm coal particle, the pressure gradient was then multiplied by 0.01m (assumed to be an approximate distance for mass transfer from the center of a particle). Table C.5 lists maximum pressure gradients and calculated pressure differentials for various assumed pore sizes.

Table C. 4 Calculation of pressure gradients for 2 cm coal particle

Temperature (^oC)	Pore Radius (m)	Area (m^2)	Mol. Wt. ($g\ mol^{-1}$)	Avg. Density ($kg\ m^{-3}$)	Viscosity (Pa s)	Mass Flux ($kg\ m^{-2}\ s^{-1}$)	F	Knud Term	SF Term	Pres. Grad. ($atm\ m^{-1}$)
300	1.08E-08	1.05E-02	17.42	0.74	2.65E-05	6.16E-05	96.06	2.20E-11	3.94E-11	9.91
400	1.08E-08	1.05E-02	19.56	0.71	3.01E-05	2.37E-04	111.34	2.15E-11	3.84E-11	39.13
500	1.09E-08	9.47E-03	18.62	0.59	3.34E-05	1.44E-04	134.91	1.97E-11	3.50E-11	25.92
600	1.12E-08	1.19E-02	19.38	0.54	3.64E-05	1.01E-04	148.95	1.94E-11	3.45E-11	18.51

Table C. 5 Pressure differentials for 2 cm coal particle

Pore Size (nm)	Pres. Grad (atm m-1)	Pres. Diff. (atm)
2.8	15.62	0.16
10	91.48	0.91
50	117.60	1.18

REFERENCES

Anthony, D.B.; Howard, J.B. Pyrolysis of Bituminous Coal Powders Under Caustic Conditions. *AIChE J*., **1976**, 22, 625-638.

Berkowitz N. *The Chemistry of Coal*; Elsevier, New York, 1985.

Bourgoyne, A.T; Milheim, K.K.; Chenevert, M.E.; Young, F.S. *Applied Drilling Engineering*; Society of Petroleum Engineers, Dallas, 1986.

Brown, G.P.; Dinardo, A.; Cheng, G.K.; Sherwood, T.K. The Flow of Gases in Pipes at Low Pressures. *J. App. Physics*, **1946**, 17, 802-813.

Burnham, A. *Slow Radio-Frequency Processing of Large Oil Shale Volumes to Produce Petroleum-like Shale Oil;* UCRL-ID-155045; LLNL: Livermore, CA, 2003.

Burton, E.; Friedmann, J.; Upadhye, R. *Best Practices in Underground Coal Gasification*; W-7405-Eng-48; LLNL: Livermore, CA, 2006.

Close, J.C. Natural fractures in coal. In *Hydrocarbons from Coal;* Brule, S., Ed.; American Association of Petroleum Geologists: Tulsa, 1993; 119–132.

Connell, L.D.; Lu, M.; Pan, Z.; An Analytical Coal Permeability Model for Tri-axial Strain and Stress Conditions. *Int. J. Coal Geo*., **2010,** 84, 103–114.

Crawford, P.; Killen, J. New Challenges and Directions in Oil Shale Development Technologies. In *Oil Shale: A Solution to the Liquid Fuel Dilemma*; American Chemical Society: New York, 2010; 21-60.

Cui, X.; Bustin, R.M. Volumetric Strain Associated with Methane Desorption and its Impact on Coalbed Gas Production from Deep Coal Seams. *AAPG Bulletin*, **2005**, 89, 1181–1202.

Dryden, I. Chemistry of Coal and Its Relation to Coal Carbonization. *J. Inst. Fuel*, **1957**, 30, 193-221.

Eddinger R.; Friedman L.; Rau E. Devolatilization of Coal in a Transport Reactor. *Fuel* **1966**, 45, 245–52.

Gamson, P.; Beamish, B.; Johnson, D. Coal Microstructure and Micropermeability and

Their Effects on Natural Gas Recovery. *Fuel*, **1993**, 72, 87-99.

Gavalas, G.R.; Wilks, K.A. Temperature Effects During Pyrolysis of Coal Maceral Surrogates. *AIChE J.,* **1980**, 26, 201-215.

Gentzis, T. Stability Analysis of a Horizontal Coalbed Methane Well in the Rocky Mountain Front Ranges of Southeast British Columbia, Canada. *Int. J. Coal Geo*., **2009a**, 77, 328–337.

Gentzis, T.; Deisman, N.; Chalaturnyk, R.J. Effect of Drilling Fluids on Coal Permeability: Impact on Horizontal Wellbore Stability. *Int. J. Coal Geo*., **2009b**, 78, 177–191.

Gentzis, T.; Deisman, N.; Chalaturnyk, R.J. A Method to Predict Geomechanical Properties and Model Well Stability in Horizontal Boreholes. *Int. J. Coal Geo*., **2009c**, 78, 149–160.

Gibbins, J.; Kandiyoti, R. Global Mechanism of Coal Pyrolysis for a Transport-Limited Bituminous Coal. *Fuel*, **1989**, 68, 895-918.

Green, M. B. *Underground Coal Gasification**:** A Joint European Trial in Spain*; DTI Pub URN99/1093; DTI: London, 1999.

Han, J.-Z.; Sang, S.-X.; Cheng, Z.-Z.; Huang, H.-Z. Exploitation Technology of Pressure Relief Coalbed Methane in Vertical Wells in the Huainan Coal Mining Area. *Mining Science and Technology*, **2009**, 19, 25–30.

Hill, R. W. In *Review of the CRIP Process*, Proceedings of the 12th Annual Underground Coal Gasification Symposium**,** Washington, DC, 1986.

Howard, J.B. Fundamentals of Coal Pyrolysis and Hydropyrolysis. In *Chemistry of Coal Utilization: 2nd Suppl. Ed*.; Elliott, M.A., Ed.; Wiley: New York, 1981; 665-784.

Incropera, F.; DeWitt, D. *Fundamentals of Heat and Mass Transfer.* 4th Ed.; Wiley: New York**,** 1996.

Javadpour, F.; Fisher, D.; Unsworth, M. Nanoscale Gas Flow in Shale Gas Sediments. *J. Can. Pet. Tech*., **2007**, 46, 55-61.

Javadpour, F. Nanopores and Apparent Permeability of Gas Flow in Mudrocks (Shales and Siltstone). *J. Can. Pet. Tech*., **2009**, 48, 16-21.

Knaus, E.; Killen, J.; Biglarbigi, K.; Crawford, P. An Overview of Oil Shale Resources. In *Oil Shale: A Solution to the Liquid Fuel Dilemma*; American Chemical Society: New York, 2010; 3-20.

Kreinin, E. V. Nontraditional Thermal Technologies for Production of Heavy-Extractable Fuels: Coal, Hydrocarbons.; OAO Gazprom: Moscow, Russia, 2004.

Larsen, J. The Effects of Dissolved CO_2 on Coal Structure and Properties. *Int. J. Coal Geo*. **2004**, 57, 63–70.

Lee, S. Proposed Oil Shale and Tar Sands Resource Management Plan Amedments to Address Land Use Allocations In Colorado, Utah, and Wyoming and Final Programmatic Environmental Impact Statement.; Department of the Interior Bureau of Land Management: Washington, D.C., 2008; A-43.

Lewellen P. Product Decomposition Effects in Coal Pyrolysis. MS thesis, Massachusetts Institute of Technology, Cambridge, MA, 1975.

Mazzotti, M., Pini, R., Storti, G. Enhanced Coalbed Methane Recovery. *J. Supercrit. Fluids*, **2009**, 47, 619-627.

Moore, T. Coalbed Methane: A Review. *Int. J. Coal Geo*., **2012**, 101, 36-81.

Nie, R.-S.; Meng, Y.-F.; Guo, J.-C.; Jia, Y.-L. Modeling Transient Flow Behavior of a Horizontal Well in a Coal Seam. *Int. J. Coal Geo*., **2012**, 92, 54–68.

Oil Shale Research, Development and Demonstration Project: Plan of Operation. Chevron USA: Houston, 2006.

Pan, Z.; Connell, L. Modeling Permeability for Coal Reservoirs: A Review of Analytical Models and Testing Data. *Int. J. Coal Geo*., **2012**, 92, 1-44.

Pant, L.; Mitra, S.; Secanell, M. Absolute permeability and Knudsen diffusivity measurements in PEMFC gas diffusion layers and micro porous layers. *J. Pow. Sources*, **2012**, 206, 153-160.

Pashin, J.C. Coalbed Methane. *Natural Resources Research*, **2011**, 20, 282–286.

Perkins, G.; Sahajwalla, V. A Mathematical Model for the Chemical Reaction of a Semi-infinite Block of Coal in Underground Coal Gasification. *Energy Fuels*, **2005**, 19, 1679–1692.

Perkins, G.; Sahajwalla, V. A Numerical Study of the Effects of Operating Conditions and Coal Properties on Cavity Growth in Underground Coal Gasification. *Energy Fuels*, **2006**, 20, 596–608.

Perkins, G.; Sahajwalla, V. Modeling of Heat and Mass Transport Phenomena and Chemical Reaction in Underground Coal Gasification. *Chem. Eng. Res. Des.,* **2007**, 85 (A3), 329–343.

Porter, I. UCG: The 3rd Way. In *Proceedings of the 7th Underground Coal Gasification Conference;* UCGA: London, UK, 2012; 215-227.

Russel, W.; Saville, P.; Greene, M. Truncated Tar Yields from Rapid Pyrolysis of Wyodak Particles. *AIChE J*., **1979**, 58, 231-243.

Secure Fuels from Domestic Resources: The Continuing Evolution of America's Oil Shale and Tar Sands Industries; U.S. Department of Energy Office of Petroleum Reserves: Washington, D.C., 2008; 28-29.

Seifi, M.; Chen, Z.; Abedi, J. Numerical Simulation of Underground Coal Gasification Using the CRIP Method. *Can. J. Chem. Eng*., **2011**, 89, 1528-1535.

Serio, M.; Peters, W.; Howard, J. Kinetics of Vapor-Phase Secondary Reactions of Prompt Coal Pyrolysis Tars . *Ind. Eng. Chem. Res.*, **1987**, 26, 1831-1838.

Shafirovich, E.; Varma, A. Underground Coal Gasification: A Brief Review of Current Status. *Ind. Eng. Chem. Res.* **2009**, 48, 7865-7875.

Smith, K.L.; Smoot, L.D.; Fletcher, T.H.; Pugmire, R.J. *The Structure and Reaction Processes of Coal*; Plenum Press: Denver, 1994.

Solomon, P.; Serio, M.; Suuberg, E.; Coal Pyrolysis: Experiments, Kinetic Rates and Mechanisms. *Prog. Ener. Comb. Sci*., **1992**, 18, 133-220.

Solomon, P.; Serio, M.; Carangelo, R.; Markham, J. Decomposition of Lignites in Oxygen-Deprived Coal Flames. *Fuel*, **1986**, 65, 182-200.

Sury, M.; White, M.; Kirton, J.; Carr, P.; Woodbridge, R.; Mostade, M.; Chappell, R.; Hartwell, D.; Hunt, D.; Rendell N. *Review of Environmental Issues of Underground Coal Gasification: Best Practice Guide*; Report COAL R273; DTI/Pub URN 04/1881; DTI: London, 2004; 541-558.

Suuberg E.M. Rapid Pyrolysis and Hydropyrolysis of Coal. Sc. D. Thesis, Massachusetts Institute of Technology, Cambridge, MA, 1977.

Suuberg, E.M. *Chemistry of Coal Conversion*; Plenum Press: Denver, 1985.

Tyler, R. Flash Pyrolysis of Coals. Devolatilization of Bituminous Coals in a Small Fluidized-bed Reactor, *Fuel*, **1980**, 59, 218-226.

Wellington, S.; Karanikas, J.; Vinegar, H.; de Rouffignac, E.; Berchenko, I.; Stegemeier, G.; Zhang, E; Fowler, T.; Ryan, R. *In Situ* Thermal Processing of a Coal Formation to Control Product Composition. U.S. Patent 6588503, July 8, 2003.

Westmoreland, P.; Dickerson, L. Pyrolysis of Blocks of Lignite. *In Situ*, **1980**, 4, 325-343.

White, F.M. *Viscous Fluid Flow*, 2nd Ed.; McGraw-Hill: Boston, 1991.

Yip, K.; Wu, H.; Zhang, D. Mathematical Modelling of Collie Coal Pyrolysis Considering the Effect of Steam Produced *In Situ* from Coal Inherent Moisture and Pyrolytic Water. *Proc. Comb. Inst*., **2009**, 32, 2675-2683.

Yu, J.; Lucas, J.A.; Wall, T.F. Formation of the Structure of Chars During the Devolatilization of Pulverized Coal and its Thermoproperties. *Prog.Ener.Comb.Sci.* **2007**, 33, 135-170.

UCG Demonstration Facility, Queensland. http://www.lincenergy.com/clean_energy_australia.php (accessed April 23, 2010).